First-principles study of π conjugate molecules adsorbed on noble metal surfaces toward the design of electrodes for organic devices

Kenji TOYODA

March 2010

First-principles study of π conjugate molecules adsorbed on noble metal surfaces toward the design of electrodes for organic devices

A dissertation submitted to

THE GRADUATE SCHOOL OF ENGINEERING SCIENCE

OSAKA UNIVERSITY

in partial fullfillment of the requirement for the degree of

DOCTOR OF PHILOSOPHY IN SCIENCE

BY

Kenji TOYODA

March 2010

Abstract

Recently, organic electronic such as organic electroluminescence, organic field effect transistors, and organic solar cell, has been attracting, because of their promising properties, for example, low-cost processing, large area devices, low-weight with flexibility, and functionalization with molecular modification. The vacuum level shift is induced by interface dipole and largely affects the carrier injection, which can determine the performance of the organic devices. We have studied the electronic structures of π conjugate molecules (benzene, pentacene, and perfluoropentacene(PFP)) adsorbed on noble metal surfaces (Cu, Ag, and Au) by using first-principles calculations, to clarify the origins of the interface dipoles.

We found that the semiempirical van der Waals (DFT-D) method to include van der Waals interactions can reproduce the accurate molecule-metal distance for organic/metal interfaces. On Ag and Au, the distances for the adsorbed system are almost the same, reflecting that the Ag and Au surfaces are chemically inert. On the other hand, on Cu, the adsorption distances are different for different adsorbate. The PFP-Cu distance is larger than the pentacene-Cu distance, although PFP is more chemically reactive than pentacene. This is presumably because of the repulsion between $2p$ electrons of F atoms and electrons of substrate. Thus, these results indicate that functional group can control adsorption distance. The work function change is sensitive to the molecule-substrate distance, and thus the molecule-substrate distance is a key parameter for the interfacial electronic state. The calculated work function changes at the calculated molecule-substrate distances are in good agreement with the experimental values, which shows that the method can predict the vacuum level shift of organic/metal interfaces accurately. The analysis of slope parameter shows the electronic and the geometric contribution to the interface dipole. Moreover, for the PFP-adsorbed system, the intramolecular dipole also contributes to the interface dipole. The calculated electronic structures show that for Au, a physical fac-

tor dominates the molecule-substrate interaction whereas for Cu and Ag, a chemical factor contributes to the interaction if the molecule is rather chemical reactive such as pentacene and PFP.

We have examined the induced density interface states (IDIS) model by using first-principles calculation. The IDIS model can describe well if the molecule-metal interaction is weak. On the other hand, it cannot describe if the interaction is strong, because of the back-donation from the surbstrate to the adsorbate. Thus, we partition the interface dipole into physical component and chemical component, and we examine the dependence of each component on the electron affinity of the adsorbate. We consider that on each surface the adsorption distances are almost constant with any adsorbate, because of the balance between the chemical reactivity and the repulsion of electrons of the adsorbate with those of the substrate. Consequently, the physical component of the interface dipole is independent on adsorbate. We show that the chemical component is extracted and depends on the electron affinity of the adsorbate, and we estimate the back donation. These results indicate that we can predict the vacuum level shift from the chemical trend.

Acknowledgments

I would like to express my sincere gratitude to Prof. Yoshitada Morikawa for valuable discussions and a number of encouragements in the course of this study. I also wish to express my gratitude to Prof. Hitoshi Katayama-Yoshida for his special advices.

I express my special thanks to Prof. Koun Shirai and Prof. Akira Yanase for their many important advices and directions of this work. I am grateful to Assistant Prof. Ikutaro Hamada, Dr. Susumu Yanagisawa, and Dr. Kyuho Lee for their considerate support and helpful discussions and comments.

I would also like to thank Dr. Daisuke Ueda, Dr. Kenji Iijima, Dr. Kiyoyuki Morita, and Mr. Ayumu Tsujimura for their continuous encouragements.

Thanks are extended to all-members of the Department of Condense Matter Physics and Panasonic Corporation for their various help.

Finally, I wish to thank my wife and my family for encouragements and supports.

Contents

Chapter 1

Introduction

1.1 Background

1.1.1 Organic semiconductor

In the early of 1950s, H. Akamatu and H. Inokuchi found that violanthrone and its derivatives have electrical conductivity, by purifying the materials after repeated sublimations. This is because the molecular structures are made of the network planes of carbon atoms, and thus the molecules are used as a model of carbon black. The electrical resistivity was measured and the values are $\sim 1 \times 10^{10}$ ohm-cm. Therefore, they called the conducting organic material as organic semiconductor [1].

In the middle of 1950s, H. Akamatu, H. Inokuchi, and Y. Matsunaga found that polycyclic aromatic hydrocarbon such as perylene forms molecular complex with bromine or iodine. The complexes behave as typical semiconductors with energy gaps for conductivity of 0.1-0.2 eV, as well as with low electrical resistivity ranging from 1 to 10^3 ohm-cm. The complexes are unstable and a substitution reaction of halogen takes place, and thus the resistivity changes. The origin of the high conductivity is due to the interaction between hydrocarbon molecules and halogen molecules, and this is presumably due to the overlapping of molecular orbitals stretching throughout the crystal [2, 3].

The first conducting polymer was synthesized in the 1970s. In the early 1970s, H. Shirakawa collaborating with A. G. MacDiarmid and A. J. Heeger of the University of Pennsylvania could increase the conductivity of polyacetylene films a billion times by doping iodine. The doped films looked like golden

metallic sheets. Later more than a dozen organic polymers could be made conducting by appropriate doping. Now plastics with conductivity comparable to that of copper can be easily fabricated. In 2000, A. J. Heeger, A. G. MacDiarmid, and H. Shirakawa won the Noble Prize in Chemistry for the discovery and development of conductive polymer. Early work on conducting plastics is described in Refs. [4, 5, 6, 7, 8].

The semiconducting conjugated polymers can be used as the active layer in light emitting diodes (LEDs), field effect transistors (FETs), solar cells, and so on. These devices are being pushed toward commercialization, because they can be fabricated by inexpensive techniques, such as spin coating, ink-jet printing, low temperature fiber drawing, and screen-printing on the flexible substrates [9]. This leads to a real advantage over the expensive and sophisticated technology using inorganic materials in the semiconductor industry. The flexible plastic films make these devices interesting, because of the advantage in terms of flexibility, low power, low weight, and low-cost processing. In view of the above advantages, conducting plastics have emerged as a new class of electronic materials. It might be possible that by the year 2015, the silicon technology might hit the physical limit and the conducting polymers may become the major players in the filed of semiconductor devices.

1.1.2 Organic devices

Since the discovery of electroluminescence from organic materials, it has been recognized that the conducting polymers are important for fabricating the organic LEDs (OLEDs) [10]. To improve the performance of OLEDs a good understanding of basic device physics is very necessary. At present, OLED technology has become a competitor for conventional light sources and display technologies like liquid crystal displays (LCDs). Displays based on organic semiconductors have already entered the market. Flat panel displays and LEDs are important applications being pursued now. A respectable electroluminescence (EL) from an organic molecule solid device was first demonstrated by Kodak in 1987 [11]. The first polymer LED was fabricated by Cambridge University in 1990 [12]. This stimulated a lot of excitement and intense activity in the field of organic electronic and optoelectronic devices.

In 1987, C. W. Tang and collaborators fabricated the first organic LED using tris(8-hydroxyquinoline) aluminum (Alq_3) emitting green light. The LED efficiency, in lumen's per watt, can be more than that

of the household bulb and their life time can be more than 10,000 hours. However, in the conventional structures, the light is wasted because of its leakage in all directions. In 1994, A. Dodabalapur and his co-workers at Bell laboratories constructed EL devices by sandwiching Alq_3 between reflecting surfaces forming a mirocavity. This structure conforms to the physics of Fabry-Perot cavity. By varying a thickness of the inert layer, undesirable light can be filtered out and emission of light can be obtained at any desired wave length. Because a microcavity makes LEDs more efficient and current less, LEDs can last longer. The group of the Cavendish laboratory headed by R. H. Friend [13] used Poly(phenylene vinylene) (PPV) and its derivatives for fabricating the LEDs. They observed the green-yellow emission from the PPV LED in 1990. These LEDs gave 2.5 lumen's per watt. To be driven at high voltage makes light output increasing but LEDs faster brokendown, because of the heat generated.

At present, the GaAs wafer size is limited to about 6 inch diameter. To make large displays, GaAs based LEDs must be individually mounted and wired. A reasonable letter size can take up to 35 LEDs. However, the size of organic film is in principle unlimited. Moreover, the starting material for organic displays can be much cheaper. Intense effort has been made in developing the thin film OLEDs [14]. Philips at Eindhoven has had a research program on polymers for several years. They have an agreement with Cambridge Display Technology (CDT) which gives Philips access to CDT's patented technology. CDT is a spin-off company of the research group at the Cambridge Cavendish Laboratory set up in 1992 by R. Friend and A. Holmes of Cambridge University. The group has also fabricated the PPV LEDs with microcavities. CDT believes that over a period of time, cathode ray tube (CRT) could be replaced by the polymer devices. The display business is estimated to be more than $ 42 billion shortly. Polymer scientists are trying hard to carve a share for themselves from this business.

In late 1980s, first organic field effect transistors (OFETs) were fabricated [15]. Very significant improvements have been made in the performance of OFETs. OFETs are of great interest for both academic and industrial institutions. Several authors have fabricated OFETs with performance comparable to the best amorphous silicon (a-Si) transistors. The mobility of the carriers has been improved considerably. For example, in pentacene transistors mobility of more than 1 cm^2/Vs has been obtained. The transistors have application as drivers for electronic barcodes, radio frequency identification (RFID) tags, large area sensor array, and in other low-cost electronic devices.

OFETs can be fabricated with a low-temperature process [16, 17]. It is therefore possible to fabricate thin film transit or (TFT) arrays for flat panel displays using a low-cost process. The substrate are low-cost and flexible such as polyetylene terepthalate (PET). The low-cost, large area TFT arrays can be used for many applications, e.g. electronic paper, smart cards, remotely updateable posters, notice boards, and so on. Currently the amorphous silicon (a-Si) technology is used for such applications, although the technology is expensive. These applications will only become popular in marketplace if the cost of production is substantially reduced. Thus, this is the driving force for the R&D effort in OFETs. As emphasized by Angelis *et al.* [18], it is very important to understand the transport mechanisms in the OFETs structure. In fact, many problems including aging effects can be solved if transport mechanism is well understood.

Solar cells (also known as photovoltaic (PV) devices) [19, 20] have become an important source of renewable energy. The world annual production of electricity by silicon solar cells is now several tens of megawatts. However, the cost of these Si cells is high and they are not able to complete with the conventional power plants. The search for cheaper PV cells has been on for a long time [8]. Early work on conducting polymer solar cells was done with the hope that the cost of the cells will come down. On the other hand, the conversion efficiency, η, of the early cells was only a few hundredths of a percent. The main difficulty arises because of the fact that the excitons generated by the incident light in the conducting polymers have a large binding energy. The excitons do not dissociate at room temperature, and thus the probability of their recombining is much higher than that of their dissociation. This property is instead useful for LEDs and explains why the work on LEDs has been so successful [21, 22, 23]. In 1992, two important papers were published [24, 25]. These paper showed that Buckminsterfullerene C_{60}, mixed with a conducting polymer, is very effective in dissociating the excitons in the polymer. More recently PV devices have been fabricated using other exciton breaking agents [26, 27, 28, 29, 30, 31, 32, 33]. Dye sensitized high efficiency solar cells have also fabricated. The conducting organic semiconductors are now challenging the dominance of the photovoltaic field by Si and other inorganic semiconductors [34].

1.2 Organic/metal interfaces

As described in the preceding section, organic devices such as OLEDs, OFETs, and organic PV are attracting enormous attraction because of their promising properties for example low-cost processing and flexibility. The energy level alignment at the organic/metal interfaces in organic devices governs the efficiency of the carrier injection, which ultimately determines the performance of the organic devices [35, 36]. The barrier heights of electron ($\Phi_{\mathrm{B}}^{\mathrm{n}}$) and hole ($\Phi_{\mathrm{B}}^{\mathrm{p}}$) injection can related to the substrate metal work function (ϕ_{m}) by

$$\Phi_{\mathrm{B}}^{\mathrm{n}} = \phi_{\mathrm{m}} - A + \Delta, \tag{1.1}$$

$$\Phi_{\mathrm{B}}^{\mathrm{p}} = -\phi_{\mathrm{m}} - I - \Delta, \tag{1.2}$$

where ϕ_{m} is the metal work function, A and I are the electron affinity and the ionization energy of the organic molecule, respectively, and Δ is the vacuum level shift (Fig. 1.1) [35, 36].

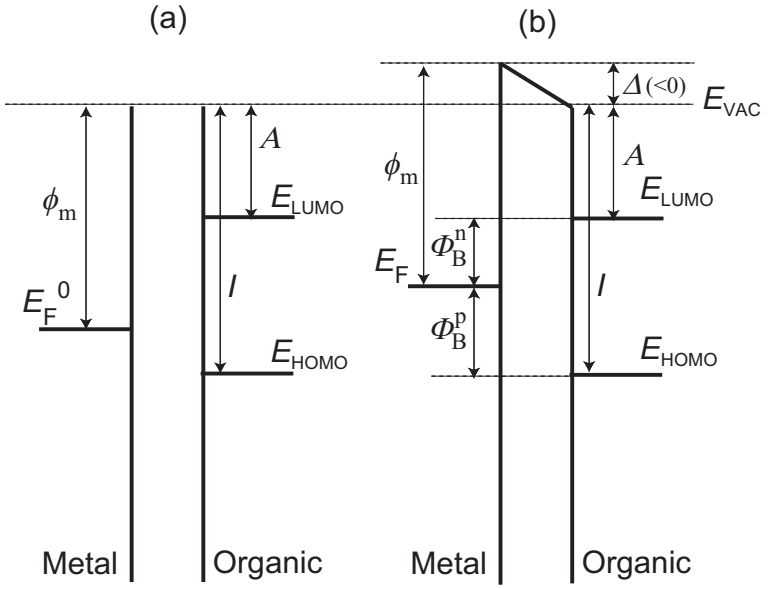

Figure 1.1: Energy band diagram at organic/metal interfaces (a) before contact and (b) after contact

The Δ is induced by a dipole layer formed at an organic/metal interface, which can change the barrier height of the carrier injection by as large as 1 eV [35, 36]. The following factors of the interface dipole formation have been proposed (Fig. 1.2) [35, 36].

- charge transfer (a1, a2)
- mirror effect (b)
- push back effect (c)
- chemical interaction (d)
- interface state (e)
- permanent dipole of adsorbates (f)

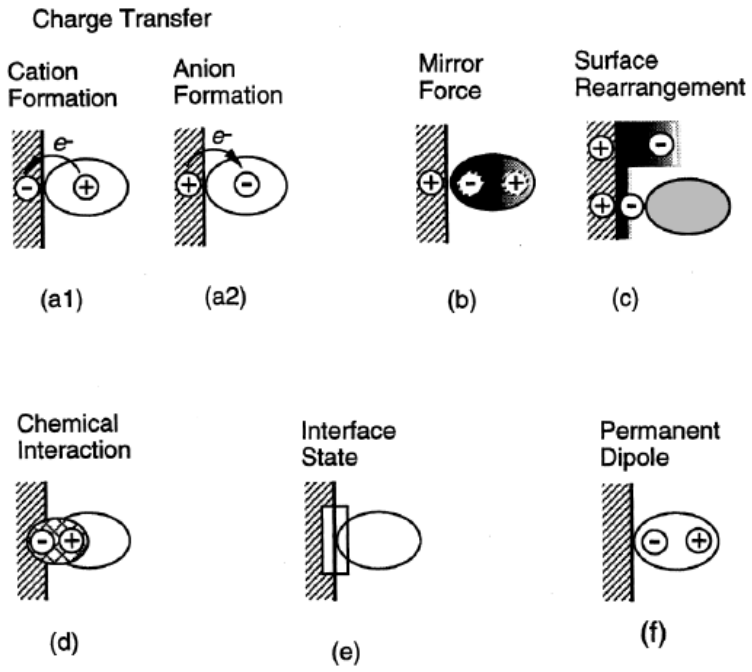

Figure 1.2: Possible factors forming and affecting the interface dipole [36]

A slope parameter S is defined by the derivative of the barrier height with respect to the substrate work function (ϕ_{m}), i.e.,

$$S = \frac{\mathrm{d}\Phi_{\mathrm{B}}^{\mathrm{n}}}{\mathrm{d}\phi_{\mathrm{m}}} = -\frac{\mathrm{d}\Phi_{\mathrm{B}}^{\mathrm{p}}}{\mathrm{d}\phi_{\mathrm{m}}}, \tag{1.3}$$

and it gives the variations of the barrier as a function of ϕ_{m} [35, 36, 37]. Substituting Eqs. (1.1) and (1.2) into Eq. (1.3) leads to

$$S = 1 + \frac{\mathrm{d}\Delta}{\mathrm{d}\phi_{\mathrm{m}}} \equiv 1 + k. \tag{1.4}$$

If the barrier heights are independent of ϕ_{m}, S is zero (Bardeen limit). On the other hand, if Δ is independent of ϕ_{m}, S is unity (Schottky limit) [37]. It should be noted that the usual definition of Schottky limit is that Δ is zero. Before Seki and co-workers reported the existence of the vacuum level shift (Δ), it had naively assumed that the vacuum levels of the metal substrate and the organic semiconductors coincide (vacuum level alignment). This is partly because the interaction at organic/metal interfaces was considered to be so weak that S was nearly unity (Schottky limit) [35, 36]. However, S's at several organic/metal interfaces are observed to take a variety of values from 0 to 1 [35, 36]. Even for *n*-alkane/metal interfaces, which are typical physisorption system, S is $\sim$0.6.

Morikawa and co-workers pointed out the important contribution of the geometric factor, especially the molecule-metal distance to S, i.e. the substrate dependence of Δ [38]. From first-principles calculations, they showed that the dependence of Δ on substrate metals is quite weak, provided that the molecule-metal distance is the same for different metal substrates. That is to say, the interface is in the Schottky limit, which is in accordance with the above mentioned naive consideration, and the substrate dependence of Δ comes solely from the difference in the molecule-metal distance. They predicted that the difference in the molecule-metal distance is as large as 0.03 nm between *n*-alkane/Cu(110) and *n*-alkane/Au(111) interfaces. The importance of the molecule-metal distance for S is also pointed out for PTCDA/metal interfaces [39]. Recently, molecule-metal distances have been measured experimentally by using x-ray standing wave (XSW) technique, and significant difference in the molecule-metal distance for different substrate has been reported [40, 41].

On the contrary, for weakly chemisorbed metal/organic interfaces, the induced density of interface states (IDIS) model has been proposed to predict Δ and S theoretically [42, 43, 44, 45, 46, 47, 48, 49]. At metal/organic interfaces, molecular states such as the highest occupied molecular orbital (HOMO) and the lowest unoccupied molecular orbital (LUMO) are broadened because of interaction with substrate metallic states and induces finite density of states (DOS) between the HOMO-LUMO gap. From a simple model, the magnitude of the induced density of interface states, which is rather insensitive to the molecule-metal distance, can determine Δ and S. The model is applied to various metal/organic interfaces and has been shown to predict Δ and S surprisingly well.

Although the energy level alignment at organic/metal interfaces has been intensively studied, a

coherent picture has never been emerged yet, and it is therefore essential to clarify the factors that determine the formation of the interface dipole layer systematically, in order to control the energy difference between the metal Fermi level and the molecular levels.

1.3 Purpose

The main purpose of this paper is to clarify the formation mechanism of interface dipole at organic/metal interfaces. In this thesis, the following issues are studied.

1. Formation factors of interface dipole

2. Prediction model for interface dipole

In Chapter 2, we investigate the electronic structures of the adsorbed systems by using first-principle calculations, and discuss the substrate dependence of the electronic structure. In Chapter 3, we examine the IDIS model using first-principles calculations, and discuss prediction model for interface dipole. The thesis ends with some conclusions and an outlook for the future.

Chapter 2

Theoretical method

In this study, we have investigated π conjugate molecules adsorbed on noble metal surfaces using density functional theoretical theory (DFT) within a generalized gradient approximation (GGA). We employ benzene(C_6H_6), pentacene($C_{22}H_{14}$), and perfluoropentancen($C_{22}F_{14}$, PFP) as π conjugate molecules, because benzene is a typical aromatic hydrocarbon, and pentacene and PFP are organic compounds for p-type [50] and n-type OFETs [51], respectively. Furthermore, we employ Cu(111), Ag(111), and Au(111) as metal surfaces, because noble metals are typical electrode materials. As is well known, GGA cannot describe long-range van der Waals (vdW) forces, which dominate the interaction between organic molecules and metal surfaces. Thus, we employ the semi-empirical vdW (DFT-D) method [52, 53, 54, 55, 56, 57] and the vdW density functional (vdW-DF) method [58, 59] to describe the vdW interactions, and calculate the adsorption energies by using the two methods.

2.1 DFT calculations

Our calculations were carried out using STATE (Simulation Tool for Atom TEchnology), a first-principles molecular dynamics program, which has been successfully applied to metal surfaces and organic/metal interfaces [38, 60, 61, 62, 63, 64]. We used the Perdew-Burke-Ernzerhof (PBE) generalized gradient approximation (GGA) [65] for the exchange-correlation functional. The electron-ion interaction was described by *ab initio* pseudopotentials [66, 67], and wave functions and augmented charge density were expanded using a plane-wave basis set with the cutoff energies of 25 and 225 Ry, respectively. The calculated equilibrium lattice constants of Cu, Ag, and Au are 0.365, 0.408, and 0.415 nm, respectively, and they are in reasonable agreement with the experimental values of 0.361, 0.409, and 0.408 nm, respectively. We used a repeated slab model to represent the metal surfaces, in which one slab consists of four or six atomic layers. A vacuum region of $\sim$2 nm was inserted between the slabs. A π conjugate molecule is adsorbed on only one surface of a slab with its molecular plane parallel to the surface in a surface unit cell.

In a geometry optimization, we fixed the height of carbon atoms from the first-layer of the clean (111) surfaces (hereinafter denoted by Z_{C}), to calculate adsorption energies and vacuum level shifts as a function of Z_{C}. We also fixed the bottom layer of the substrate slabs at their respective bulk positions. The remaining degree of freedom, including carbon positions parallel to the surface, were fully optimized, until the maximum force dropped below below a threshold value of 0.08 nN.

The work function difference between the two surfaces of a slab was compensated for using a dipole correction [68]. Work function were calculated from the difference between the Fermi energy of the system and the average electrostatic potential energy at the center of the vacuum region. It has been reported experimentally that the vacuume level is slightly shifted by the further deposition up to thickness of a few nm, and then becomes almost constant [35, 36]. Thus, the vacuum level shifts can be calculated from the work function changes induced by the adsorption of the π conjugate molecule.

2.2 van der Waals correction to the density functional energy calculations

We employed the semiempirical van der Waals (DFT-D) method and the van der Waals density functional (vdW-DF) method to include the vdW interactions.

The DFT-D method is proposed by Grimme [52], and is based on a damped atom-pairwise dispersion corrections of the form $C_6 R^{-6}$, where C_6 represents the dispersion coefficient for a given atom pair, and R is the distance between the atoms. The DFT-D total energy is give by

$$E^{\mathrm{DFT-D}} = E^{\mathrm{KS-DFT}} + E^{\mathrm{disp}}, \tag{2.1}$$

where $E^{\mathrm{KS-DFT}}$ is the Kohn-Sham total energy as obtained from the chosen density functional, and E^{disp} is a semiempirical dispersion correction. The method was successfully applied to adenine on graphite(0001) [53], and pyridine on metal surfaces [55]. We derived the C_6 coefficient and the van der Waals radius R_0 for Au, on the basis of Grimm's scheme [52], because they are unavailable in the literature. We used the scalar relativistic Douglas-Kroll approximation [69, 70, 71] and highly accurate relativistic basis sets [72] with the Gaussian 03 program [73]. The C_6 and R_0 for Au are evaluated to be 47.81 J nm^6/mol and 1.497 Å. Following a prescription given by Ref. [52], the scale factor s_6 was set to be 0.75, because GGA-PBE was employed as the exchange-correlation functional.

The vdW-DF method is proposed by Dion *et al.* [58], and is able to calculate vdW interactions from first-principles. This method is successfully applied to several systems. The vdW-DF energy is calculated as

$$E_{xc}^{\mathrm{vdW-DF}} = E_x^{\mathrm{GGA}}[n] + E_c^{\mathrm{LDA}}[n] + E_c^{\mathrm{nl}}[n], \tag{2.2}$$

where n is the electron density self-consistently calculated by the GGA-PBE, $E_x^{\mathrm{GGA}}[n]$ is the exchange energy calculated by the GGA, $E_c^{\mathrm{LDA}}[n]$ is the local density approximation (LDA) correlation, and $E_c^{\mathrm{nl}}[n]$ is the long-range nonlocal correlation energy. For the exchange part, the RPBE[74] is employed according to Ref. [75]. The long-range nonlocal correlation energy is derived from the adiabatic connection fluctuation dissipation theorem, the random phase approximation (RPA), and using a plasmon pole

model for the polarizablity. We employed 0.95 nm for the nonlocal interaction cutoff, and for vdW-DF calculations, we thus used six atomic layer slabs that are thicker than the cutoff.

Chapter 3

Vacuum level shifts and electronic structures

We calculate adsorption energies and vacuum level shifts as a function of Z_{C}.

The adsorption energy E_{ad} is defined by

$$E_{\mathrm{ad}} = E(\text{adsorbate/metal}) - E(\text{adsorbate}) - E(\text{metal}), \tag{3.1}$$

where E(adsorbate/metal), E(adsorbate), E(metal) are the total energies of the adsorbed system, the isolated molecule, and the clean metal surface, respectively. A negative value of E_{ad} means that the adsorbed system is energetically favorable relative to the isolated state.

The vacuum level shift is calculated from the work function change. The work function change $\Delta\phi$ is defined by

$$\Delta\phi' = \phi(\text{adsorbate/metal}) - \phi(\text{metal}), \tag{3.2}$$

where ϕ(adsorbate/metal) and ϕ(metal) are the work function change of the adsorbed system and the clean metal surface, respectively. To estimate the work function change at the experimental surface molecular density of the adsorbate on the surface, we used surface molecular density, n_{metal}, and corrected

$\Delta\phi'$ by using the Helmholtz equation [76]:

$$\Delta\phi = \Delta\phi' \frac{n_{\text{metal}}}{n_0}, \tag{3.3}$$

where $\Delta\phi$ is the corrected work function change, and $n_0 \equiv A_0^{-1}$, where A_0 is the area of the surface unit cell of the adsorbed systems.

3.1 Benzene/Noble Metal

Benzene/metal interfaces are prototypical systems of interfaces between functional aromatic compounds and metal electrodes. Accordingly, benzene on metal surfaces has been extensively studied both experimentally and theoretically [77, 78, 79, 80, 81, 82, 83, 84, 85, 86, 87, 88, 89, 90, 91, 92]. Bilić *et al.* studied benzene on noble metal surfaces using DFT, and showed that their calculations reproduce major qualitative features of the experimental results. However, the magnitude of the binding energy is severely underestimated because of lack of the long-range vdW interactions [86]. Bagus and co-workers made a theoretical study of benzene on noble metal surfaces to compare the calculation results with the experimental ones, and showed that the exchange effect is an important origin of the interface dipole layer and the chemical interaction on Cu(111) is stronger than that on Au(111) [77, 78, 79]. They employed the second-order Møller Plesset perturbation (MP2) method to reproduce the long-range vdW interactions, although their calculations were limited to small clusters. Moreover, the MP2 method tends to overestimate the vdW interactions, creating a need for more accurate methods such as coupled cluster calculations [93, 94].

3.1.1 Calculation model

Figure 3.1 shows the calculation model for benzene adsorbed on noble metal surfaces.

The surface unit cell is (3×3), and a (4×4) **k**-point mesh was used to sample the surface Brillouin zone. The number of the slab is six. It has shown experimentally that benzene is adsorbed at a threefold-hollow site on Ag(111) [83] with C-H bonds parallel to the Ag-Ag nearest neighbor direction (hereinafter denoted by $C_{3v}(\sigma_v)$ and shown in Fig. 3.1) and also with C-H bonds perpendicular to the Ag-Ag nearest neighbor direction (hereinafter denoted by $C_{3v}(\sigma_d)$) [84]. We assumed that the center of the benzene molecules is located at the fcc-hollow site of the (111) surface with the local symmetry $C_{3v}(\sigma_v)$ as shown in Fig. 3.1. Note that in the vdW-DF calculations, the binding energy of benzene adsorbed on Cu(111) with the local symmetry $C_{3v}(\sigma_v)$ is lower than that with the local symmetry $C_{3v}(\sigma_d)$ by $\sim$0.005 eV.

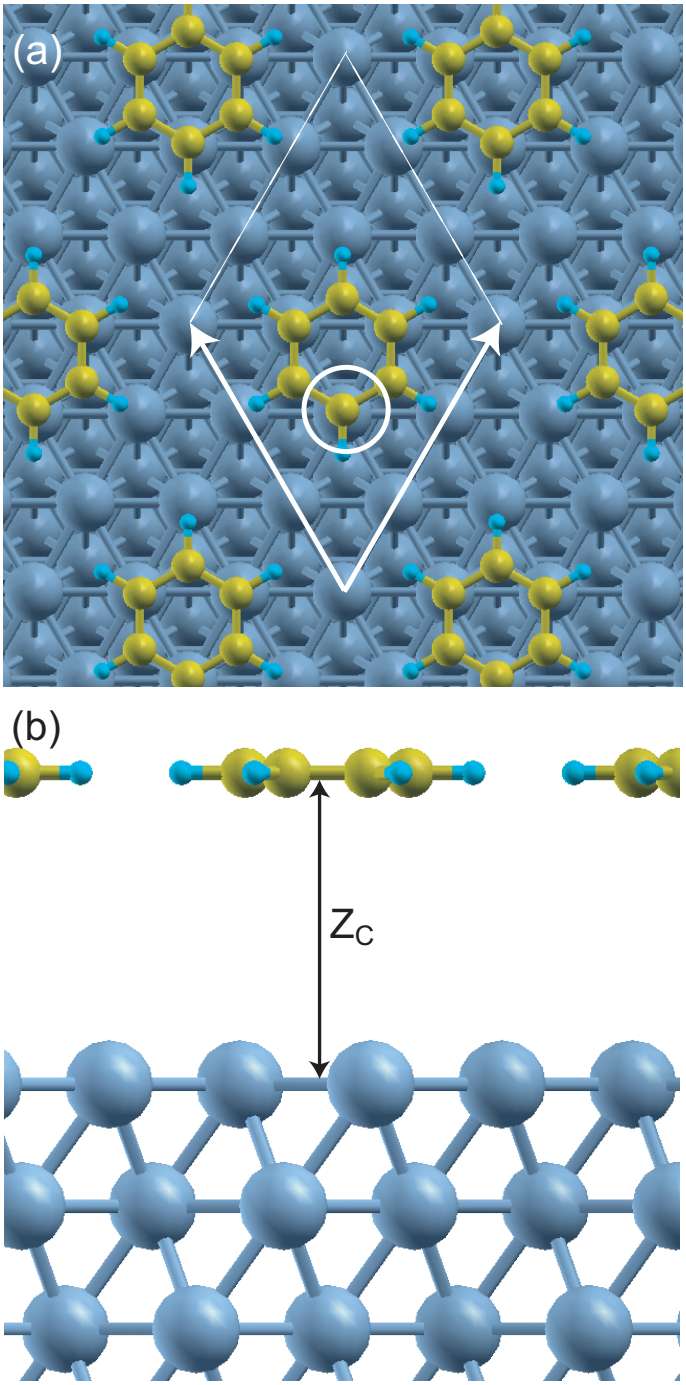

Figure 3.1: (a) Plane view and (b) cross-sectional view of benzene on a (111) surface at a fcc-hollow site. The geometry has the local symmetry $C_{3v}(\sigma_v)$.

3.1.2 Adsorption energy

Figure 3.2 (a)-(c) shows E_{ad} of benzene on Cu(111), Ag(111), and Au(111) as a function of Z_{C} using GGA, DFT-D, and vdW-DF. As shown in Fig. 3.2 (a)-(c), the potential energy curves calculated by GGA have shallow minima, whereas those by DFT-D and vdW-DF have deeper minima. The equilibrium distances calculated by DFT-D are smaller than those calculated by GGA and vdW-DF. Table 3.1 summarizes the equilibrium distances ($Z_{\mathrm{C}}^{\mathrm{GGA}}$, $Z_{\mathrm{C}}^{\mathrm{DFT-D}}$, and $Z_{\mathrm{C}}^{\mathrm{vdW}}$) and the adsorption energies ($E_{\mathrm{ad}}^{\mathrm{GGA}}$, $E_{\mathrm{ad}}^{\mathrm{DFT-D}}$, and $E_{\mathrm{ad}}^{\mathrm{vdW}}$) calculated by GGA, DFT-D, and vdW-DF, respectively.

Table 3.1: The equilibrium distances ($Z_{\mathrm{C}}^{\mathrm{GGA}}$, $Z_{\mathrm{C}}^{\mathrm{DFT-D}}$, and $Z_{\mathrm{C}}^{\mathrm{vdW}}$), and the adsorption energies ($E_{\mathrm{ad}}^{\mathrm{GGA}}$, $E_{\mathrm{ad}}^{\mathrm{DFT-D}}$, and $E_{\mathrm{ad}}^{\mathrm{vdW}}$) calculated by GGA, DFT-D and vdW-DF, respectively, along with the equilibrium distances and the adsorption energies calculated by MP2, and the experimentally determined adsorption energies for benzene on Cu(111), Ag(111), and Au(111).

	Surface	Cu(111)	Ag(111)	Au(111)
GGA	$Z_{\mathrm{C}}^{\mathrm{GGA}}$ / nm	0.37	0.37	0.37
	$E_{\mathrm{ad}}^{\mathrm{GGA}}$ / eV	-0.050	-0.061	-0.068
DFT-D	$Z_{\mathrm{C}}^{\mathrm{DFT-D}}$ / nm	0.29	0.29	0.31
	$E_{\mathrm{ad}}^{\mathrm{DFT-D}}$ / eV	-0.56	-0.64	-0.79
vdW-DF	$Z_{\mathrm{C}}^{\mathrm{vdW}}$ / nm	0.37	0.37	0.37
	$E_{\mathrm{ad}}^{\mathrm{vdW}}$ / eV	-0.55	-0.49	-0.55
MP2	Z_{C} / nm	0.36[a]	0.37[b]	0.38[c]
	E_{ad} / eV	-0.35[a]	-0.33[b]	-0.31[b]
Expt.	$E_{\mathrm{ad}}^{\mathrm{exp}}$ / eV	-0.58[d]	-0.42[e]	-0.60[f]

[a] Ref. [78].
[b] Ref. [77].
[c] Ref. [77, 79].
[d] Ref. [78, 80].
[e] Ref. [77, 81].
[f] Ref. [77, 82].

The $E_{\mathrm{ad}}^{\mathrm{vdW}}$ values are -0.55, -0.49, and -0.55 eV for Cu, Ag, and Au, respectively. They are in good agreement with the experimental values of -0.58 [78, 80], -0.42 [77, 81], and -0.60 eV [77, 82], respectively, and the agreement is slightly better than that of the MP2 method [77, 78]. The $E_{\mathrm{ad}}^{\mathrm{DFT-D}}$ values are

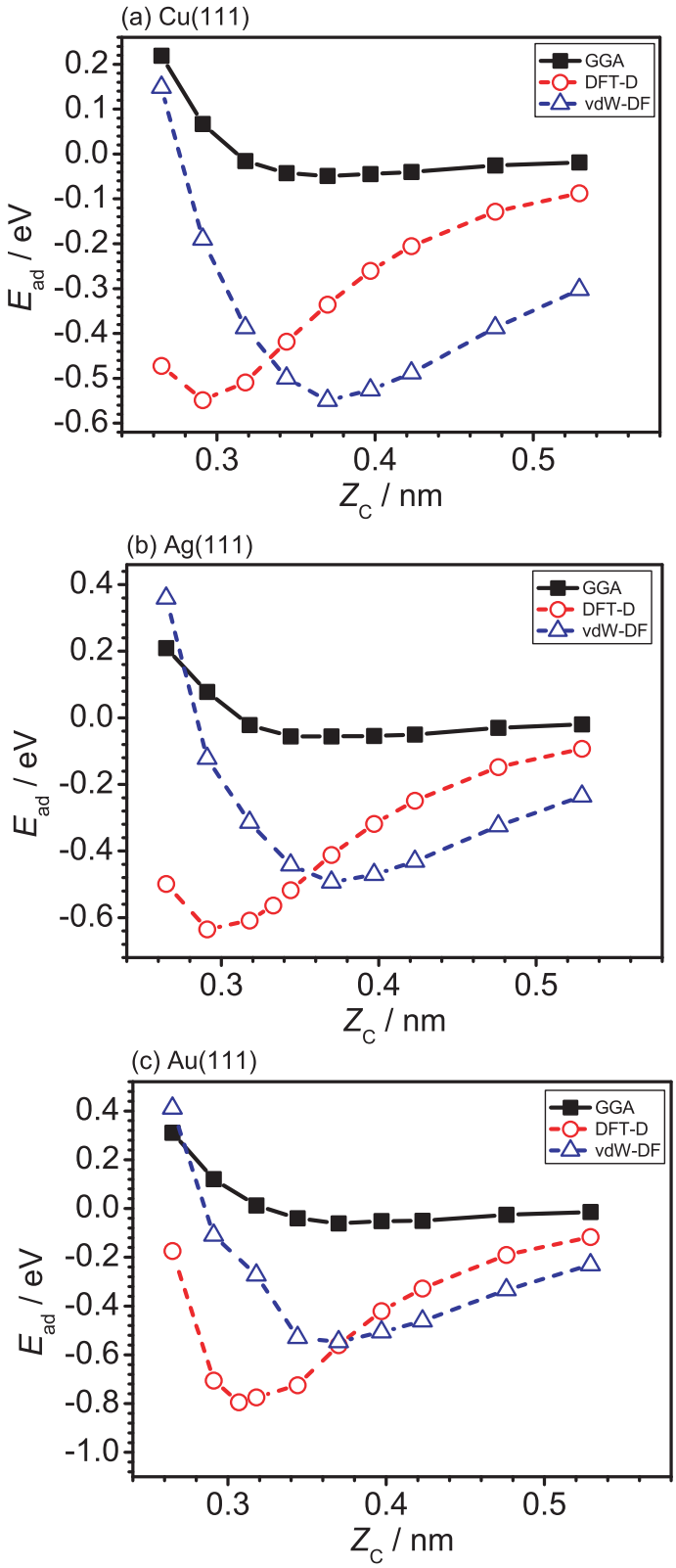

Figure 3.2: The adsorption energy (E_{ad}) as a function of the distance between the molecule and the metal surface (Z_{C}) using GGA, DFT-D, and vdW-DF for benzene on (a) Cu(111), (b) Ag(111), and (c) Au(111)

-0.56, -0.64, and -0.79, respectively. For Cu, the value is in good agreement with the experimental value, whereas for Ag and Au, the absolute values are slightly overestimated by ∼0.2 eV. This might be because the C_6 coefficient for heavier atoms may be overestimated by the Grimm's scheme [57]. The $E_{\rm ad}^{\rm GGA}$ values are -0.050, -0.061, and -0.068 eV for Cu, Ag, and Au, respectively, which are an order of magnitude smaller than the experimental values and are close to previous GGA results [86]. This indicates that the interaction between benzene and close-packed noble metal surfaces is predominantly due to the dispersion interaction.

The $Z_{\rm C}^{\rm GGA}$ and $Z_{\rm C}^{\rm vdW}$ values are the same, although the $E_{\rm ad}$ values are significantly dependent on the choice of the energy functionals. Moreover, the $Z_{\rm C}$ values calculated by MP2 are also almost the same. On the other hand, the $Z_{\rm C}^{\rm DFT-D}$ values are 0.29, 0.29, and 0.31 nm for Cu, Ag, and Au, respectively. They are smaller than those calculated by the other methods. Romaner *et al.* reported that for PTCDA on noble metal surfaces, $Z_{\rm C}^{\rm vdW}$'s are systematically overestimated [39]. Unfortunately, the benzene-substrate distances have never been measured experimentally, and thus we cannot compare our calculated results with experimental ones. However, as will be discussed later, by comparing the calculated vacuum level shifts with the experimental ones, we observe similar trend. Thus, we conclude that the DFT-D method can give reasonable benzene-metal distance whereas the GGA and the vdW-DF methods overestimate it.

3.1.3 Vacuum level shift and slope parameter

The vacuum level shift is calculated from the work function change. The work function change, $\Delta\phi$, is estimated according to Eqs. (3.2) and (3.3). For Ag and Au, $n_{\rm Ag(111)}$ and $n_{\rm Au(111)}$ are based on the experimental data of benzene on Ag(111) [84] and Au(111) [92], respectively. Because the surface molecular density on Cu(111) have been never measured experimentally, we assumed that $n_{\rm Cu(111)}$ is the same as $n_{\rm Au(111)}$. In this way, the work function change ($\Delta\phi$) are scaled from the bare calculated values ($\Delta\phi'$) by factors 1.3, 1.0, and 1.6 for Cu, Ag, and Au, respectively.

Figure 3.3 shows $\Delta\phi$ of benzene adsorbed on Cu(111), Ag(111), and Au(111) as a function of $Z_{\rm C}$ using GGA. The experimentally determined work function changes on Cu(111), Ag(111), and Au(111) are indicated by horizontal dashed lines, whereas the equilibrium distances on Cu(111), Ag(111), and

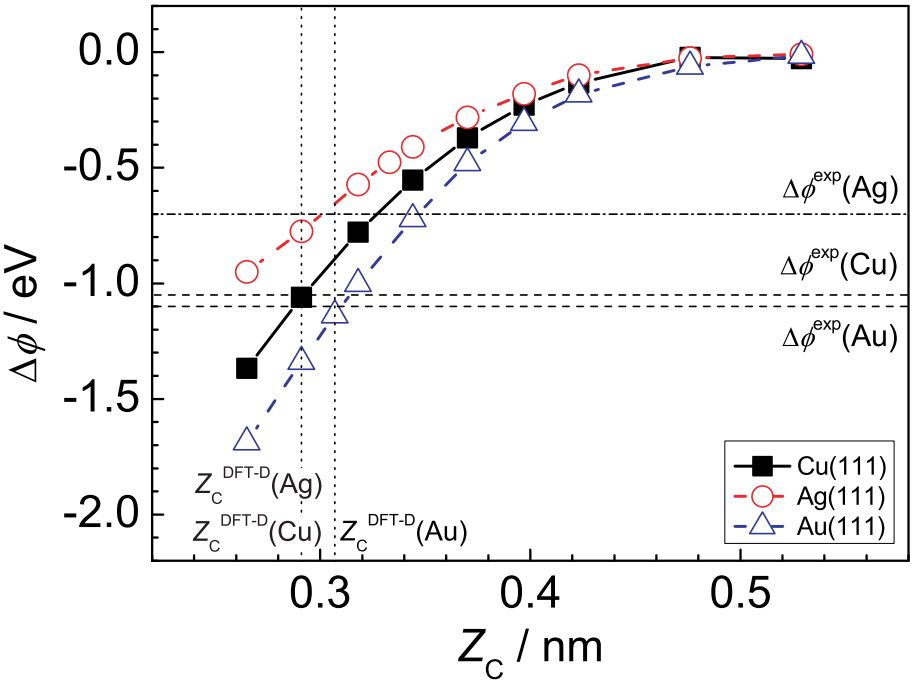

Figure 3.3: The work function change ($\Delta\phi$) as a function of Z_{C} for benzene on Cu(111), Ag(111), and Au(111). The experimental values of $\Delta\phi$ on Cu(111), Ag(111), and Au(111) are shown by horizontal dashed lines. The equilibrium distances on Cu(111), Ag(111), and Au(111) ($Z_{\mathrm{C}}^{\mathrm{DFT-D}}$(Cu), $Z_{\mathrm{C}}^{\mathrm{DFT-D}}$(Ag), and $Z_{\mathrm{C}}^{\mathrm{DFT-D}}$(Au)) calculated by DFT-D are shown by vertical dotted lines.

Au(111) calculated by DFT-D are indicated by shown by vertical dotted lines.

Table 3.2 summarizes $\Delta\phi$'s calculated by GGA at several distances for benzene on Cu(111), Ag(111), and Au(111). For Cu(111), Ag(111), and Au(111), the calculated $\Delta\phi$'s at $Z_{\mathrm{C}}^{\mathrm{DFT-D}}$ are in excellent agreement with the experimental values of -1.05 [79], -0.70 [77], and -1.10 eV [79], respectively. On the other hand, the absolute values of the calculated $\Delta\phi$'s at $Z_{\mathrm{C}}^{\mathrm{GGA}}$ and $Z_{\mathrm{C}}^{\mathrm{vdW}}$ are significantly underestimated, which comes from the overestimation of the $Z_{\mathrm{C}}^{\mathrm{GGA}}$ and $Z_{\mathrm{C}}^{\mathrm{vdW}}$, as pointed by Romaner *et al.* [39]. Note that the $Z_{\mathrm{C}}^{\mathrm{DFT-D}}$ is smaller than the values calculated by the MP2 method [77, 78, 79], although the $\Delta\phi$'s calculated by the two methods are almost the same. The discrepancy in Z_{C}'s between the two calculations may be partly due to different modeling of the metal surfaces, i.e. the slab model and the cluster model. In the cluster model, neglect of depolarization effects possibly overestimates the magnitude of the work function change [95]. Note that Rohlfing *et al.* [96] showed that it is possible to predict a correct adsorption distances of PTCDA on Ag from first-principles. This approach is, however, computationally very demanding. On the other hand, the DFT-D method may be equally accurate with relatively low computational cost. Thus, in the following electronic structure analysis, the adsorption

Table 3.2: The work function changes ($\Delta\phi$) calculated by GGA at $Z_{\rm C}^{\rm GGA}$, $Z_{\rm C}^{\rm DFT-D}$, and $Z_{\rm C}^{\rm vdW}$, along with the experimentally work function change ($\Delta\phi^{\rm exp}$) for benzene on Cu(111), Ag(111), and Au(111).

Surface	GGA		MP2	Expt.
	$Z_{\rm C}$ / nm	$\Delta\phi$ / eV	$\Delta\phi$ / eV	$\Delta\phi^{\rm exp}$ /eV
Cu(111)	$Z_{\rm C}^{\rm DFT-D}$=0.29	-1.09	-1.08[a]	-1.05[a]
	$Z_{\rm C}^{\rm GGA}$, $Z_{\rm C}^{\rm vdW}$=0.37	-0.33	—	—
Ag(111)	$Z_{\rm C}^{\rm DFT-D}$=0.29	-0.71	-0.77[b]	-0.70[c]
	$Z_{\rm C}^{\rm GGA}$, $Z_{\rm C}^{\rm vdW}$=0.37	-0.25	—	—
Au(111)	$Z_{\rm C}^{\rm DFT-D}$=0.31	-1.06	-0.87[a]	-1.10[a]
	$Z_{\rm C}^{\rm GGA}$, $Z_{\rm C}^{\rm vdW}$=0.37	-0.48	—	—

[a] Ref. [79].
[b] Ref. [77].
[c] Ref. [81].

distance obtained by DFT-D method will be used.

To single out the electronic factor contributing to the formation of the interface dipole, we investigated the vacuum level shifts using the same benzene coverage for the three metal surfaces. Thus, we rescaled $\Delta\phi$'s in Eq. (3.2) by using $n_{\rm metal} = n_{\rm Au(111)}$ and plotted the results in Fig. 3.4.

As seen in Fig. 3.4, the substrate dependences of $\Delta\phi$ on $Z_{\rm C}$ are almost the same for the three metal surfaces, which means S is near unity, that is to say, this interface is in the Schottky limit [Eq. (1.4)]. This is consistent with the previous results that the exchange effect is an important origin [77, 78, 79]. However, experimentally, the slope parameter for benzene on metal surfaces is evaluated to be ∼0.46, which is different from the above our result. This is due to the difference in the benzene-substrate distance and the surface molecular density on different substrates.

3.1.4 Electronic structure

To inspect the electronic structures of the adsorbed systems, we calculated the projected density of states (PDOS) onto the molecular orbitals. In Fig. 3.5, we display the PDOS of benzene molecular orbitals on Cu(111), Ag(111), and Au(111). Note that we included that the molecular orbitals upto

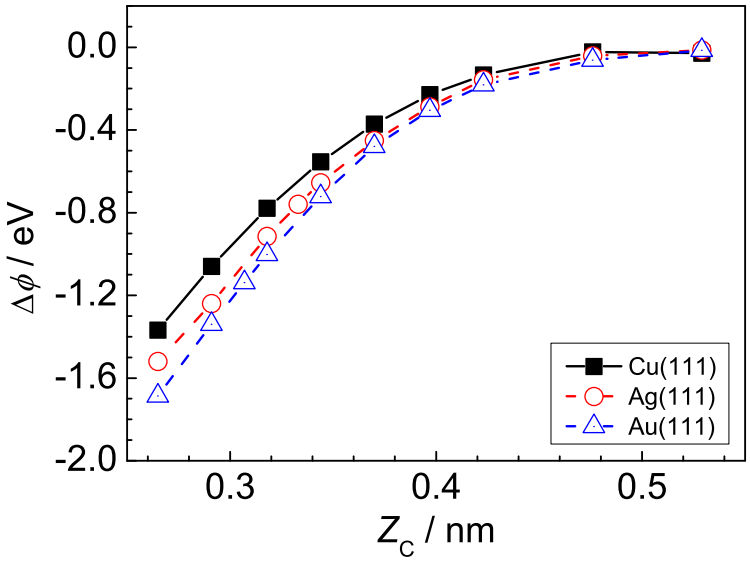

Figure 3.4: The work function change ($\Delta\phi$) as a function of Z_{C} for benzene on Cu(111), Ag(111), and Au(111) provided that the surface molecular densities on the three metal surfaces are assumed to be the same as $n_{\mathrm{Au(111)}}$.

LUMO+2 as the benzene molecular orbitals. The contribution of LUMO+3 to the bonding interaction between benzene and the substrate is not large because LUMO+3 is much higher than LUMO+2 by ∼1.0 eV, and therefore we did not include the LUMO+3 state.

On Cu, some magnitude of PDOS around -2 eV is found. Munakata and co-workers showed that there are enhancements of the *d*-band for benzene/Cu(111) at ∼2 eV below the Fermi energy (E_{F}) [87] and the occupied state for benzene/Cu(110) is at 2.2 eV below E_{F} [90]. Our calculated PDOS is in reasonable agreement with the experimental photoemission spectra. Moreover, the LUMO and the HOMO states are becomes slightly broader, because of the hybridization between the molecular orbitals and the substrate states. On Ag, the broadening of the LUMO and the HOMO states is almost the same as that for Cu, whereas that for Au is less than those for the other two metal surfaces. This means that the strength of the interaction of benzene with Au is weaker than those with Cu and Ag.

We calculated the projected density of states (PDOS) onto atomic *d* orbital of the metal atom circles in Fig. 3.1 for a clean surfaces and for the adsorbed system. In Fig. 3.6, we show the d_{z^2}-component of PDOS of the metal atom. For the three metal surfaces, the differences in the PDOS are not found, confirming that the interaction of benzene with the substrates is weak.

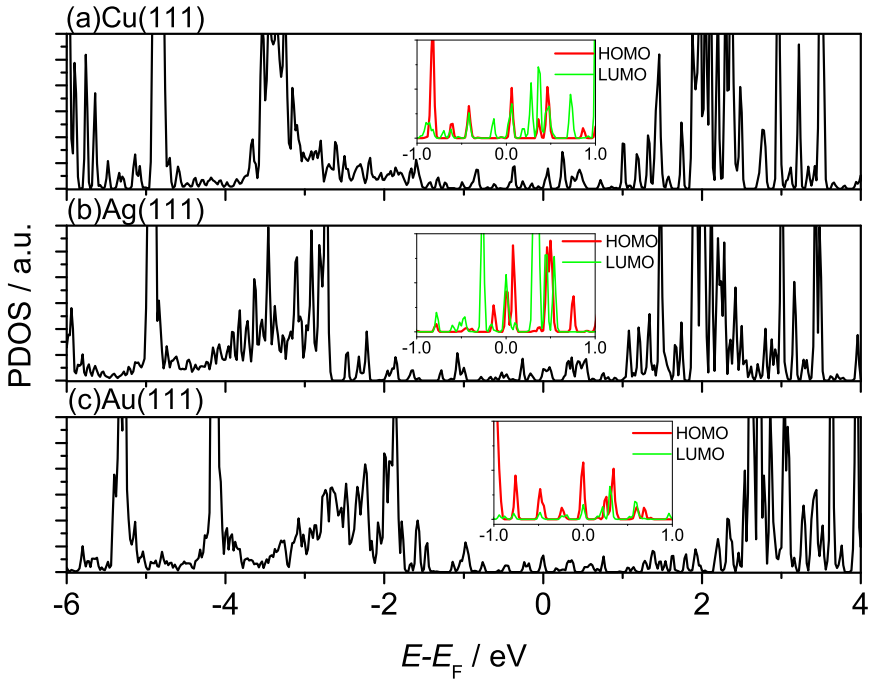

Figure 3.5: The projected density of states (PDOS) onto the molecular orbitals of benzene on (a) Cu(111), (b) Ag(111), and (c) Au(111). The energy zero is taken to be the Fermi energy of the adsorbed system. The HOMO and the LUMO parts of the PDOS near the Fermi energy are magnified in the insets

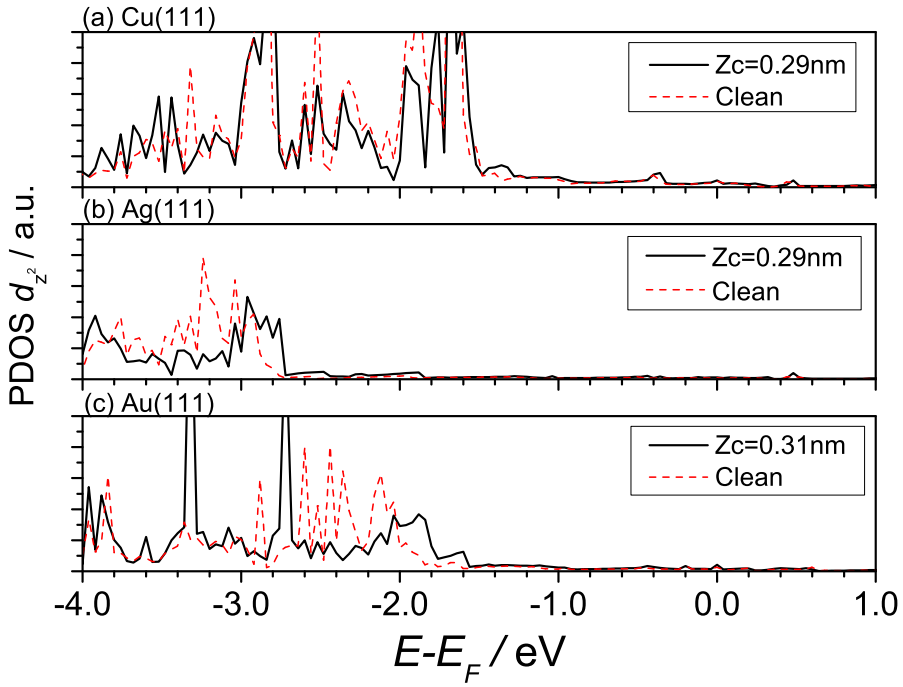

Figure 3.6: The d_{z^2}-component of the projected density of states (PDOS) of the metal atom circled in Fig. 3.1 for a clean surface (Clean) and for the adsorbed system (Z_{C}=$Z_{\mathrm{C}}^{\mathrm{DFT-D}}$), for (a) Cu(111), (b) Ag(111), and (c) Au(111)

3.2 Pentacene/Noble Metal

Pentacene ($C_{22}H_{14}$) is one of the most promising organic compounds for OFETs [50]. The interaction between pentacene and metal surfaces has therefore been studied extensively both experimentally and theoretically [40, 60, 97, 98, 99, 100, 101, 102, 103, 104, 105, 106, 107, 108, 109, 110, 111, 112, 113, 114]. Koch *et al.* studied pentacene on a Cu(111) surface to estimate the vacuum level shift and the adsorption geometry using ultraviolet photoelectron spectroscopy (UPS) and XSW measurements [40]. Ferretti *et al.* [98] and Yamane *et al.* [99, 100] observed the mixing of pentacene molecular orbitals and Cu substrate states using angle-resolved UPS (ARUPS), which indicated that the interaction between pentacene and Cu surfaces is not simple physisorption. Koch *et al.* studied pentacene on Ag(111) [103] and Au(111) [106] surfaces to estimate the vacuum level shift and hole injection barrier using UPS. Watkins *et al.* [111] studied pentacene on several surfaces to estimate the dependence of the interface dipole on the substrate work function using UPS. As mentioned above, the pentacene-Cu(111) distance has been determined experimentally [40]. Thus, the pentacene/metal interfaces are ideal systems to systematically investigate the origins of the interface dipole and to compare the calculated results with experimental ones in detail.

3.2.1 Calculation model

Figure 3.7 shows the calculation model for pentacene adsorbed on noble metal surfaces.

The surface unit cell of $(\sqrt{43} \times \sqrt{7})$ is used for a Cu(111) surface, whereas the cell of $(6 \times \sqrt{7})$ is used for Ag(111) and Au(111) surfaces. A (2×4) **k**-point mesh was used to sample the surface Brillouin zone. The number of the slab is four, because we confirmed that the adsorption energy and the work function change derived from a four-layer slab is almost the same as those derived from a six-layer slab. It has been shown experimentally, using scanning tunneling microscopy (STM) [101], that the center of a pentacene molecule is located at an hcp hollow site of Cu(111) with the long molecular axis aligned with the close-packed metal atom rows. We also confirmed that in the pentacene/Cu(111) system, the adsorption energy and the work function change are almost unchanged when the molecular center is moved to an fcc-hollow site. Thus, we assumed that the center of the pentacene molecule is located at an hcp-hollow site on the (111) surfaces as shown in Fig. 3.7.

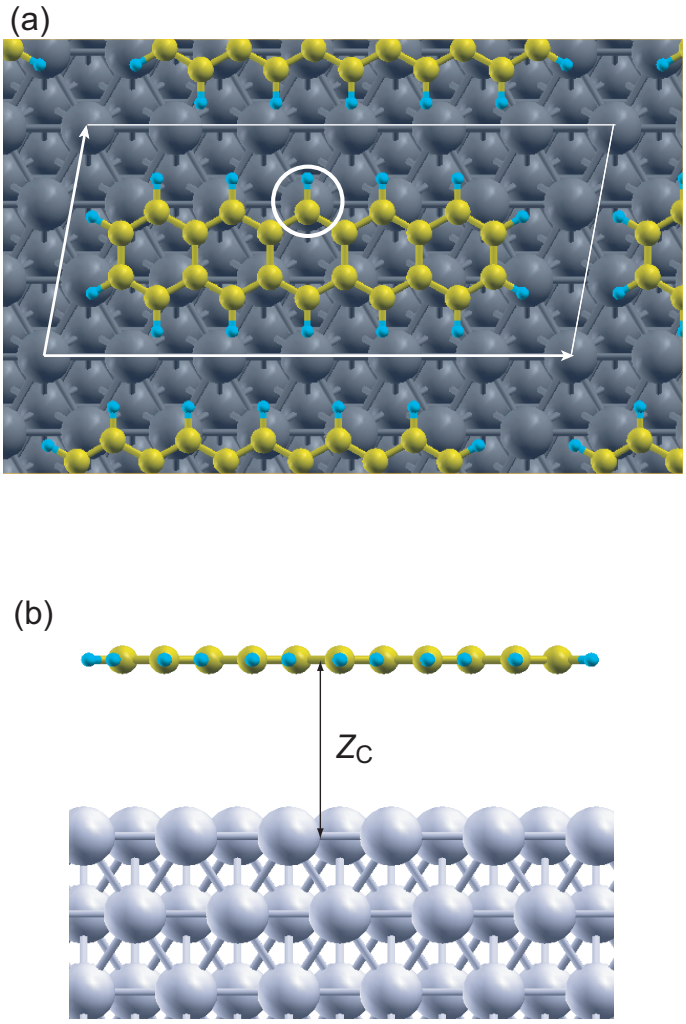

Figure 3.7: (a) Plane view and (b) cross-sectional view of pentacene on a (111) surface. The surface unit cell is $(6 \times \sqrt{7})$.

3.2.2 Adsorption energy

Figure 3.8 (a)-(c) shows E_{ad} of pentacene on Cu(111), Ag(111), and Au(111) as a function of Z_{C} using GGA, DFT-D, and vdW-DF. As shown in Fig. 3.8 (a)-(c), the potential energy curves calculated by GGA have shallow minima, whereas those calculated by DFT-D and vdW-DF have deeper minima, which is similar to the case of benzene. Table 3.3 summarizes the equilibrium distances ($Z_{\mathrm{C}}^{\mathrm{GGA}}$, $Z_{\mathrm{C}}^{\mathrm{DFT-D}}$, and $Z_{\mathrm{C}}^{\mathrm{vdW}}$) and the adsorption energies ($E_{\mathrm{ad}}^{\mathrm{GGA}}$, $E_{\mathrm{ad}}^{\mathrm{DFT-D}}$, and $E_{\mathrm{ad}}^{\mathrm{vdW}}$) calculated by GGA, DFT-D, and vdW-DF, respectively.

Table 3.3: The equilibrium distances ($Z_{\mathrm{C}}^{\mathrm{GGA}}$, $Z_{\mathrm{C}}^{\mathrm{DFT-D}}$, and $Z_{\mathrm{C}}^{\mathrm{vdW}}$), and the adsorption energies ($E_{\mathrm{ad}}^{\mathrm{GGA}}$, $E_{\mathrm{ad}}^{\mathrm{DFT-D}}$, and $E_{\mathrm{ad}}^{\mathrm{vdW}}$) calculated by GGA, DFT-D and vdW-DF, respectively, along with the experimentally determined adsorption distance ($Z_{\mathrm{C}}^{\mathrm{exp}}$) and adsorption energies ($E_{\mathrm{ad}}^{\mathrm{exp}}$)for pentacene on Cu(111), Ag(111), and Au(111)

	Surface	Cu(111)	Ag(111)	Au(111)
GGA	$Z_{\mathrm{C}}^{\mathrm{GGA}}$ / nm	0.42	0.37	0.37
	$E_{\mathrm{ad}}^{\mathrm{GGA}}$ / eV	0.090	-0.108	-0.136
DFT-D	$Z_{\mathrm{C}}^{\mathrm{DFT-D}}$ / nm	0.24	0.29	0.32
	$E_{\mathrm{ad}}^{\mathrm{DFT-D}}$ / eV	-1.61	-2.28	-2.51
vdW-DF	$Z_{\mathrm{C}}^{\mathrm{vdW}}$ / nm	0.37	0.37	0.37
	$E_{\mathrm{ad}}^{\mathrm{vdW}}$ / eV	-1.47	-1.62	-1.66
Expt.	$Z_{\mathrm{C}}^{\mathrm{exp}}$ / nm	0.234[a]	—	—
	$E_{\mathrm{ad}}^{\mathrm{exp}}$ / eV	-1.6[b]	-1.5[c]	-1.1[d]

[a] Ref. [40].
[b] Ref. [108, 115, 116].
[c] Ref. [104, 105].
[d] Ref. [108].

The $E_{\mathrm{ad}}^{\mathrm{vdW}}$ values are -1.47, -1.62, and -1.66 eV for Cu, Ag, and Au, respectively. For Cu and Ag, they are in good agreement with the experimental values of -1.6 and -1.5 [104, 105], respectively, whereas for Au, the absolute value is slightly overestimated by ∼0.5 eV compared with the experimental value of -1.1 eV [108]. It should be noted that we estimated the adsorption energy of the pentacene/Cu interface from that of the pentacene/Au interface in Ref. [108] using the proportional relation between adsorption

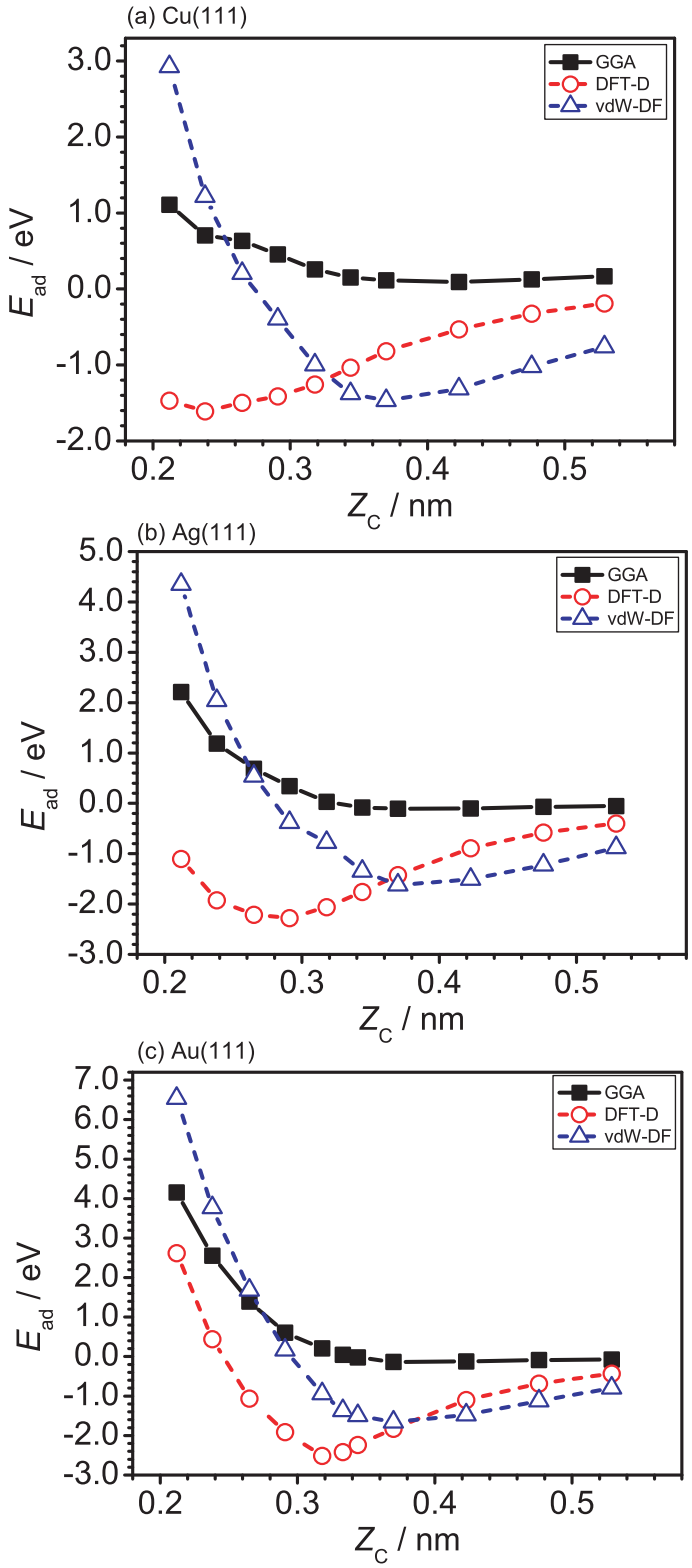

Figure 3.8: The adsorption energy (E_{ad}) as a function of the distance between the molecule and the metal surface (Z_{C}) using GGA, DFT-D, and vdW-DF for pentacene on (a) Cu(111), (b) Ag(111), and (c) Au(111)

energy and desorption temperature in first-order desorption kinetics [115, 116]. The $E_{\rm ad}^{\rm DFT-D}$ values are -1.61, -2.28, and -2.51, respectively. For Cu, the value is in good agreement with the experimental value, whereas for Ag and Au, the absolute values are slightly overestimated by ∼1.0 eV. This is similar to the case of benzene. The $E_{\rm ad}^{\rm GGA}$ values are 0.090, -0.108, and -0.136 eV for Cu, Ag, and Au, respectively. For Cu, the sign of the value is reversed, and for Ag and Au, the values are an order of magnitude smaller than the experimental values. These results indicates the the interaction between pentacene and close-packed noble metal surfaces is predominantly due to the dispersion interactions.

For Cu, the calculated $Z_{\rm C}^{\rm DFT-D}$ is 0.24 nm, which is in excellent agreement with the experimental value of 0.234 nm [40]. On the other hand, $Z_{\rm C}^{\rm GGA}$ and $Z_{\rm C}^{\rm vdW}$ are 0.42 and 0.37 nm, respectively. being significantly overestimated by 0.13∼0.18 nm. For Ag and Au, the pentacene-substrate distances have never been measured experimentally. However, as will be discussed later, by comparing the calculated vacuum level shifts with the experimental ones, we confirm the similar trend to the case of benzene. Thus, we conclude that the DFT-D method gives reasonable pentacene-metal distance.

3.2.3 Vacuum level shift and slope parameter

The vacuum level shift is calculated from the work function change ($\Delta\phi$), and $\Delta\phi$ is estimated [Eqs. (3.2) and (3.3)]. For Ag and Au, $n_{\rm Ag(111)}$ and $n_{\rm Au(111)}$ are based on the experimental data of pentacene on Ag(111) [105] and Au(111) [108], respectively. Because the surface molecular density on Cu(111) have been never measured experimentally, we estimated $n_{\rm Cu(111)}$ by

$$n_{\rm Cu(111)} = n_{\rm Au(111)} \frac{n_{\rm Cu(110)}}{n_{\rm Au(110)}}, \tag{3.4}$$

where $n_{\rm Cu(110)}$ and $n_{\rm Au(110)}$ are the experimental values for pentacene on Cu(110) [102] and Au(110) [110], respectively. In this way, the work function changes ($\Delta\phi$) are scaled from the bare calculated values ($\Delta\phi'$) by factors 1.05, 1.00, and 1.46 for Cu, Ag, and Au, respectively.

Figure 3.9 shows $\Delta\phi$ of pentacene adsorbed on Cu(111), Ag(111), and Au(111) as a function of $Z_{\rm C}$ using GGA. The experimentally determined work function changes on Cu(111) [40], Ag(111) [103], and Au(111) [106, 107] are indicated by horizontal dashed lines, whereas the experimentally deter-

mined pentacene-Cu(111) distance [$Z_{\rm C}$(Cu)][40] and the equilibrium distances Ag(111) and Au(111) [$Z_{\rm C}^{\rm DFT-D}$(Ag) and $Z_{\rm C}^{\rm DFT-D}$(Au)] calculated by DFT-D are shown by vertical dotted lines. Table 3.4 summarizes $\Delta\phi$'s calculated by GGA at several distances for pentacene on Cu(111), Ag(111), and Au(111). For Cu, the calculated $\Delta\phi$ at $Z_{\rm C}^{\rm exp}$, or $Z_{\rm C}^{\rm DFT-D}$ is in good agreement with the experimental value of 0.90 eV [40]. For Ag and Au, the calculated $\Delta\phi$'s at $Z_{\rm C}^{\rm DFT-D}$ are in very satisfying agreement with the experimental values of -0.50 [103] and -0.95 eV [106, 107], respectively. On the other hand, for the three metal surfaces, the absolute values of the calculated $\Delta\phi$ at $Z_{\rm C}^{\rm GGA}$ and $Z_{\rm C}^{\rm vdW}$ are significantly underestimated. Thus, in the following electronic structure analysis, the adsorption distance obtained by DFT-D method will be used.

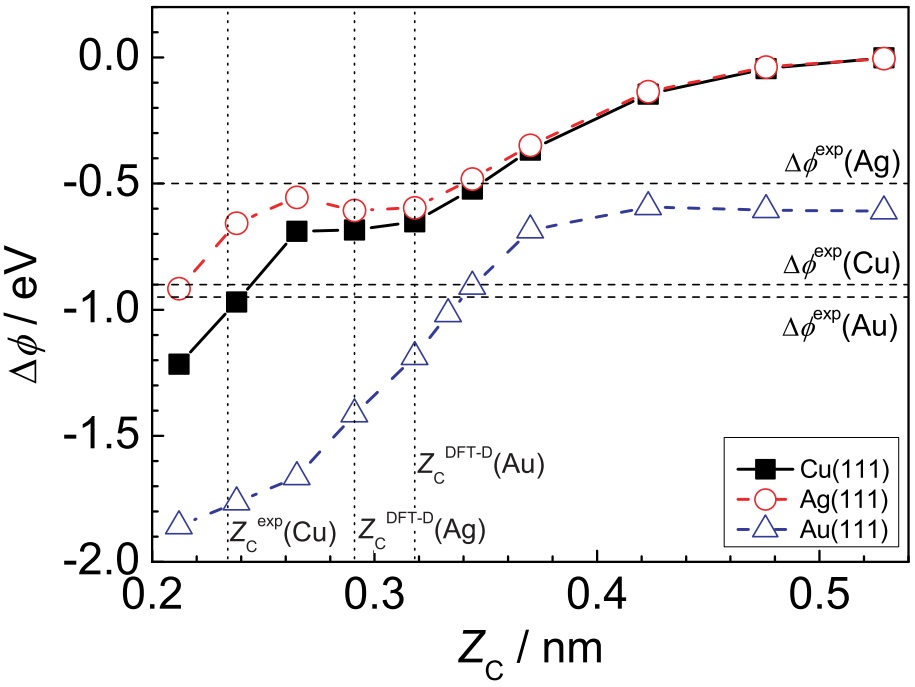

Figure 3.9: The work function change ($\Delta\phi$) as a function of $Z_{\rm C}$ for pentacene on Cu(111), Ag(111), and Au(111). The experimental values of $\Delta\phi$ on Cu(111), Ag(111), and Au(111) are shown by horizontal dashed lines. The experimentally observed pentacene-Cu(111) distance ($Z_{\rm C}^{\rm exp}$(Cu), and the equilibrium distance on Ag(111), and Au(111) ($Z_{\rm C}^{\rm DFT-D}$(Ag) and $Z_{\rm C}^{\rm DFT-D}$(Au)) calculated by DFT-D are shown by vertical dotted lines.

To clarify important factors that contribute to the formation of interface dipoles, we calculated the vacuum level shifts using the same pentacene coverage for Cu(111), Ag(111), and Au(111) surfaces. We rescaled $\Delta\phi'$ in Eq. (3.2) by using $n_{\rm metal} = n_{\rm Au(111)}$ and plotted the results in Fig. 3.10(a). Therefore, the different behavior of the vacuum level shifts on Cu(111), Ag(111), and Au(111) surfaces shown in Fig. 3.10(a) purely comes from the difference in the electronic structures of the three substrates. As

Table 3.4: The work function changes ($\Delta\phi$) calculated by GGA at $Z_{\mathrm{C}}^{\mathrm{GGA}}$, $Z_{\mathrm{C}}^{\mathrm{DFT-D}}$, and $Z_{\mathrm{C}}^{\mathrm{vdW}}$, along with the experimentally work function change ($\Delta\phi^{\mathrm{exp}}$) for pentacene on Cu(111), Ag(111), and Au(111).

Surface	GGA		Expt.	
	Z_{C} / nm	$\Delta\phi$ / eV	$Z_{\mathrm{C}}^{\mathrm{exp}}$ / nm	$\Delta\phi^{\mathrm{exp}}$ /eV
Cu(111)	$Z_{\mathrm{C}}^{\mathrm{DFT-D}}$=0.24	-0.97	-0.234[a]	-0.90[a]
	$Z_{\mathrm{C}}^{\mathrm{vdW}}$=0.37	-0.37	—	—
	$Z_{\mathrm{C}}^{\mathrm{GGA}}$=0.42	-0.15	—	—
Ag(111)	$Z_{\mathrm{C}}^{\mathrm{DFT-D}}$=0.29	-0.61	—	-0.50[b], -0.70[c]
	$Z_{\mathrm{C}}^{\mathrm{GGA}}$, $Z_{\mathrm{C}}^{\mathrm{vdW}}$=0.37	-0.25	—	—
Au(111)	$Z_{\mathrm{C}}^{\mathrm{DFT-D}}$=0.32	-1.19	—	-0.95[d], -1.0[c]
	$Z_{\mathrm{C}}^{\mathrm{GGA}}$, $Z_{\mathrm{C}}^{\mathrm{vdW}}$=0.37	-0.69	—	—

[a] Ref. [40].
[b] Ref. [103].
[c] Ref. [111].
[d] Ref. [106, 107].

seen in Fig. 3.10(a), the vacuum level shifts ($\Delta\phi$) on Cu(111) and Ag(111) are quite similar to each other, whereas that on Au(111) is different from those on the other two surfaces. It should be noted that on Au, $\Delta\phi$ at $Z_{\mathrm{C}} > 0.42$ nm converges to a negative value of ∼-0.6 eV. This unreasonable behavior comes from the artificial electron transfer from pentacene to the substrate, as will be shown in the last part of 3.2.4, and in reality, it should converge to zero at large Z_{C}, coinciding with those on the other two substrates. For Au, as Z_{C} decreases, $\Delta\phi$ monotonously decreases, presumably because of the push back (Pauli repulsion) effect. On the contrary, $\Delta\phi$'s take plateau-like shape at around 0.26 nm $< Z_{\mathrm{C}} <$ 0.32 nm. As will be further discussed in the next session, the hybridization between the pentacene LUMO and the substrate states takes place at $Z_{\mathrm{C}} <$ ∼0.3 nm, and therefore the plateau comes from the counter-polarization because of the back donation from the substrate to the pentacene.

To further clarify the substrate dependence of interface dipole, we plotted $\Delta\phi$ as a function of the substrate work function (ϕ_{m}) at several Z_{C}'s (0.21, 0.24, 0.29, and 0.37 nm) in Fig. 3.10(b) and k is evaluated at each Z_{C}. Although experimentally observed k values do not correspond to those estimated at fixed Z_{C}, we would like to single out the effect of the electronic factor from the geometric factors. As seen in Fig 3.10(a), at $Z_{\mathrm{C}} > 0.34$ nm, $\Delta\phi$ depends weakly on the work function of the substrate, and k is evaluated to be -0.34 at $Z_{\mathrm{C}} = 0.37$ nm. Note that k at $Z_{\mathrm{C}} = 0.53$ nm could be near zero, because $\Delta\phi$'s for the three metal surfaces should be converged to zero. On the other hand, at $Z_{\mathrm{C}} < 0.34$ nm, $\Delta\phi$ varies with the work function of the substrate, because of the different magnitude of the hybridization between the pentacene molecular orbitals and the substrate states. For example, k at $Z_{\mathrm{C}} = 0.29$, 0.24, and 0.21 nm are evaluated to be -0.97, -1.32, and -0.89, respectively(Fig. 3.10(b)). Our calculations show that as pentacene molecule approaches the substrate, k decreases from 0 to nearly -1.0 and consequently S decreases from 1 to nearly 0 [Eq. (1.4)]. This result suggests a transition from the Schottky limit to the Bardeen limit, which is consistent with the intuitive explanation that the interface is in the Schottky limit if the pentacene-substrate interaction is weak whereas the interface is in the Bardeen limit if the interaction is strong. Experimentally, the slope parameter for pentacene on several substrate is evaluated to be ∼0.5 eV [112], which is an intermediate between the two limits. As described, this is due to the difference in the pentacene-substrate distance and the surface molecular density on difference substrates.

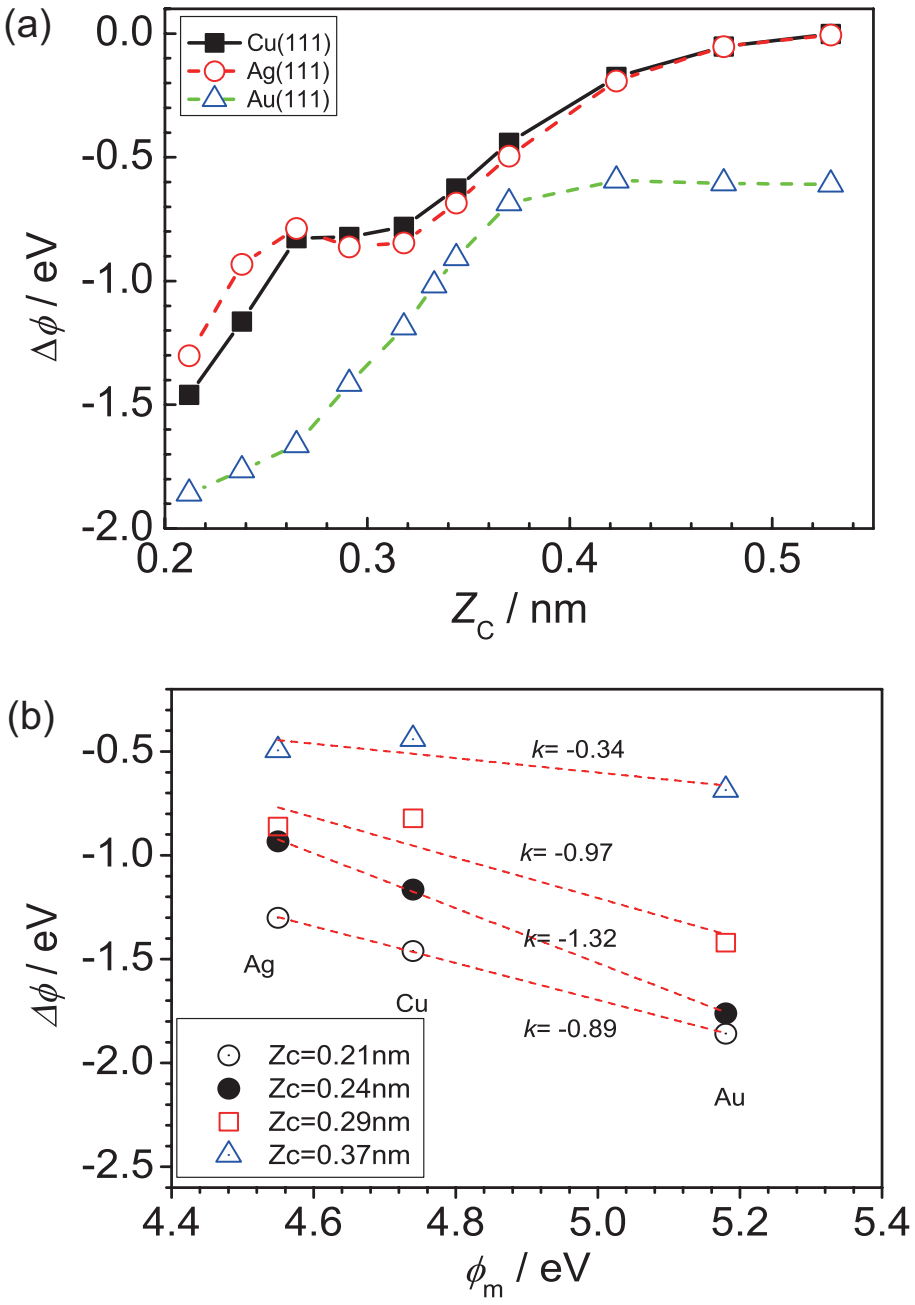

Figure 3.10: (a)The work function change ($\Delta\phi$) as a function of Z_C for benzene on Cu(111), Ag(111), and Au(111) provided that the surface molecular densities on the three metal surfaces are assumed to be the same as $n_{Au(111)}$. (b)$\Delta\phi$ as a function of the metal work function (ϕ_m) at Z_C = 0.21, 0.24, 0.29, and 0.37 nm. k indicates the slope of the line of $\Delta\phi$ as a function of ϕ_m at each Z_C.

3.2.4 Electronic structure

To inspect the electronic structures of the adsorbed systems, we calculated the projected density of states (PDOS) onto the molecular orbitals. In Fig. 3.11, we display the PDOS of pentacene molecular orbitals on Cu(111), Ag(111), and Au(111). Note that we included that the molecular orbitals upto LUMO as the pentacene molecular orbitals. The contribution of LUMO+1 is much higher than LUMO by ∼1.3 eV, and therefore we did not include the LUMO+1 state.

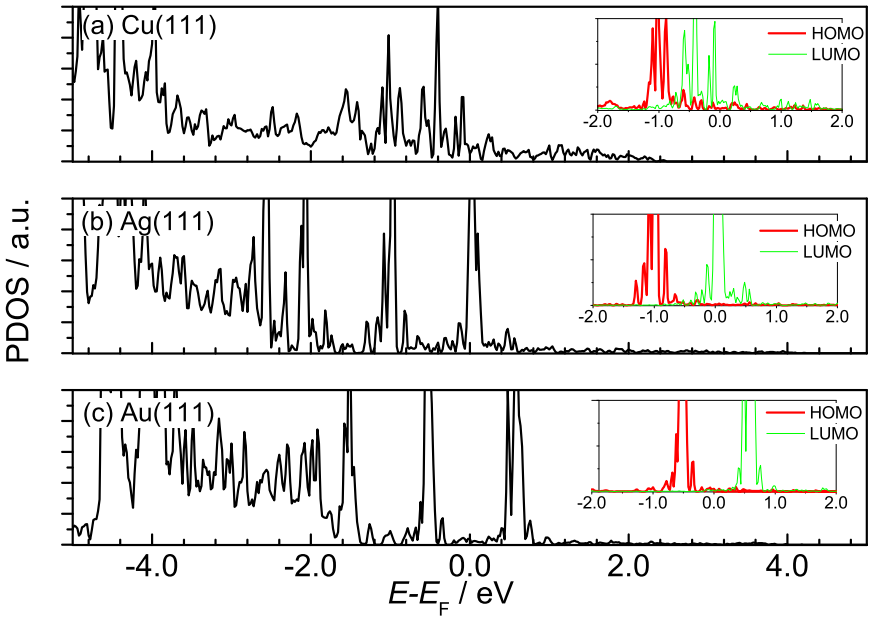

Figure 3.11: The projected density of states (PDOS) onto the molecular orbitals of pentacene on (a) Cu(111), (b) Ag(111), and (c) Au(111). The energy zero is taken to be the Fermi energy of the adsorbed system. The HOMO and the LUMO parts of the PDOS near the Fermi energy are magnified in the insets

On Cu, the LUMO and HOMO peaks are located at -0.4 and -1.0 eV (energy zero is set to the Fermi energy), respectively. Experimentally, a hybrid gap state in the range of -0.5 to -1.0 eV and HOMO at -1.3 eV are observed [40], being in reasonable agreement with our calculated results. On Ag and Au, the HOMO peak is located at -0.96 eV and -0.52, which correspond well to experimentally observed HOMO peaks derived at -1.5 eV [103] and -0.9 eV [106], respectively. On Cu, the hybridization between the molecular orbitals and the substrate states is strongest among the three substrates and both LUMO and the HOMO states are significantly broadened. On Ag, the hybridization is intermediate, i.e. in between

Cu and Au cases, and the LUMO state is partially filled. On Au the LUMO and HOMO peaks are sharp, and accordingly the molecular states are almost the same as those of an isolated molecule.

We calculated the projected density of states (PDOS) onto atomic d orbital of the metal atom circles in Fig. 3.7 for a clean surfaces and for the adsorbed system. In Fig. 3.12, we show the d_{z^2}-component of PDOS of the metal atom. Note that we confirmed that hybridization compared with other components. On Cu, broadening of the d states due to the hybridization can be observed. On the other hand, such a broadening is not observed on Ag and Au, confirming that the weak interaction between pentacene and the two surfaces.

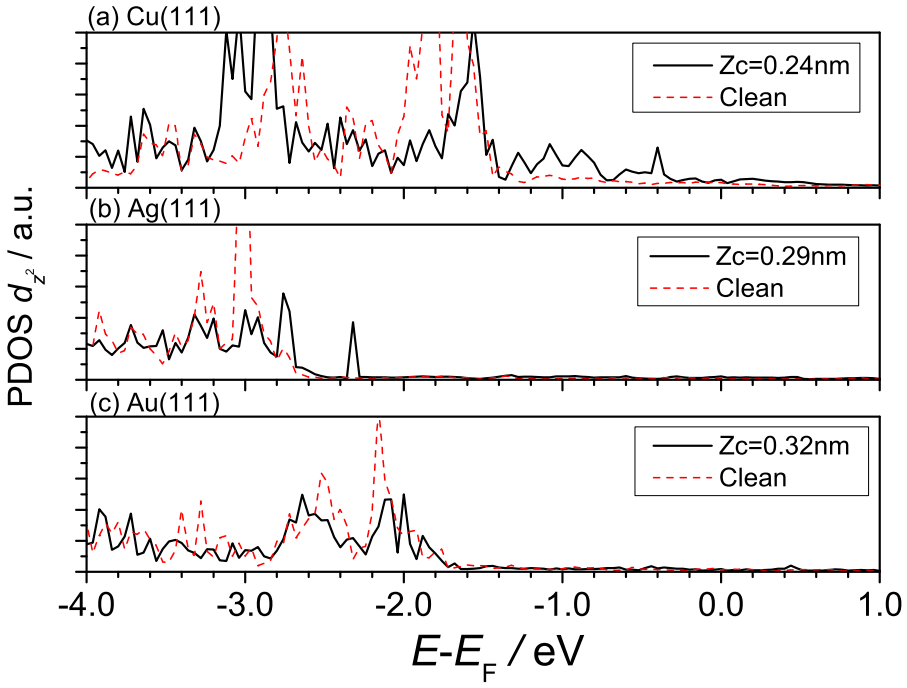

Figure 3.12: The d_{z^2}-component of the projected density of states (PDOS) of the metal atom circled in Fig. 3.7 for a clean surface (Clean) and for the adsorbed system (Z_C=Z_C^{DFT-D}), for (a) Cu(111), (b) Ag(111), and (c) Au(111)

There results show that for Au a physical factor dominates the pentacene-substrate interaction, whereas for Cu a chemical factor contribute to the interaction the pentacene LUMO and the substrate d states, and for Ag the adsorption state is between the two states. This is similar to the result of PTCDA on noble metals [117].

To visualize the hybridization between pentacene and the Cu(111) surface, we calculated the electron density difference for pentacene on Cu(111) at Z_C^{DFT-D}. The electron density difference $\delta\rho(\mathbf{r})$ is defined

by

$$\delta\rho(\mathbf{r}) = \rho^{\mathrm{A/S}}(\mathbf{r}) - \rho^{\mathrm{A}}(\mathbf{r}) - \rho^{\mathrm{A}}(\mathbf{r}), \tag{3.5}$$

where $\rho^{\mathrm{A/S}}(\mathbf{r})$, $\rho^{\mathrm{A}}(\mathbf{r})$, and $\rho^{\mathrm{A}}(\mathbf{r})$ are the electron densities of the adsorbed system, the isolated adsorbate, and the isolated substrate, respectively. In Fig. 3.13, we show the isosurfaces of the electron density difference for pentacene on Cu(111) at $Z_{\mathrm{C}}^{\mathrm{DFT-D}}$. Electrons are mainly accumulated in the middle part between the pentacene molecules and the Cu atoms, whereas electrons are reduced not only from the C atoms but also from the Cu atoms just below the pentacene molecules. The hybridization between pentacene molecular orbitals and the substrate states polarizes the pentacene molecules normal to their molecular plane toward the substrate. The large number of transferred electrons creates weak chemical bonds between pentacene molecules and the Cu surface: this can also be inferred from the results showing that back donation occurs. This is in line with the result of pentacene/Cu(100) [98].

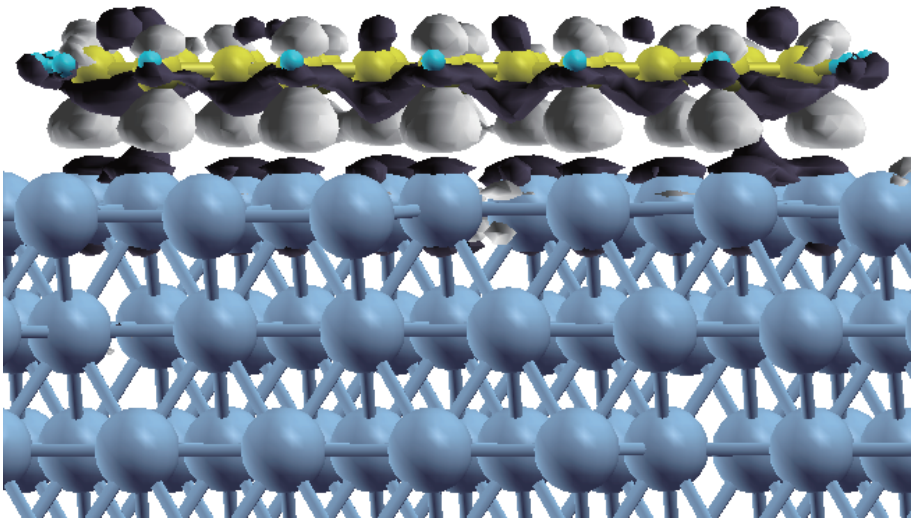

Figure 3.13: Isosurfaces of the electron density difference for pentacene on Cu(111) at $Z_{\mathrm{C}}^{\mathrm{DFT-D}}$. Light (dark) regions denote electron accumulation (electron depletion) compared to the non-interacting system. The isovalues are $\pm$ 0.01 electron/nm^3.

The artificial electron transfer from pentacene to Au substrate at $Z_C > 0.42$ nm

Figure 3.14 shows that the PDOS of pentacene on Cu(111), Ag(111), and Au(111) at $Z_C = 0.53$ nm. For Cu and Ag, HOMO is below the Fermi energy [Figs. 3.14 (a) and (b)], and electrons do not transfer from the pentacene to the substrate. On the other hand, for Au, HOMO is slightly above the Fermi energy of the adsorbed system [Fig. 3.14 (c)] and electrons artificially transfer from the pentacene to the substrate. This originates from the underestimation of the HOMO-LUMO gap of the pentacene molecule as is well in LDA or GGA calculations. In 3.1, we showed that benzene has such a large HOMO-LUMO gap that the artificial electron transfer does not take place.

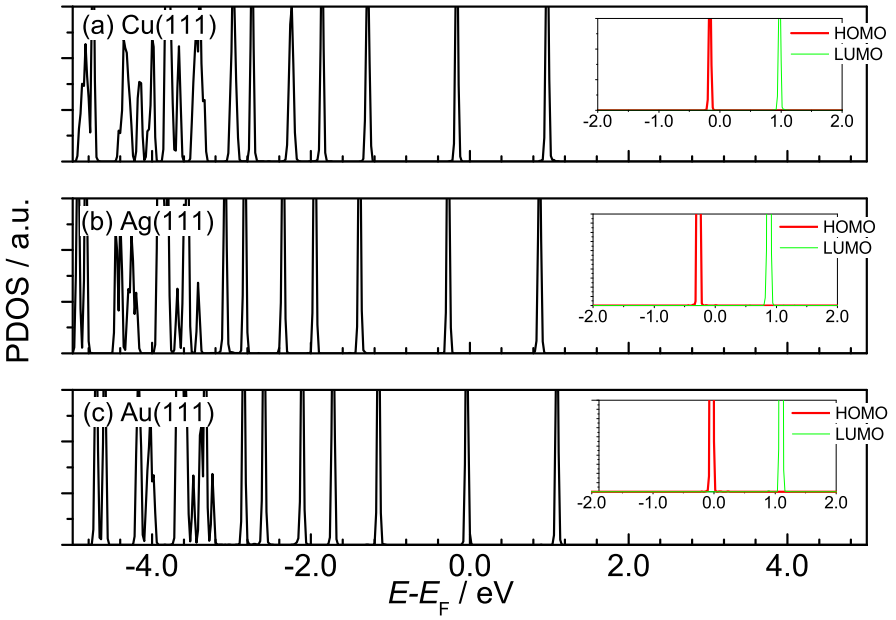

Figure 3.14: The projected density of states (PDOS) onto the molecular orbitals of pentacene on (a) Cu(111), (b) Ag(111), and (c) Au(111) at $Z_C = 0.53$ nm. The energy zero is taken to be the Fermi energy of the adsorbed system. The HOMO and the LUMO parts of the PDOS near the Fermi energy are magnified in the insets

3.2.5 Origin of Surface-Band at the Pentacene/Cu Interface

As shown in the preceding section, the pentacene/Cu interface is not simple physisorption. Yamane *et al.* observed intramolecular energy dispersion at Pentacene/Cu(110) interfaces using ARUPS [99, 100]. Annese *et al.* reported that the pentacene molecular orbitals (MO) derived states in pentacene/Cu(119) systems exhibit the energy dispersion using ARUPS, whereas the electron charge distribution of pentacene is very similar to that of the isolated molecule using STM [118]. The energy dispersion at pentacene/Cu interface is considered to originate from hybridization between the MOs and the substrate states, which significantly affects the electron transfer through the interface. However, the definitive origin of the intermolecular energy dispersion is yet to be clarified.

We have studied the surface-band structure of pentacene adsorbed on Cu(111) surface using first-principles calculations based on DFT. To investigate the origin of the energy dispersion, we conducted a Mulliken population analysis, and inspected the DOS projected onto the MOs of pentacene adsorbed on Cu(111).

Calculation model

Figure 3.15 shows the calculation model for pentacene adsorbed on a Cu(111) surface.

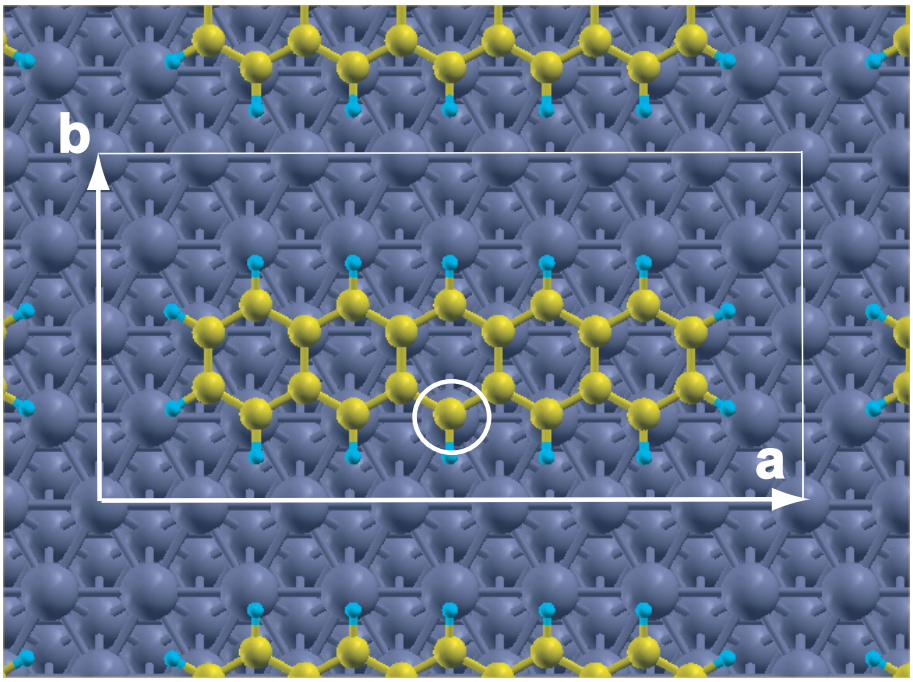

Figure 3.15: Plane view of pentacene on a Cu(111) surface.

The surface unit cell of $(7 \times 2\sqrt{3})$ is used. A (2×4) **k**-point mesh was used to sample the surface Brillouin zone. The number of the slab is four. The adsorption site and the direction of the molecular long axis is the same as those in the preceding section.

Electronic structure

To investigate the dispersion of the pentacene MO derived states, we first calculated k-resolved gross population (k-GPOP) of the pentacene MOs, using the Mulliken population analysis [119, 120]. At the pentacene/metal interface, the pentacene MOs hybridize with the substrate continuum states and their energy levels are shifted and broadened. The wave functions of the hybridized states were expanded by those of the separated pentacene and the metal substrate. k-GPOP indicates weight of contribution from the pentacene-MOs to each hybridized state.

Figure 3.16 shows the k-GPOP of pentacene of HOMO and LUMO along the reciprocal vector $\mathbf{a}^*$, and the DOS weighted by GPOP of pentacene HOMO and LUMO. The open circles in Fig. 3.16 indicates the energy positions of the largest peak in k-GPOP at each k-point. As shown in Fig. 3.16, the pentacene HOMO- and LUMO-derived states exhibit clear dispersion along the vector $\mathbf{a}^*$. The bandwidth of HOMO- (LUMO-)derived state is $\sim$0.08 (0.62) eV, which is consistent with the experimental results [99, 100]. The LUMO-derived state is located at -0.5$\sim$0.1 eV relative to E_{F}, indicating that the considerable hybridization of LUMO with the substrate states. Here, it is noteworthy that the surface-band dispersion is observed neither when we considered an isolated pentacene monolayer by removing the Cu substrate from the pentacene/Cu interface, nor when we calculated the band structure at $Z_{\mathrm{C}}^{\mathrm{vdW}}$. Furthermore, careful analysis of the electronic wave functions shows that there is negligible overlap between neighboring pentacene molecules as shown in Fig. 3.17. Thus, our calculations strongly suggest that the energy dispersion is due to the hybridization of pentacene HOMO and LUMO states with the Cu substrate, not to the overlap between pentacene MOs.

To inspect the effect of the hybridization on the surface-band dispersion in more detail, we calculated k-resolved crystal overlap population (k-COOP) using the Mulliken population analysis [119, 120]. The k-COOP indicates the character of the interaction between the pentacene MOs and the substrate wave functions for each hybridized state, i.e, a positive value means a bonding state whereas a negative value

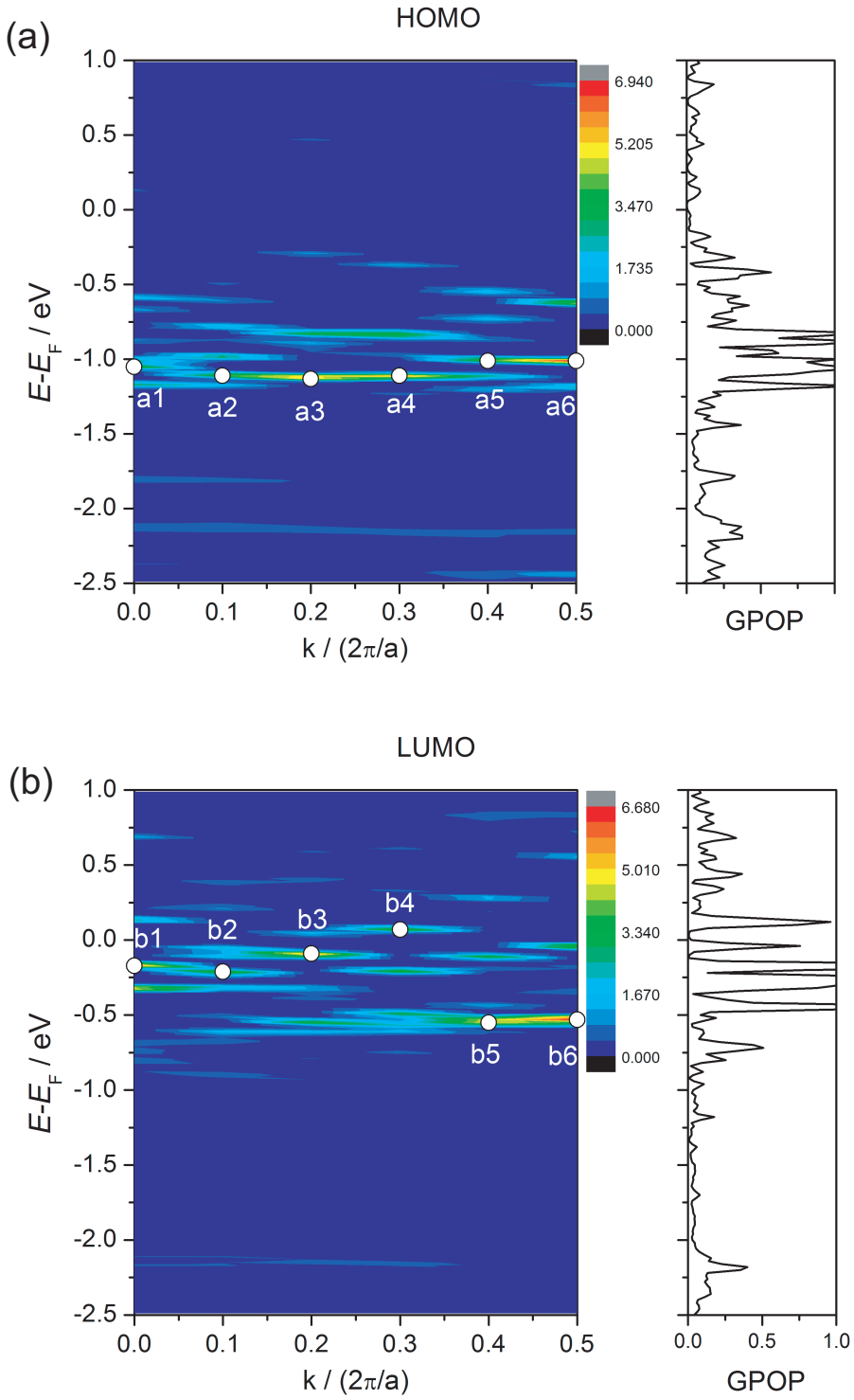

Figure 3.16: The left graphs show k-resolved gross population (k-GPOP) of HOMO (a) and LUMO (b) along the reciprocal vector $\mathbf{a}^*$. The right graphs show the density of states weighted by GPOP of pentacene HOMO (a) and LUMO (b). The open circles in the left graphs indicate the energy position of the largest peak in k-GPOP at each k-point. The energy zero is taken to be the Fermi energy of the adsorbed system.

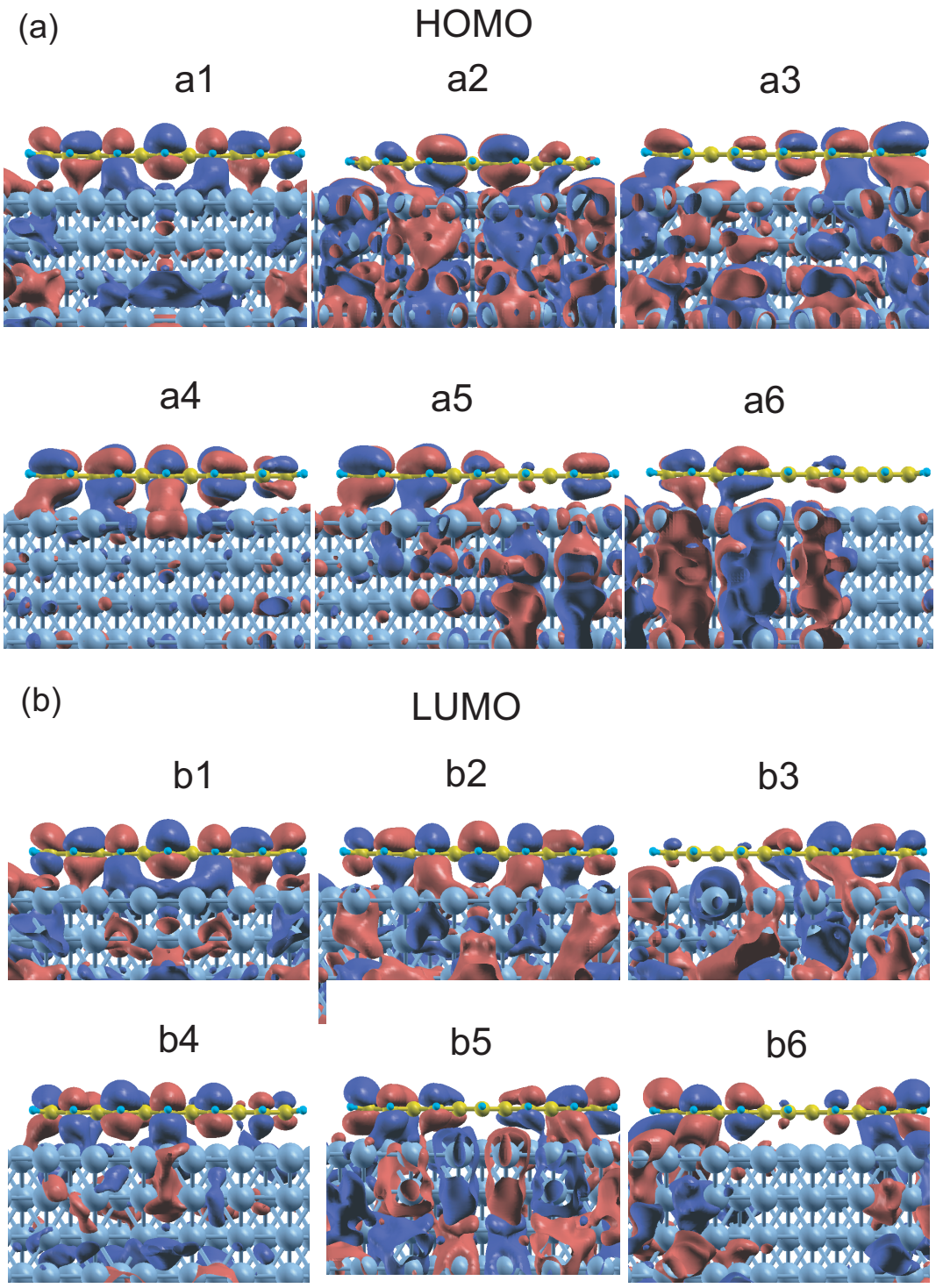

Figure 3.17: The wave functions of (a) HOMO-derived state and (b) LUMO-derived state at each k points. The labels of a1-a6 for the HOMO-derived band and b1-b6 for the LUMO-derived band correspond to those used in Fig. 3.16.

means an anti-bonding state.

Figure 3.18 shows k-COOP for pentacene HOMO and LUMO. HOMO-derived states at a1, a5, and a6 have anti-bonding character, whereas those at a2, a3, and a4 have bonding one. LUMO-derived states at b1, b2, b3, and b4 show anti-bonding character, whereas those at the other points show bonding one. Furthermore, the LUMO-derived states are much larger than those for the HOMO-derived ones, suggesting that LUMO dominated the hybridization. Our results clearly indicate that the energy dispersion of the HOMO- and LUMO-derived states can be ascribed to the bonding and anti-bonding interaction with the substrate states.

Figure 3.19 shows the k-resolved density of states projected onto the d_{z^2} orbital (PDOS) for a surface Cu atom circled in Fig. 3.15. PDOS for the clean surface is also shown for comparison. Positions of extra peaks appearing in the adsorbed system correspond to the LUMO- and HOMO-derived states observed in GPOP and COOP in Figs. 3.16 and 3.18, implying that the hybridization of pentacene LUMO and HOMO with the Cu substrate is due to the d_{z^2} state. We confirmed that the hybridization of the Cu d_{z^2}-component with pentacene MOs is significant compared with other d-components.

To summarize, our first-principles calculation reveals that the surface-band dispersion of pentacene adsorbed on a Cu surface is ascribed to the hybridization, especially to the wave-vector dependent bonding and anti-bonding interaction between pentacene LUMO with substrate d_{z^2} state.

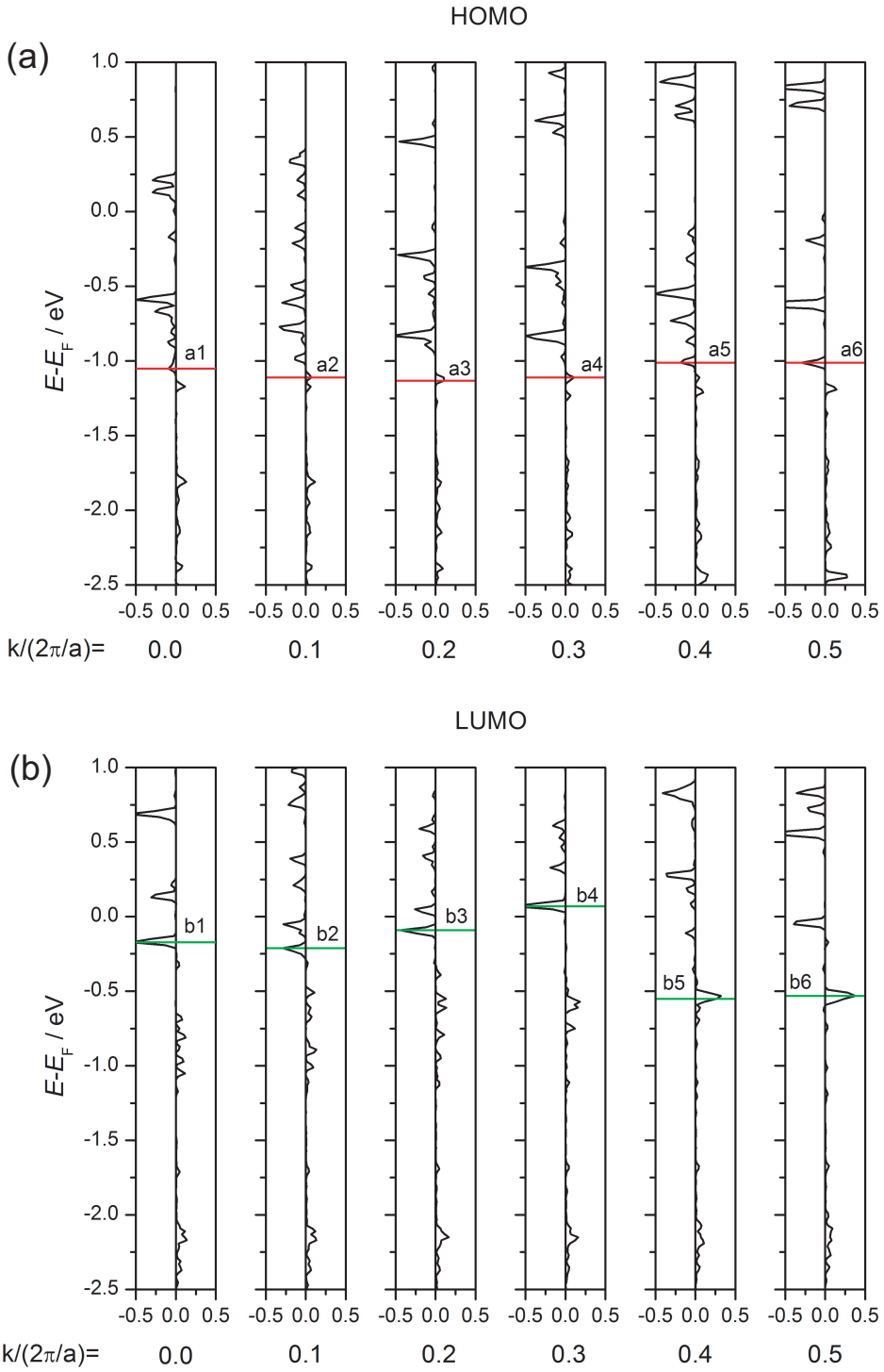

Figure 3.18: The k-resolved crystal orbital overlap population (k-COOP) of pentacene (a) HOMO-derived and (b) LUMO-derived states. The horizontal lines indicate peaks which correspond to those of k-GPOP in Fig. 3.16. The labels of a1-a6 for the HOMO-derived band and b1-b6 for the LUMO-derived band correspond to those used in Fig. 3.16.

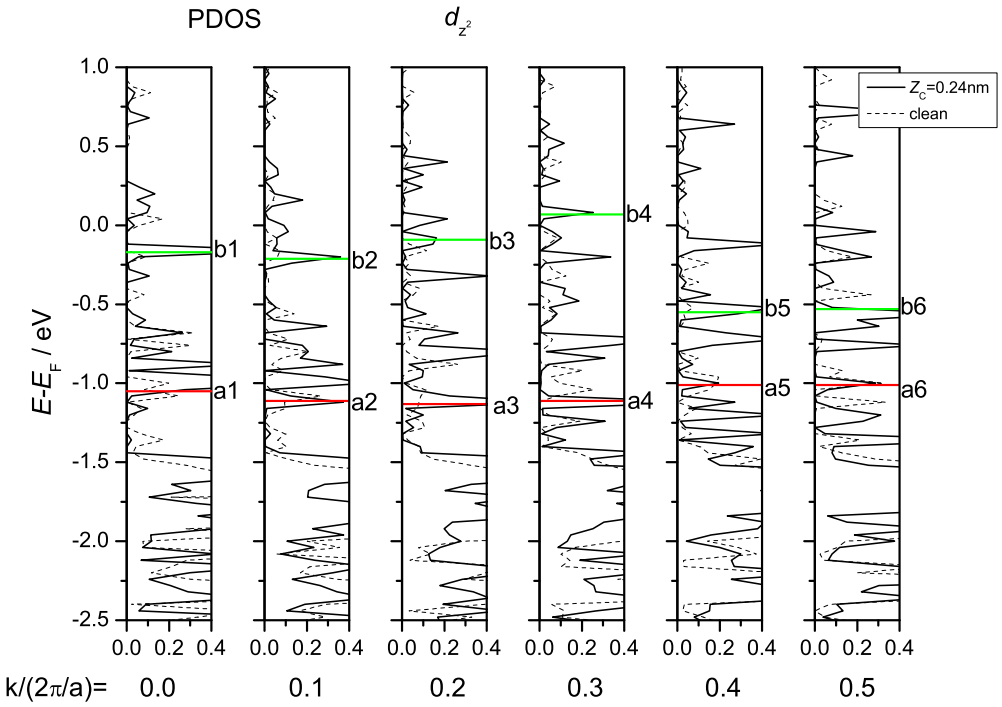

Figure 3.19: The k-resolved PDOS's for the d_{z^2}-component of a Cu atom in the first layer circled in Fig. 3.15 for a clean surface and for the adsorbed system. The horizontal lines indicate peaks with correspond to those of k-GPOP in Fig. 3.16. The labels of a1-a6 for the HOMO-derived band and b1-b6 for the LUMO-derived band correspond to those used in Fig. 3.16.

3.3 Perfluoropentacene/Noble Metal

Perfluoropentacene (PFP, $C_{22}F_{14}$) is examined as one of a few organic materials for n-type FET [51]. The ionization potential of PFP is 5.85 eV whereas that of pentacene is 5.0 eV, which indicates PFP is more chemically reactive than pentacene [40]. The interaction between PFP and metal surfaces has therefore been studied experimentally [40, 106]. Koch *et al.* studied PFP on a Cu(111) surface to estimate the vacuum level shift and the adsorption geometry using UPS and XSW measurements. They observed the molecular distortion by adsorption, which causes an intramolecular dipole [40]. Koch *et al.* also studied PFP on a Au(111) surface to estimate the vacuum level shift and electronic structure using UPS [106]. In contrast, the interaction between PFP and metal surfaces has never been studied theoretically.

As mentioned above, the PFP-Cu(111) distance has been determined experimentally, and the intramolecular dipole caused by geometric distortion of the molecule is pointed out as an origin of the interface dipole [40]. We investigate how the stronger chemical reactivity of PFP affects the interaction of the PFP molecule with metal surfaces.

3.3.1 Calculation model

Figure 3.20 shows the calculation model for PFP adsorbed on noble metal surfaces.

The surface unit cell of $(\sqrt{43} \times 2\sqrt{3})$ is used. Here, we assumed the surface unit cell which is commensurate with the Cu(111) surface unit cell on the basis of the experimental data of PFP adsorbed on Cu(111) using STM [40]. A (2×4) **k**-point mesh was used used to sample the surface Brillouin zone. The number of the slab is four, as for the case of pentacene. The center of the PFP molecule is located at an hcp-hollow site on the (111) surfaces with the long molecular axis aligned with the close-packed metal atom rows as shown in Fig. 3.20. Note that we assumed that the adsorption site of PFP is the same as that of pentacene adsorbed on Cu(111) [101].

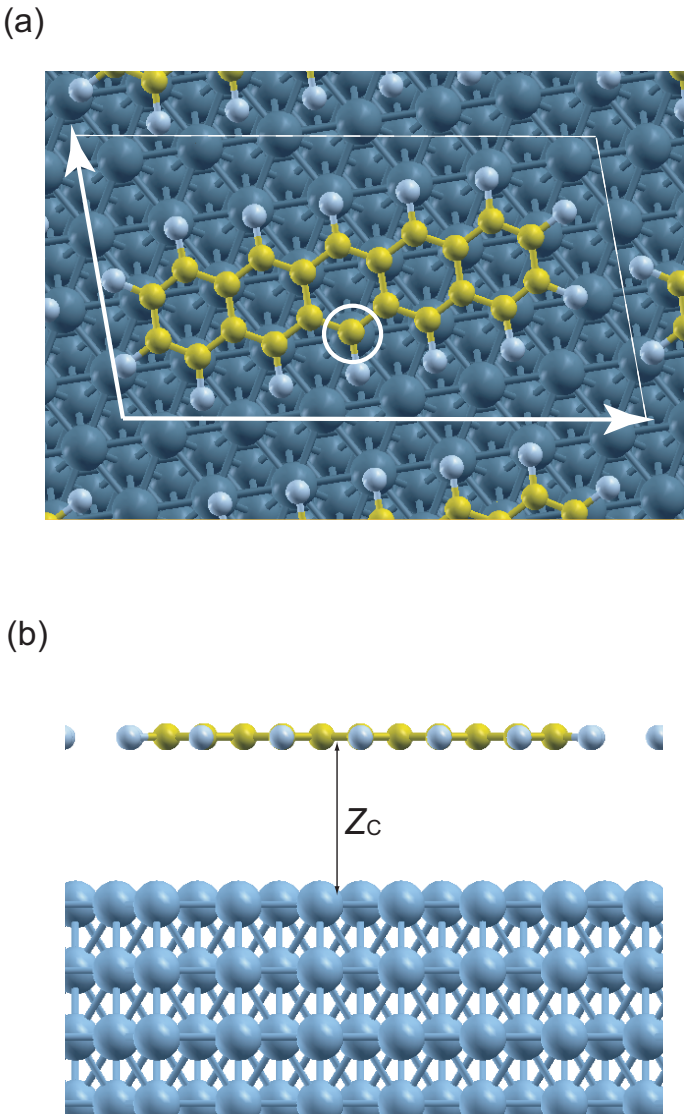

Figure 3.20: (a) Plane view and (b) cross-sectional view of PFP on a (111) surface

3.3.2 Adsorption energy

Figure 3.21 (a)-(c) shows E_{ad} of PFP on Cu(111), Ag(111), and Au(111) as a function of Z_{C} using GGA, DFT-D, and vdW-DF. As shown in Fig. 3.21 (a)-(c), the potential curves have shallow minima, whereas those by DFT-D and vdW-DF have deeper minima. The equilibrium distances calculated by DFT-D are smaller than those calculated by GGA and vdW-DF. Table 3.5 summarizes the equilibrium distances ($Z_{\mathrm{C}}^{\mathrm{GGA}}$, $Z_{\mathrm{C}}^{\mathrm{DFT-D}}$, and $Z_{\mathrm{C}}^{\mathrm{vdW}}$) and the adsorption energies ($E_{\mathrm{ad}}^{\mathrm{GGA}}$, $E_{\mathrm{ad}}^{\mathrm{DFT-D}}$, and $E_{\mathrm{ad}}^{\mathrm{vdW}}$) calculated by GGA, DFT-D, and vdW-DF, respectively.

Table 3.5: The equilibrium distances ($Z_{\mathrm{C}}^{\mathrm{GGA}}$, $Z_{\mathrm{C}}^{\mathrm{DFT-D}}$, and $Z_{\mathrm{C}}^{\mathrm{vdW}}$), and the adsorption energies ($E_{\mathrm{ad}}^{\mathrm{GGA}}$, $E_{\mathrm{ad}}^{\mathrm{DFT-D}}$, and $E_{\mathrm{ad}}^{\mathrm{vdW}}$) calculated by GGA, DFT-D and vdW-DF, respectively, along with the experimentally determined adsorption distance ($Z_{\mathrm{C}}^{\mathrm{exp}}$) for PFP on Cu(111), Ag(111), and Au(111)

	Surface	Cu(111)	Ag(111)	Au(111)
GGA	$Z_{\mathrm{C}}^{\mathrm{GGA}}$ / nm	0.37	0.42	0.42
	$E_{\mathrm{ad}}^{\mathrm{GGA}}$ / eV	0.011	-0.124	-0.082
DFT-D	$Z_{\mathrm{C}}^{\mathrm{DFT-D}}$ / nm	0.29	0.32	0.32
	$E_{\mathrm{ad}}^{\mathrm{DFT-D}}$ / eV	-2.17	-2.40	-2.68
vdW-DF	$Z_{\mathrm{C}}^{\mathrm{vdW}}$ / nm	0.34	0.37	0.37
	$E_{\mathrm{ad}}^{\mathrm{vdW}}$ / eV	-1.72	-1.71	-1.94
Expt.	$Z_{\mathrm{C}}^{\mathrm{exp}}$ / nm	0.298[a]	—	—

[a] Ref. [40].

The $E_{\mathrm{ad}}^{\mathrm{vdW}}$ values are -1.72, -1.71, and -1.94 eV for Cu, Ag, and Au, respectively, whereas the $E_{\mathrm{ad}}^{\mathrm{DFT-D}}$ values are -2.17, -2.40, and -2.68 eV for Cu, Ag, and Au, respectively. The differences between $E_{\mathrm{ad}}^{\mathrm{vdW}}$ and $E_{\mathrm{ad}}^{\mathrm{DFT-D}}$ for Ag and Au are larger than that for Cu. This is similar to the cases of benzene and pentacene. The $E_{\mathrm{ad}}^{\mathrm{GGA}}$ values are 0.011, -0.124, and -0.082 eV for Cu, Ag, and Au, respectively. For Cu, the sign of the value is reversed, and for Ag and Au, the values are an order of magnitude smaller than those calculated by the other two methods. Unfortunately, the adsorption energies for the systems studied in the present work have never measured experimentally, and we cannot compare the calculated adsorption energy with experimental one. However, in the preceding sections, we showed that the vdW-

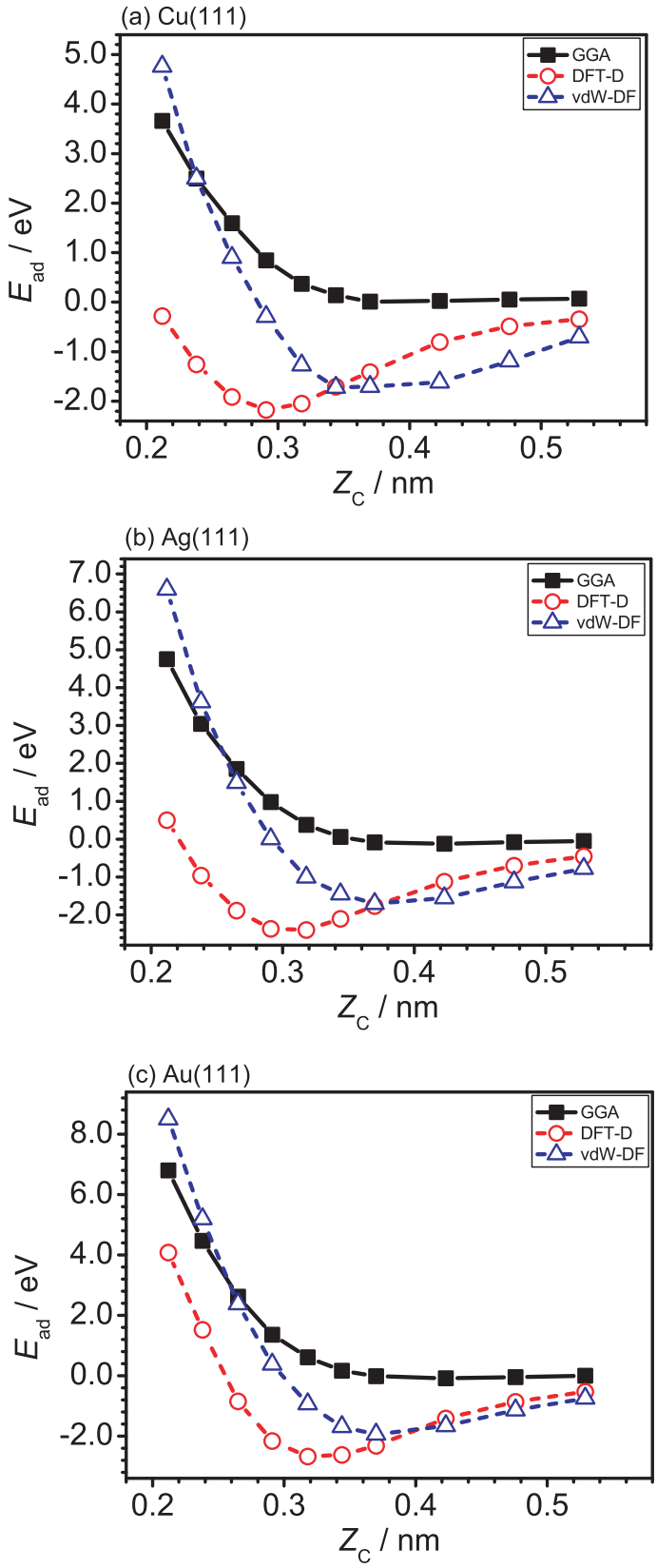

Figure 3.21: The adsorption energy (E_{ad}) as a function of the distance between the molecule and the metal surface (Z_{C}) using GGA, DFT-D, and vdW-DF for PFP on (a) Cu(111), (b) Ag(111), and (c) Au(111)

DF method gives reasonable adsorption energy, whereas the DFT-D and the GGA methods give slight overestimation and significant underestimation of the magnitude of it, respectively. Thus, we consider that $E_{\mathrm{ad}}^{\mathrm{vdW}}$'s are presumably most accurate adsorption energies of PFP adsorbed on the three metal surfaces, and these results might indicate the the interaction between PFP and close-packed noble metal surfaces is predominantly due to the dispersion interactions.

For Cu, the calculated $Z_{\mathrm{C}}^{\mathrm{DFT-D}}$ value is 0.29 nm, which is in excellent agreement with the experimental value of 0.298 nm [40]. On the contrary, the calculated $Z_{\mathrm{C}}^{\mathrm{vdW}}$ and $Z_{\mathrm{C}}^{\mathrm{GGA}}$ are 0.34 and 0.37 nm, respectively, being significantly overestimated by 0.04∼0.07 nm. For Ag and Au, the PFP-substrate distances have never been measured experimentally, and we cannot compare our calculated distances with the experimental one. However, as will be discussed later, by comparing the calculated vacuum level shifts with the experimental ones, we confirm the similar trend to the cases of benzene and pentacene. Thus, we conclude that for PFP/metal systems, the DFT-D method give reasonable PFP-metal distances.

3.3.3 Vacuum level shift and slope parameter

The vacuum level shift is calculated from the work function change ($\Delta\phi$), and $\Delta\phi$ is estimated [Eqs. (3.2) and (3.3)]. For Cu, $n_{\mathrm{Cu(111)}}$ is based on the experimental data of PFP on Cu(111) [40]. Because the surface molecular density on Ag(111) and Au(111) have been never measured experimentally, we assumed that $n_{\mathrm{Ag(111)}}$ and $n_{\mathrm{Au(111)}}$ are the same as $n_{\mathrm{Cu(111)}}$. In this way, the work function changes ($\Delta\phi$) are scaled from the bare calculated values ($\Delta\phi'$) by factors, 1.0, 1.25, and 1.3 for Cu, Ag, and Au substrate, respectively.

Figure 3.22 shows $\Delta\phi$ of PFP adsorbed on Cu(111), Ag(111), and Au(111) as a function of Z_{C} using GGA. The experimentally determined work function changes on Cu(111) [40] and Au(111) [106] are indicated by horizontal dashed lines, whereas the experimentally determined PFP-Cu(111) distance [Z_{C}(Cu)][40] and the equilibrium distances Ag(111) and Au(111) [$Z_{\mathrm{C}}^{\mathrm{DFT-D}}$(Ag) and $Z_{\mathrm{C}}^{\mathrm{DFT-D}}$(Au)] calculated by DFT-D are shown by vertical dotted lines.

Table 3.6 summarizes $\Delta\phi$'s calculated by GGA at several distances for PFP on Cu(111), Ag(111), and Au(111). For Cu and Au, the calculated $\Delta\phi$'s at $Z_{\mathrm{C}}^{\mathrm{DFT-D}}$ are in good agreement with the exper-

Table 3.6: The work function changes ($\Delta\phi$) calculated by GGA at $Z_{\mathrm{C}}^{\mathrm{GGA}}$, $Z_{\mathrm{C}}^{\mathrm{DFT-D}}$, and $Z_{\mathrm{C}}^{\mathrm{vdW}}$, along with the experimentally work function change ($\Delta\phi^{\mathrm{exp}}$) for PFP on Cu(111), Ag(111), and Au(111).

Surface	GGA		Expt.	
	Z_{C} / nm	$\Delta\phi$ / eV	$Z_{\mathrm{C}}^{\mathrm{exp}}$ / nm	$\Delta\phi^{\mathrm{exp}}$ /eV
Cu(111)	$Z_{\mathrm{C}}^{\mathrm{DFT-D}}$=0.29	-0.34	-0.298[a]	-0.35[a]
	$Z_{\mathrm{C}}^{\mathrm{vdW}}$=0.34	-0.26	—	—
	$Z_{\mathrm{C}}^{\mathrm{GGA}}$=0.37	-0.16	—	—
Ag(111)	$Z_{\mathrm{C}}^{\mathrm{DFT-D}}$=0.32	-0.21	—	—
	$Z_{\mathrm{C}}^{\mathrm{vdW}}$=0.37	-0.23	—	—
	$Z_{\mathrm{C}}^{\mathrm{GGA}}$=0.42	-0.01	—	—
Au(111)	$Z_{\mathrm{C}}^{\mathrm{DFT-D}}$=0.32	-0.50	—	-0.50[b]
	$Z_{\mathrm{C}}^{\mathrm{vdW}}$=0.37	-0.18	—	—
	$Z_{\mathrm{C}}^{\mathrm{GGA}}$=0.42	-0.06	—	—

[a] Ref. [40].
[b] Ref. [106].

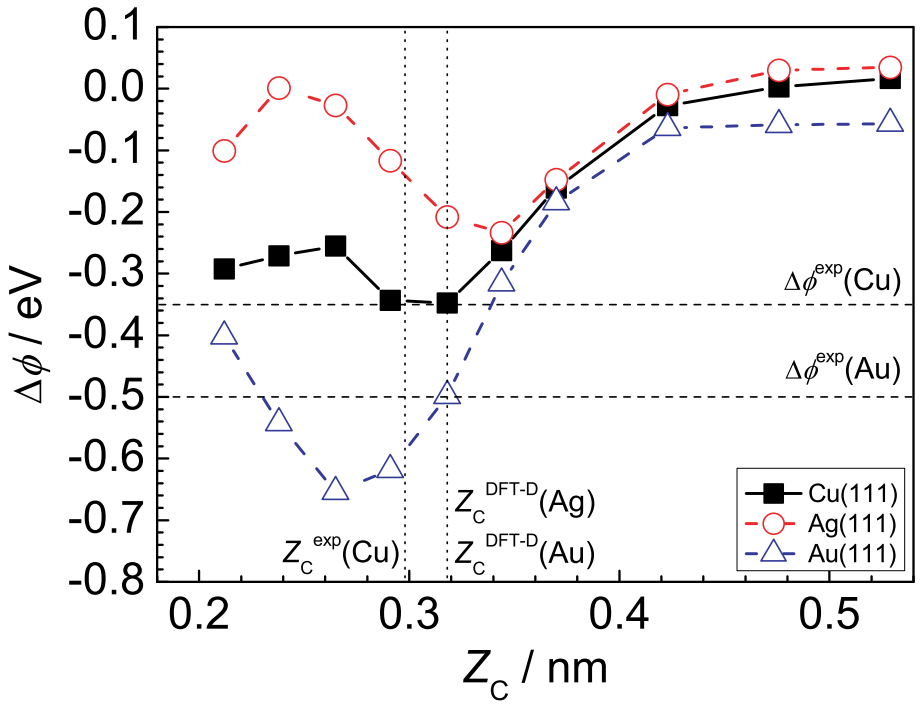

Figure 3.22: The work function change ($\Delta\phi$) as a function of Z_{C} for pentacene on Cu(111), Ag(111), and Au(111). The experimental values of $\Delta\phi$ on Cu(111) and Au(111) are shown by horizontal dashed lines. The experimentally observed PFP-Cu(111) distance ($Z_{\mathrm{C}}^{\mathrm{exp}}$(Cu), and the equilibrium distance on Ag(111), and Au(111) ($Z_{\mathrm{C}}^{\mathrm{DFT-D}}$(Ag) and $Z_{\mathrm{C}}^{\mathrm{DFT-D}}$(Au)) calculated by DFT-D are shown by vertical dotted lines.

imental values of -0.35 [40] and -0.50 eV [106], respectively. On the other hand, the absolute values of the calculated $\Delta\phi$'s at $Z_{\mathrm{C}}^{\mathrm{GGA}}$ and $Z_{\mathrm{C}}^{\mathrm{vdW}}$ are significantly underestimated, which comes from the overestimation of $Z_{\mathrm{C}}^{\mathrm{GGA}}$ and $Z_{\mathrm{C}}^{\mathrm{vdW}}$ values. Thus, our results indicate that the DFT-D method can predict the equilibrium distance and the work function changes of PFP/metal interfaces quite accurately, and thus for Ag, the equilibrium distance and the work function change are determined to be 0.32 nm and -0.21 eV, respectively.

As shown in Fig. 3.22, at $Z_{\mathrm{C}} \leq 0.34$ nm, $\Delta\phi$'s for the three metal surfaces take minima. The minima for the PFP/metal systems are deeper than those for the pentacene/metal systems. This is because the effect of the molecular distortion becomes more significant if the PFP molecule moves closer to the substrate, as described above. Thus, we calculated the average height of F atoms relative C-rings of PFP ($Z_{\mathrm{F-C}}$) and the work function changes which are caused by the molecular distortion ($\Delta\phi_{\mathrm{mol}}$) as a function of Z_{C} for PFP on Cu(111), Ag(111), and Au(111) (Fig. 3.23). Here, we estimated $\Delta\phi_{\mathrm{mol}}$ from the dipole of the isolated PFP molecule, given that the geometry of the isolated molecule is the same as that adsorbed on the substrate. For Cu, $Z_{\mathrm{F-C}}$ at $Z_{\mathrm{C}}^{\mathrm{exp}}$ is calculated to be $\sim$0.008 nm, which is

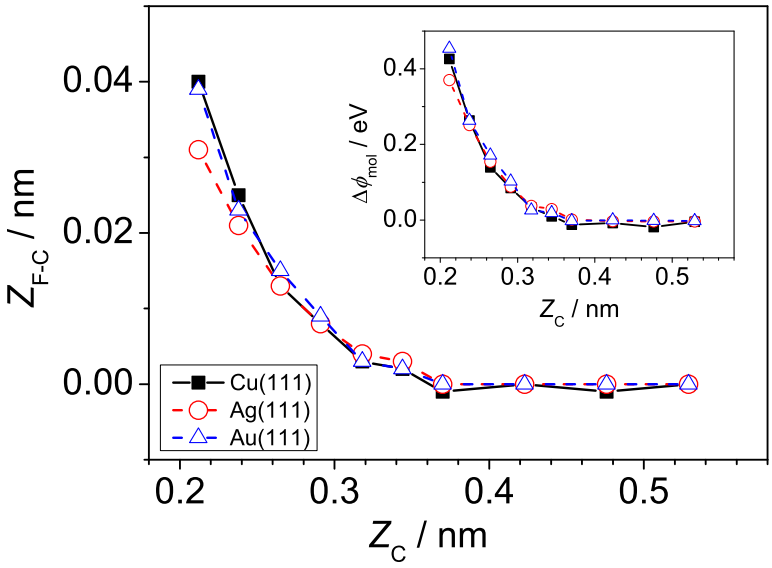

Figure 3.23: The average height of F atoms relative C-rings of PFP ($Z_{\mathrm{F-C}}$) as a function of Z_{C} for PFP on Cu(111), Ag(111), and Au(111). The work function changes which are caused by the molecular distortion ($\Delta\phi_{\mathrm{mol}}$) for PFP on the three metal surfaces are displayed in the inset.

good agreement with the experimental value of 0.01 nm [40]. Our calculations show that we can get the accurate molecular structure if we use the experimentally-observed molecule-substrate distance [121]. As seen in Fig. 3.23, the distortion of the PFP molecule starts at $Z_{\mathrm{C}} \leq 0.34$ nm, and for example, $\Delta\phi_{\mathrm{mol}}$ at $Z_{\mathrm{C}} = 0.21$ nm reaches ~0.4 eV. The dependences of $Z_{\mathrm{F-C}}$'s and $\Delta\phi_{\mathrm{mol}}$'s are almost the same for the three metal surfaces. However, for Cu, Ag, and Au, $\Delta\phi_{\mathrm{mol}}$'s at $Z_{\mathrm{C}}^{\mathrm{DFT-D}}$ are 0.08, 0.04, and 0.03 eV, respectively. This is because the difference in $\Delta\phi_{\mathrm{mol}}$ on different metal surfaces is attributed to the difference in the PFP-metal distance.

To single out the electronic factor contributing to the formation of interface dipoles from geometric factors, we subtract the effect of the intramolecular dipole ($\Delta\phi_{\mathrm{mol}}$) from the work function change ($\Delta\phi$) for PFP adsorbed on Cu(111), Ag(111), and Au(111). In Fig. 3.24(a), we plotted the results of ($\Delta\phi - \Delta\phi_{\mathrm{mol}}$) for the three metal surfaces. The difference behavior of ($\Delta\phi - \Delta\phi_{\mathrm{mol}}$) on the three metal surfaces purely comes from the difference in the electronic structure of the three adsorbed systems, because the same surface molecular densities on the three metal surfaces are assumed in these calculations. As seen in Fig. 3.24(a), ($\Delta\phi - \Delta\phi_{\mathrm{mol}}$)'s are almost independent on the metal work function. On the other hand, at $Z_{\mathrm{C}} \leq 0.34$ nm, ($\Delta\phi - \Delta\phi_{\mathrm{mol}}$)'s vary with the metal work function, and this comes from the hybridization

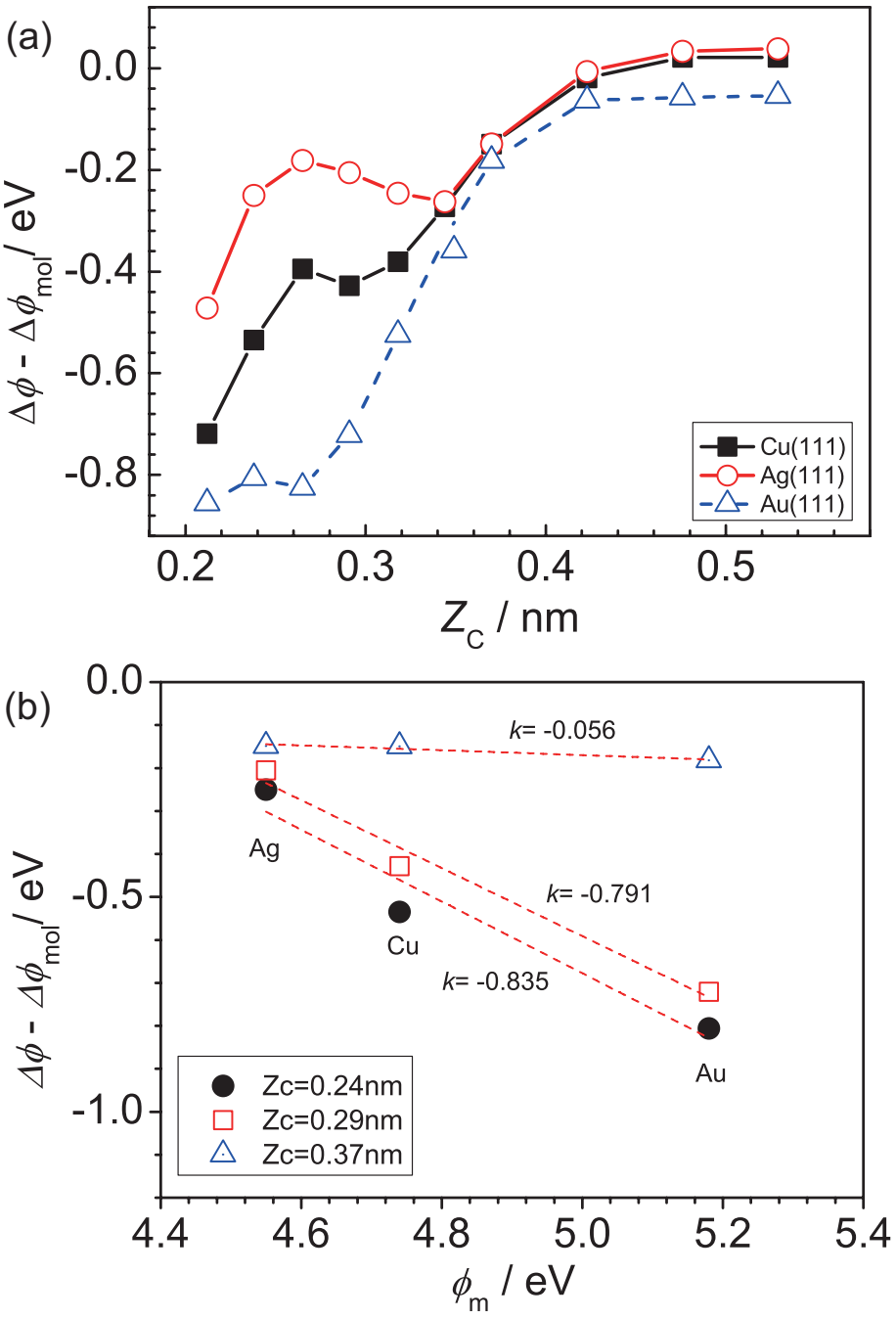

Figure 3.24: (a)($\Delta\phi - \Delta\phi_{\rm mol}$) as a function of $Z_{\rm C}$ for PFP on the three metal surfaces. (b)($\Delta\phi - \Delta\phi_{\rm mol}$) as a function of $\phi_{\rm m}$ for PFP on the three metal surfaces at $Z_{\rm C}$ =0.24, 0.29, and 0.37 nm.

between the PFP molecular orbital and the metal substrate states, as pointed by our previous calculation of the pentacene/metal systems. To make clear the relationship between ($\Delta\phi - \Delta\phi_{\rm mol}$) and the metal work function ($\phi_{\rm m}$), we plotted ($\Delta\phi - \Delta\phi_{\rm mol}$) as a function of $\phi_{\rm m}$ at several $Z_{\rm C}$ (0.24, 0.29, and 0.37 nm) in Fig. 3.24(b), where k is defined by $k \equiv {\rm d}(\Delta\phi - \Delta\phi_{\rm mol})/{\rm d}\phi_{\rm m}$. The slope parameter can be expressed by $S = 1 + k$ [Eq.(1.4)]. Although experimentally-observed S and k values include both geometric and electronic contributions, in the present analysis, we hypothetically estimate S and k values using the same geometries for the three metal surfaces. As in seen in Fig. 3.24(b), k at $Z_{\rm C}$ =0.24, 0.29, and 0.37 nm are evaluated to be -0.84, -0.79, and -0.056, respectively, indicating that as the PFP molecules approaches the substrate, the slope parameter, S, decreases from ∼0.95 to ∼0.16 [Eq. (1.4)]. This result suggests that the transition from the Schottky limit to the Bardeen limit, which is similar to that for pentacene adsorbed on noble metals. Note that in the Bardeen limit, the difference in ($\Delta\phi - \Delta\phi_{\rm mol}$) between on Ag and on Cu for the PFP/metal systems is larger than the difference in $\Delta\phi$ between on Ag and on Cu for the pentacene/metal systems. Moreover, the absolute values of ($\Delta\phi - \Delta\phi_{\rm mol}$)'s for the PFP/metal systems are smaller than those for the pentacene/metal systems, given that the adsorbate-metal distances and the surface molecular densities are the same for both systems. For example, at $Z_{\rm C}$ = 0.21 nm, ($\Delta\phi - \Delta\phi_{\rm mol}$) for the PFP/Au systems is -0.9 eV, whereas $\Delta\phi$ for the pentacene/Au system is rescaled to be -1.1 eV by assuming that the surface molecular density is the same as that for the PFP/metal system. These differences presumably come from the stronger chemically reactivity of PFP than pentacene, which means that the hybridization of PFP is stronger than that of pentacene if the geometric parameters are the same.

3.3.4 Electronic structure

To inspect the electronic structures of the adsorbed systems, we calculated the projected density of states (PDOS) onto the molecular orbitals of PFP. In Fig. 3.25, we display the PDOS of PFP molecular orbitals on Cu(111), Ag(111), and Au(111). Note that we included that the molecular orbitals upto LUMO as the PFP molecular orbitals. The contribution of LUMO+1 is much higher than LUMO by ∼1.3 eV, and therefore we did not include the LUMO+1 state.

On Cu and Au, the HOMO peaks are located at -0.74 and -0.46 eV (energy zero is set to $E_{\rm F}$), which

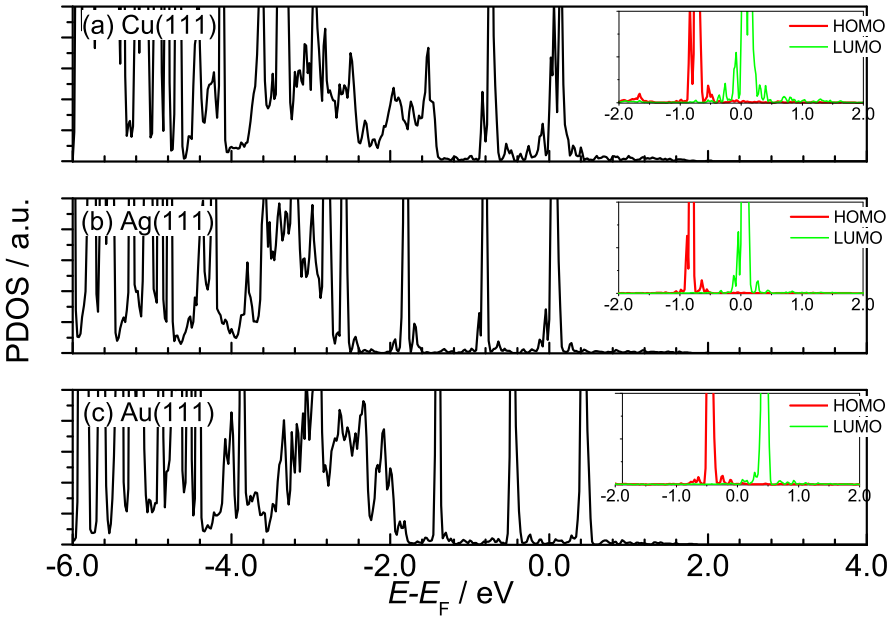

Figure 3.25: The density of states projected onto the molecular orbitals of PFP (PDOS) on (a) Cu(111), (b) Ag(111), and (c) Au(111). The energy zero is taken to be the Fermi energy of the adsorbed system. The HOMO and the LUMO parts of the PDOS near the Fermi energy are magnified in the insets

are slightly shallower than the experimentally-observed HOMO derived peaks at -1.35 [40] and -0.80 eV [106], respectively, because of the effect of the self-interaction in GGA. On Cu and Ag, the LUMO states become broaden and the part of the LUMO state is below the Fermi level. In particular, the result for Cu shows the hybridization is weaker than those for pentacene/Cu(100) [98] and pentacene/Cu(111) [40]. On Au, the LUMO and HOMO peaks are sharp, and the LUMO states are above the Fermi energy. which indicates that the molecular orbitals do not significantly hybridize with the substrate states.

We calculated the projected density of states (PDOS) onto atomic d orbital of the metal atom circled in Fig. 3.20 for a clean surface and for the adsorbed system. In Fig. 3.26, we show the d_{z^2}-component of PDOS of the metal atom. Note that we confirmed that in the PFP/Cu(111) system, the d_{z^2}-component dominates the hybridization compared with other components. We showed that for a pentacene/Cu(111) interface, a broadening of the d states due to the hybridization with pentacene states can be observed. On the other hand, for the PFP/noble metal systems, an obvious broadening of the d states is not observed, confirming that the interaction between PFP and the surface is weaker than that of pentacene with a Cu surface.

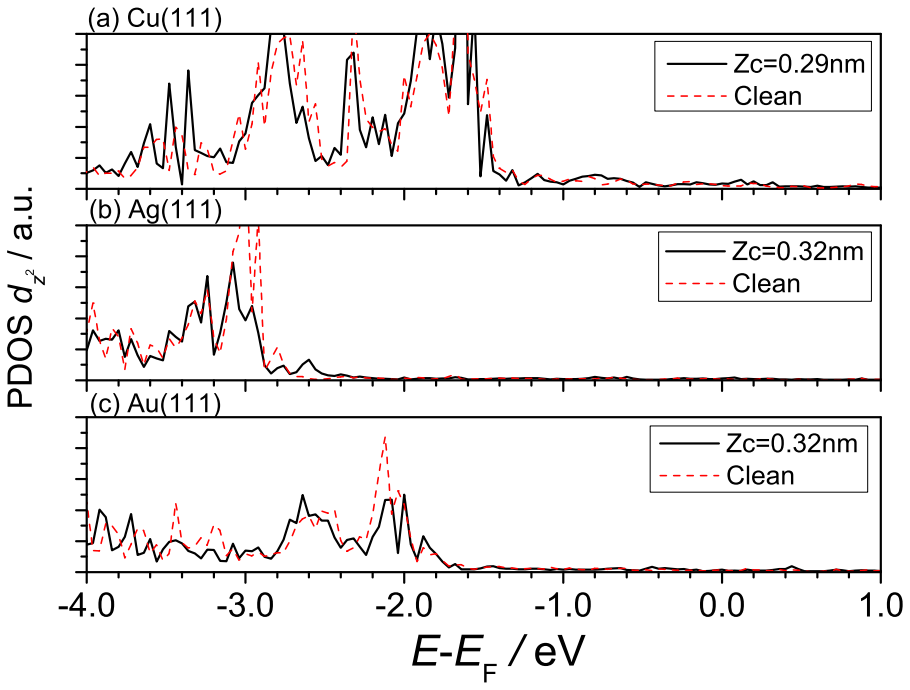

Figure 3.26: The d_{z^2}-component of the projected density of states (PDOS) of the metal atom circled in Fig. 3.20 for a clean surface (Clean) and for the adsorbed system (Z_C=Z_C^{cal}), for (a) Cu(111), (b) Ag(111), and (c) Au(111)

There results show that for Au a physical factor dominates the PFP-substrate interaction, whereas for Cu and Ag a chemical factor slightly contributes to the interaction the PFP LUMO and the substrate *d* states. The chemical interaction of PFP with the metal surfaces is weaker than that of pentacene with the metal surfaces, because of the larger PFP-substrate distances.

3.4 Control of organic/metal interface

3.4.1 Summary of adsorption distances

Table 3.7: The equilibrium distances calculated by DFT-D ($Z_{\mathrm{C}}^{\mathrm{DFT-D}}$) for benzene ($C_6H_6$), pentacene ($C_{22}H_{14}$), and PFP ($C_{22}F_{14}$) on Cu(111), Ag(111), and Au(111). $Z_{\mathrm{C}}^{\mathrm{DFT-D}}$ is in the unit of nm.

Surface	C_6H_6	$C_{22}H_{14}$	$C_{22}F_{14}$
Cu(111)	0.29	0.24	0.29
Ag(111)	0.29	0.29	0.32
Au(111)	0.31	0.32	0.32

Table 3.7 summarizes the equilibrium distances calculated by the DFT-D method ($Z_{\mathrm{C}}^{\mathrm{DFT-D}}$)for benzene, pentacene, and PFP adsorbed on Cu(111), Ag(111), and Au(111).

On Ag and Au, the distances for the adsorbed system are almost the same, reflecting that the Ag and Au surfaces are chemically inert. On the other hand, on Cu, the adsorption distances for different adsorbed systems are different. The distance for the pentacene/Cu interface is smaller than that for the benzene/Cu interface, reflecting that pentacene is more chemically reactive than benzene. In contrast, the distance for the PFP/Cu interface is larger than that for the pentacene/Cu interface, although PFP is more chemically reactive than pentacene. This is presumably because of the repulsion between $2p$ electrons of F atoms and electrons of substrate. Thus, these results indicate that functional group can control adsorption distance.

3.4.2 The effect of functional group on the adsorption distance

To confirm the control of the adsorption distance by functional group, we investigated how fluorination affects adsorption distance. We calculated several molecules (Fig. 3.27) adsorbed on Cu(111) to perform a geometry optimization without any restriction by using the DFT-D method. The threshold value of the maximum force is set to be 0.2 nN. These molecules have the same flamework which consists of five benzene rings, whereas the number of fluorine is different. The numbers of F atoms in F12, F8, and F4 are 12, 8, and 4, respectively. Table 3.8 summarizes the electron affinity (A) and the ionization

potential (I) of those molecules calculated by GGA. Here, we assumed that the surface unit cells for those molecules adsorbed on Cu(111) are the same as that of the PFP/Cu interface.

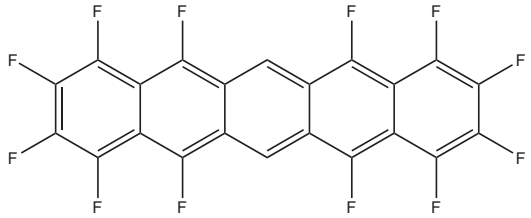

(a) F12

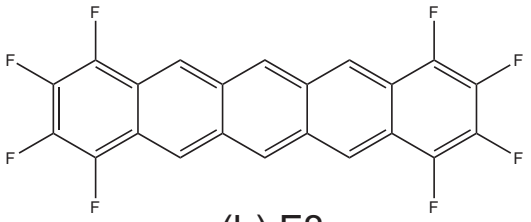

(b) F8

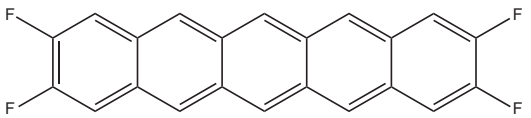

(c) F4

Figure 3.27: Molecular structures of (a) F12, (b) F8, and (c) F4

The work function changes for F12, F8, and F4 adsorbed systems are estimated to be -0.29, -0.41, and -0.62 eV, respectively. Figure 3.28 shows the relationship between the adsorption distance and fluorination. Note that we estimated the adsorption distance by averaging the height of C atoms from the first layer of the surface. As the number of F atoms increases, the adsorption distance increases, which confirms that the repulsion between $2p$ electrons of F atoms and electrons of substrate causes the distance larger. These results indicate that we can control the adsorption distance if we choose an appropriate functional group, and thus we can get a desired organic/metal interface.

Table 3.8: The electron affinity (A) and the ionization potential (I) of PFP, F12, F8, F4, and pentacene calculated by GGA

Molecule	A / eV	I / eV
$C_{22}F_{14}$	4.28	5.25
F12	4.30	5.27
F8	4.04	5.17
F4	3.72	4.90
$C_{22}H_{14}$	3.36	4.50

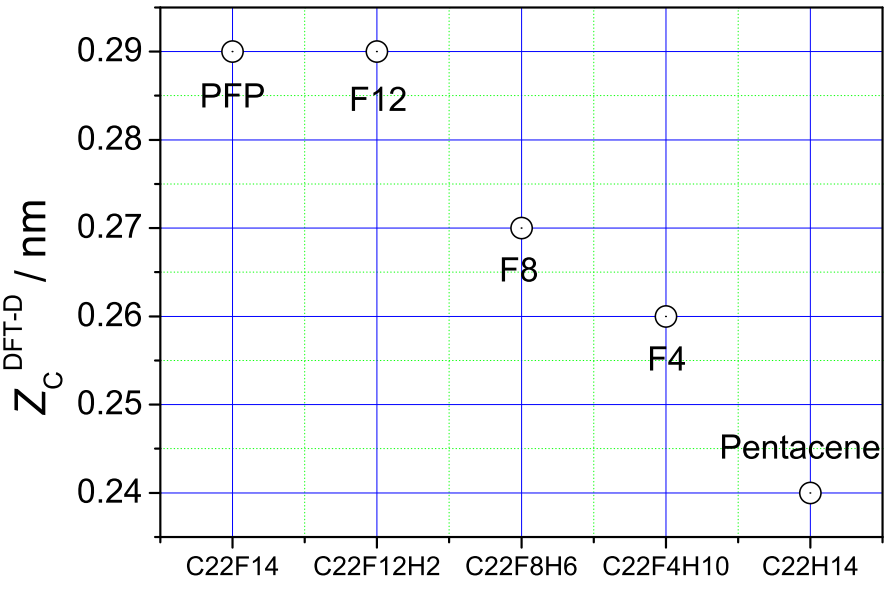

Figure 3.28: The relationship between the adsorption distance and fluorination.

3.5 Summary

We have presented a first-principles study of benzene, pentacene, and PFP adsorbed on Cu(111), Ag(111), and Au(111) to clarify the mechanism of the interface dipole.

The work function change ($\Delta\phi$) is sensitive to the molecule-substrate distance (Z_{C}). Furthermore, we investigate the dependence of the slope parameter on geometric factors such as molecular-substrate distance and surface molecular density. We compared $\Delta\phi$'s on the three metal surfaces provided that the molecule-substrate distances and the surface molecular densities are the same, and thus showed the geometric and electronic contribution to the interface dipole.

- In the case of benzene, $\Delta\phi$'s on the three metal surfaces are almost the same Thus, the interfaces are in the Schottky limit. This mean that the geometric factors mainly contribute the interface dipole.

- In the case of pentacene, at $Z_{\mathrm{C}} \geq 0.34$ nm, $\Delta\phi$'s on the three metal surfaces does not the substrate work function (ϕ_{m}). On the other hand, $Z_{\mathrm{C}} \leq 0.34$ nm, $\Delta\phi$'s vary with ϕ_{m}. This means a transition from the Schttky limit to the Bardeen limit. This means that not only the geometric factors but also the electronic factor contribute to the interface dipole.

- In the case of PFP, at $Z_{\mathrm{C}} \leq 0.34$ nm, the interface dipole induced by the molecular distortion ($\Delta\phi_{\mathrm{mol}}$) affects $\Delta\phi$. At $Z_{\mathrm{C}} \geq 0.34$ nm, the work function changes (($\Delta\phi - \Delta\phi_{\mathrm{mol}}$)'s) does not depend on ϕ_{m}. On the other hand, at $Z_{\mathrm{C}} \leq 0.34$ nm, ($\Delta\phi - \Delta\phi_{\mathrm{mol}}$)'s vary with ϕ_{m}. This means a transition from the Schottky limit to the Bardeen limit. This means that not only the geometric factors but also the electronic factor contribute to the interface dipole, which is similar to the case of pentacene.

We employed the semiempirical van der Waals (DFT-D) method and the van der Waals density functional (vdW-DF) method to include the long-range vdW interactions.

- The DFT-D method can reproduce the molecule-substrate distance accurately, although it could overestimate the adsorption energy.

- The vdW-DF method systematically overestimate the distance, although it can reproduce the adsorption energy.

The calculated work function changes at the distance calculated by DFT-D are in good agreement with the experimental values, which shows that the DFT-D method can predict the vacuum level shift of organic/metal interfaces accurately.

In particular, the pentacene/Cu interface is not simple physisorption. Our first-principles calculation reveals that the surface-band dispersion of pentacene adsorbed on a Cu surface is ascribed to the hybridization.

Furthermore, we investigate the effect of functional group on the adsorption distance. Our calculation results indicate that we can control the adsorption distance if we choose an appropriate functional group, and thus we can get a desired organic/metal interface.

Chapter 4

Prediction model for interface dipole

In the preceding chapter, we showed that first-principles calculations can predict the vacuum level shift of organic/metal interfaces accurately. However, the calculation cost is rather high, and thus prediction model for the interface dipole is desired. As described in Introduction, the induced density interface states (IDIS) model has been proposed as a model for the interface dipole. We examine the IDIS model using first-principle calculations, and investigate factors determining the interface dipole from the viewpoint of chemical trend.

4.1 Induced density of interface states (IDIS) model

For weak interaction organic/metal interfaces, Flores and co-workers proposed a simple model based on the induced density of interface states (IDIS) [42, 43, 44, 45, 46, 47, 48, 49]. In this model, they assumed that the interface dipole is originated mainly from the charge transfer between organic molecules and metal surfaces. Although the model is quite simple, they concluded that it provides a predictive description of the energy level at various organic/metal interfaces. However, it is not clear why the model works well and what the limitations of the model are.

In this study, we have theoretically examined the IDIS model for benzene, pentacene, and PFP adsorbed on Cu(111), Ag(111), and Au(111) using first-principles calculations.

4.1.1 Calculation method

The IDIS model provides a simple and intuitive explanation of energy-level alignment at weakly interacting organic/metal [42, 43, 45, 46, 47, 48, 49] and organic/organic [44, 45] interfaces. In the case of weakly interacting organic/metal interfaces and the metal creates an IDIS in the organic energy gap. Although the chemical interaction is weak, the IDIS is large enough to define the charge neutrality level (CNL) of the adsorbed organic molecule, E_{CNL}, Fig. 4.1 shows energy band diagrams at organic/metal interfaces before and after contact.

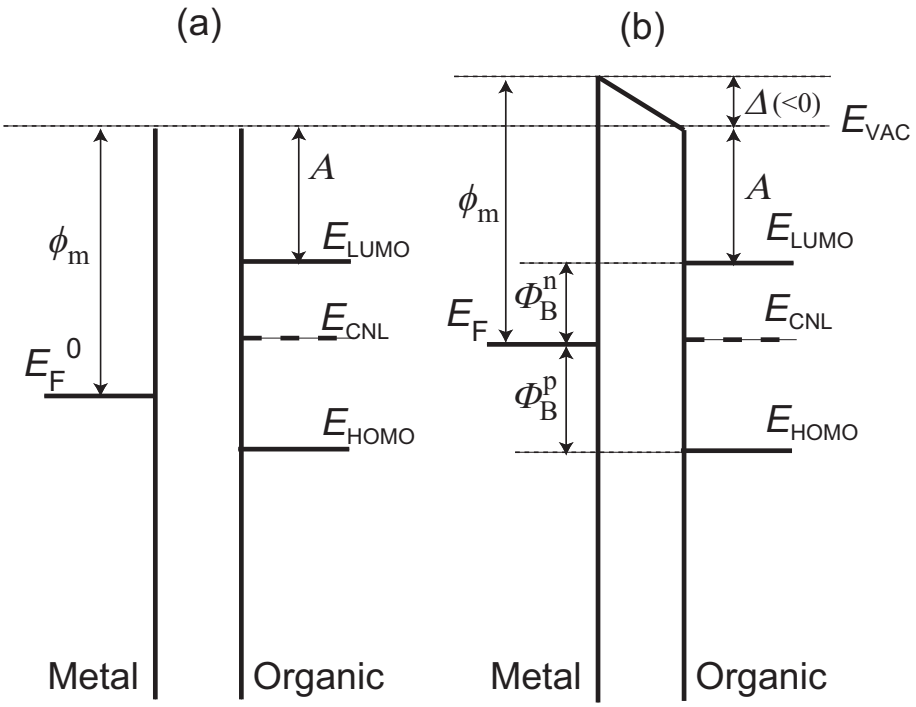

Figure 4.1: Energy band diagrams at organic/metal interfaces (a) before and (b) after contact. The sign of $\Delta\phi$ is taken to be minus in the case of the figure.

The barrier height of the electron injection ($\Phi_{\mathrm{B}}^{\mathrm{n}}$) and E_{CNL} have the following relation [37]:

$$\Phi_{\mathrm{B}}^{\mathrm{n}} = S(\phi_{\mathrm{m}} - A) + (1 - S)(E_{\mathrm{LUMO}} - E_{\mathrm{CNL}}), \tag{4.1}$$

where E_{LUMO} and A is the LUMO level and the electron affinity of the organic molecule, respectively, ϕ_{m} is the work function of a clean metal surface, and S is the interface slope parameter. The interface Fermi level, E_{F} (Fig. 4.1 (b)) and the initial metal Fermi level before contact, E_{F}^{0} (Fig. 4.1 (a)) are

described in the following ways:

$$E_{\mathrm{F}} = E_{\mathrm{LUMO}} - \Phi_{\mathrm{B}}^{\mathrm{n}}, \tag{4.2}$$

$$E_{\mathrm{F}}^{0} = E_{\mathrm{LUMO}} - \phi_{\mathrm{m}} + A, \tag{4.3}$$

where the built-in potential can be neglected because the dopant concentration in the organic region is very low. Inserting Eqs. (4.2), (4.3) into Eq. (4.1) finally gives the following relation:

$$E_{\mathrm{F}} - E_{\mathrm{CNL}} = S(E_{\mathrm{F}}^{0} - E_{\mathrm{CNL}}). \tag{4.4}$$

The charge transfer through the interface associated with the difference between E_{F} and E_{CNL}, and makes an interface dipole layer at the interface. The interface dipole layer induces a vacuum level shift, Δ (Fig. 4.1 (b)). From Eqs. (4.2)-(4.4), Δ is given by

$$\Delta = (1 - S)(E_{\mathrm{F}}^{0} - E_{\mathrm{CNL}}). \tag{4.5}$$

If the interaction between the organic molecules and the metal is large, that it to say, the slope parameter S is small, it tends to pin E_{F} close to E_{CNL} and Δ becomes close to $(E_{\mathrm{F}}^{0} - E_{\mathrm{CNL}})$ [42, 43].

To calculate the number of electron transfer from the molecule to the metal surface, which is necessary to estimate the vacuum level shift based on the IDIS model (Δ_{IDIS}), we carried out the Mulliken population analysis [119, 120]. Wave functions of a molecule-adsorbed metal (111) surface (ψ_i) were expanded by those of the separated molecule (χ_m^{A}) and the metal substrate (χ_n^{S}),

$$\psi_i = \sum_{m}^{M_{\mathrm{A}}} c_{im}^{\mathrm{A}} \chi_m^{\mathrm{A}} + \sum_{n}^{M_{\mathrm{S}}} c_{in}^{\mathrm{S}} \chi_n^{\mathrm{S}}, \tag{4.6}$$

where M_{A}, M_{S} are the numbers of the molecular and substrate orbitals employed to expand the wave function ψ_i, respectively. χ_m^{A} and χ_n^{S} are calculated by using the same **k**-point set, the same cutoff energies, and the same unit cell and exactly the same atomic positions as the adsorbed states. The expansion coefficients c_{im}^{A} and c_{in}^{S} are obtained by inverting the overlap matrix $S_{mn} = \langle \chi_m^{\mathrm{A}} | \hat{S} | \chi_n^{\mathrm{S}} \rangle$, where $\hat{S}$ is the overlap operation in the ultrasoft pseudopotential scheme [66]. The energy-dependent gross

population (GPOP, $q_m^{\mathrm{A}}(E)$) of a molecular orbital χ_m^{A} is defined by

$$q_m^{\mathrm{A}}(E) = \sum_{i=1}^{M} \left(|c_{im}^{\mathrm{A}}|^2 + \frac{1}{2} \left(\sum_{n=1}^{M} (c_{im}^{\mathrm{A}})^* c_{in}^{\mathrm{S}} S_{mn} + \mathrm{c.c.} \right) \right) \delta(E - E_i), \tag{4.7}$$

where E_i and M are the energy eigen value and the number of states of the adsorbed system, respectively. Here, it should be noted that the calculation of the overlap matrix must be carried out with great care. When we calculate the overlap matrix within the ultrasoft pseudopotential scheme, the overlap operator for the adsorbed system is used instead of using those for the separated systems. In some cases, this procedure causes an incorrect expansion of the wave functions of the total system (or the expansion coefficients), and hence violation of the orthonormal condition, leading to physically incorrect results. In such cases, the norm-conserving pseudopotentials or the all-electron method should be used instead. We verified that it is not the case in the present study by comparing the numbers of transferred electrons and the work function changes calculated with the ultrasoft and norm-conserving pseudopotentials in the last part of 4.1.2. We also note that the number of orbitals of the subsystem must be chosen carefully to avoid the incomplete basis problem.

The number of valence electrons (q_m^{A}) accommodated in the molecular orbital χ_m^{A} is calculated by

$$q_m^{\mathrm{A}} = \int_{-\infty}^{E_{\mathrm{F}}} q_m^{\mathrm{A}}(E). \tag{4.8}$$

The charge neutrality level of the adsorbate (E_{CNL}) is determined in such a way as to satisfy the following conditions:

$$q^{\mathrm{A}}(E) = \sum_{m=1}^{M_{\mathrm{A}}} q_m^{\mathrm{A}}(E), \tag{4.9}$$

$$\int_{\infty}^{E_{\mathrm{CNL}}} q^{\mathrm{A}}(E) dE = N_0^{\mathrm{A}}, \tag{4.10}$$

where N_0^{A} is the number of valence electrons belonging to the isolated neutral molecule. The number of electrons transferred to the molecule (ΔN^{A}) is calculated by integrating GPOP from E_{F} to E_{CNL}:

$$\Delta N^{\mathrm{A}} = \int_{E_{\mathrm{CNL}}}^{E_{\mathrm{F}}} q^{\mathrm{A}}(E) dE. \tag{4.11}$$

The vacuum level shift can thus estimated by applying Gauss's law to the surface charge on the metal and adsorbates [37],

$$\Delta_{\mathrm{IDIS}} = Z_{\mathrm{C}} \frac{\Delta N^{\mathrm{A}}}{A_0 \epsilon_i}, \tag{4.12}$$

where A_0 is the area of the surface unit cell of the adsorbed systems and ϵ_i is the permittivity of the interfacial layer, which is assumed to be close to that in vacuum, ϵ_0.

4.1.2 Calculation of the charge transfer and examination of the IDIS model

We will show the number of electrons transferred from the metal surfaces to adsorbed molecule (ΔN^{A}) as a function of Z_{C} for Cu(111), Ag(111), and Au(111). We compare the vacuum level shift estimated by the IDIS model (Δ_{IDIS}, Eq.(4.12)) with the work function change by using the self-consistent GGA results ($\Delta\phi$, Eq. (3.2)). Both Δ_{IDIS} and $\Delta\phi$ are corrected by the use of Eq. (3.3).

benzene-adsorbed noble metal systems

In Figs. 4.2-4.4, we show ΔN^{A} and the vacuum level shifts (Δ_{IDIS} and $\Delta\phi$) as a function of Z_{C} for benzene on Cu(111), Ag(111), and Au(111).

For the three surfaces, ΔN^{A}'s have minima. At large Z_{C}, holes are induced in the occupied states. As the molecule approaches, the unoccupied states are partially filled as shown in the inset of Fig. 3.5. Accordingly, Δ_{IDIS} fairly agrees with $\Delta\phi$ at large Z_{C}. In contrast, Δ_{IDIS} tends to deviate at small Z_{C}, where back donation from the substrate to the adsorbate become large (Figs. 4.2(b)-4.4(b)). This is similar to the result of benzene/Al(111) [64].

As shown in Figs. 4.2-4.4, the IDIS model works well, because the effect of the back donation is not significant.

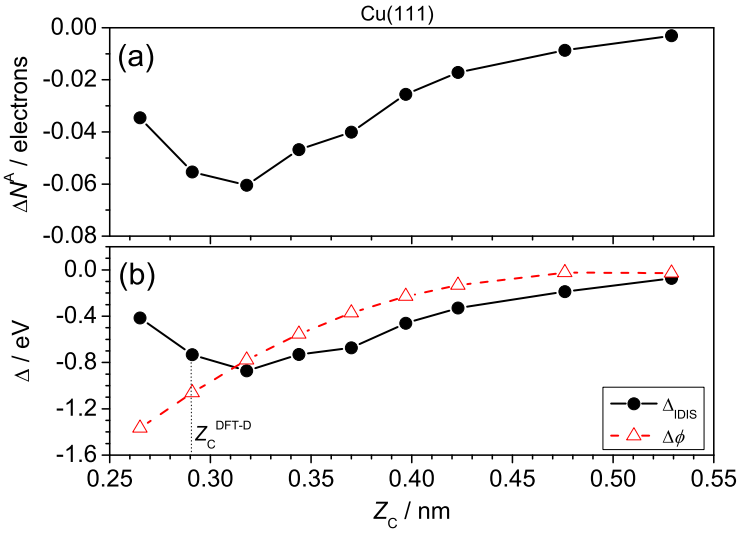

Figure 4.2: (a) Number of electrons transferred from the substrate to the adsorbate (ΔN^{A}) as a function of Z_{C} for benzene on Cu(111). (b) Vacuum level shifts estimated by the IDIS model (Δ_{IDIS}) and the work function change ($\Delta\phi$) as a function of Z_{C}, and the position of $Z_{\mathrm{C}}^{\mathrm{DFT-D}}$ is shown by a vertical dotted line.

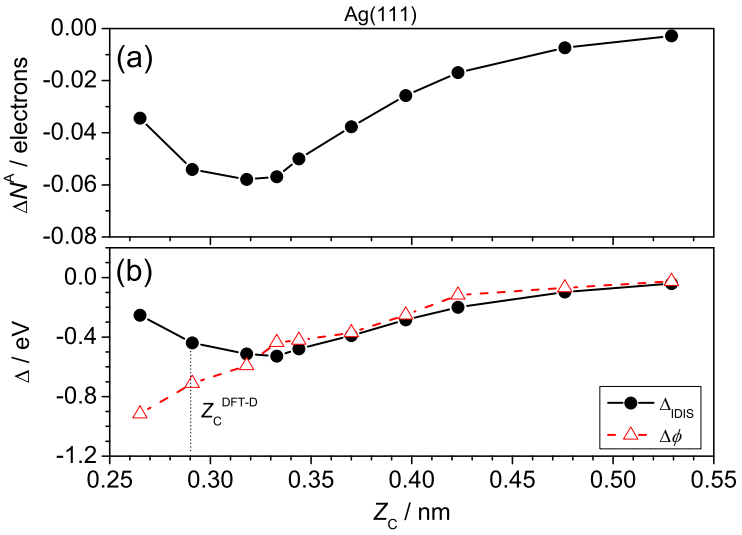

Figure 4.3: (a) Number of electrons transferred from the substrate to the adsorbate (ΔN^{A}) as a function of Z_{C} for benzene on Ag(111). (b) Vacuum level shifts estimated by the IDIS model (Δ_{IDIS}) and the work function change ($\Delta\phi$) as a function of Z_{C}, and the position of $Z_{\mathrm{C}}^{\mathrm{DFT-D}}$ is shown by a vertical dotted line.

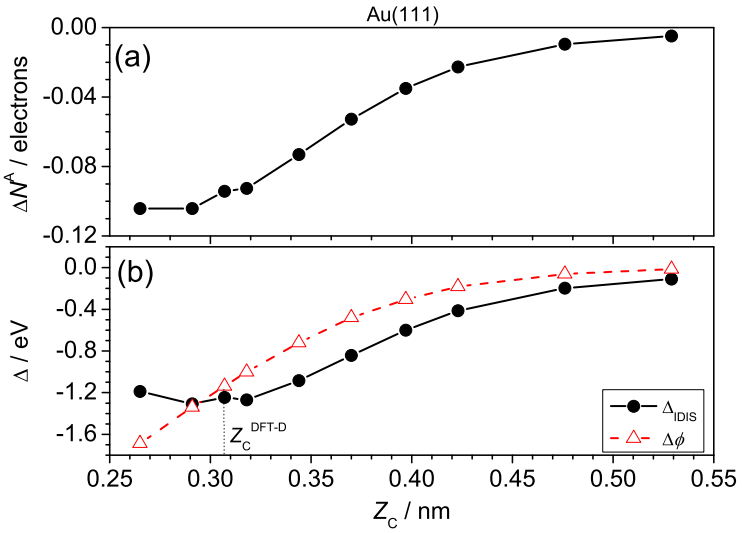

Figure 4.4: (a) Number of electrons transferred from the substrate to the adsorbate (ΔN^{A}) as a function of Z_{C} for benzene on Au(111). (b) Vacuum level shifts estimated by the IDIS model (Δ_{IDIS}) and the work function change ($\Delta\phi$) as a function of Z_{C}, and the position of $Z_{\mathrm{C}}^{\mathrm{DFT-D}}$ is shown by a vertical dotted line.

pentacene-adsorbed noble metal systems

In Figs. 4.5-4.7, we show ΔN^{A} and the vacuum level shifts (Δ_{IDIS} and $\Delta\phi$) as a function of Z_{C} for pentacene on Cu(111), Ag(111), and Au(111).

For the three surfaces, ΔN^{A}'s have minima as for the case of benzene. At large Z_{C}, holes are induced in the occupied states. As the molecule approaches, the unoccupied states are partially filled as shown in the inset of Fig. 3.11. Accordingly, Δ_{IDIS} fairly agrees with $\Delta\phi$ at large Z_{C}. In contrast, Δ_{IDIS} tends to deviate at small Z_{C}, where back donation from the substrate to the adsorbate become large (Figs. 4.5(b)-4.7(b)). This is also similar to the results of benzene.

For Ag and Au, as shown in Figs. 4.6-4.7, the IDIS model works well, because at $Z_{\mathrm{C}}^{\mathrm{DFT-D}}$ the effect of the back donation is not significant. On the other hand, for Cu, the IDIS model does not work well (Fig. 4.5), because at $Z_{\mathrm{C}}^{\mathrm{DFT-D}}$ the effect is significant.

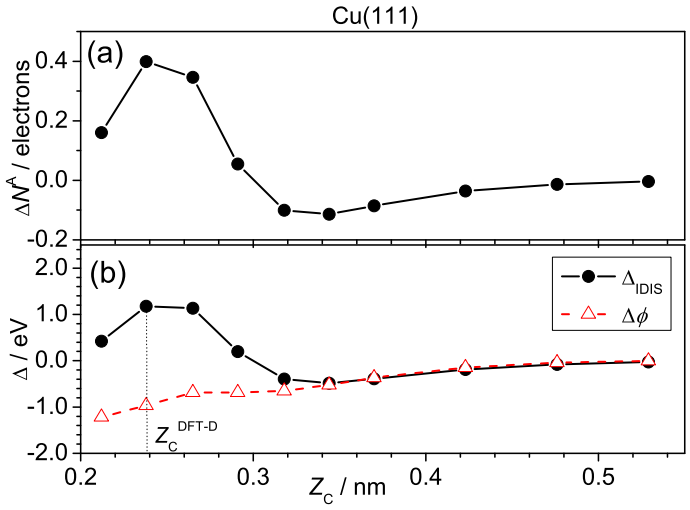

Figure 4.5: (a) Number of electrons transferred from the substrate to the adsorbate (ΔN^{A}) as a function of Z_{C} for pentacene on Cu(111). (b) Vacuum level shifts estimated by the IDIS model (Δ_{IDIS}) and the work function change ($\Delta\phi$) as a function of Z_{C}, and the position of $Z_{\mathrm{C}}^{\mathrm{DFT-D}}$ is shown by a vertical dotted line.

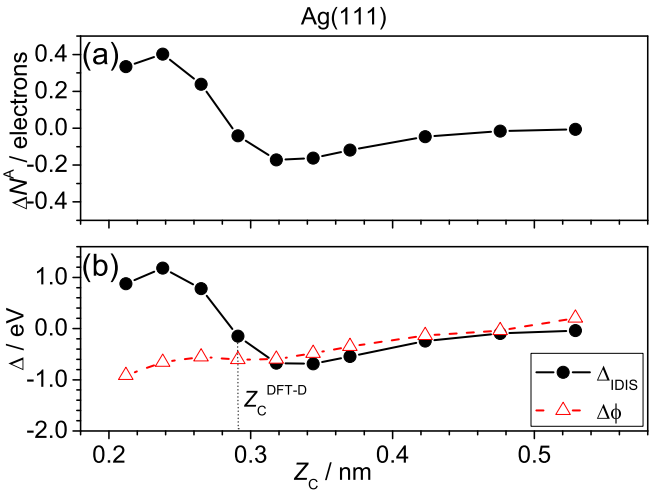

Figure 4.6: (a) Number of electrons transferred from the substrate to the adsorbate (ΔN^{A}) as a function of Z_{C} for pentacene on Ag(111). (b) Vacuum level shifts estimated by the IDIS model (Δ_{IDIS}) and the work function change ($\Delta\phi$) as a function of Z_{C}, and the position of $Z_{\mathrm{C}}^{\mathrm{DFT-D}}$ is shown by a vertical dotted line.

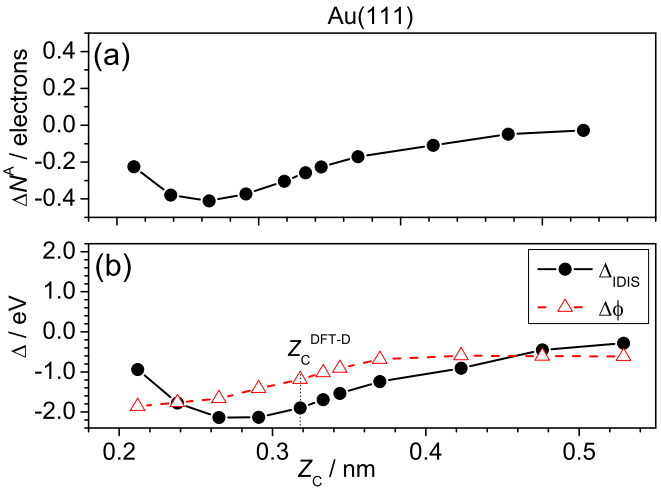

Figure 4.7: (a) Number of electrons transferred from the substrate to the adsorbate (ΔN^{A}) as a function of Z_{C} for pentacene on Au(111). (b) Vacuum level shifts estimated by the IDIS model (Δ_{IDIS}) and the work function change ($\Delta\phi$) as a function of Z_{C}, and the position of $Z_{\mathrm{C}}^{\mathrm{DFT-D}}$ is shown by a vertical dotted line.

PFP-adsorbed noble metal systems

In Figs. 4.8-4.10, we show ΔN^{A} and the vacuum level shifts (Δ_{IDIS} and $\Delta\phi$) as a function of Z_{C} for PFP on Cu(111), Ag(111), and Au(111).

For the three surfaces, ΔN^{A}'s have minima as for the case of benzene and pentacene. At large Z_{C}, holes are induced in the occupied states. As the molecule approaches, the unoccupied states are partially filled as shown in the inset of Fig. 3.25. Accordingly, Δ_{IDIS} fairly agrees with $\Delta\phi$ at large Z_{C}. In contrast, Δ_{IDIS} tends to deviate at small Z_{C}, where back donation from the substrate to the adsorbate become large (Figs. 4.8(b)-4.10(b)). This is also similar to the results of benzene and pentacene.

For Au, the IDIS model works well, because the effect of the back donation at $Z_{\mathrm{C}}^{\mathrm{DFT-D}}$ is not significant (Fig. 4.10). On the other hand, for Cu and Ag, the IDIS model does not work well (Fig. 4.8-4.9), because the effect at $Z_{\mathrm{C}}^{\mathrm{DFT-D}}$ is significant.

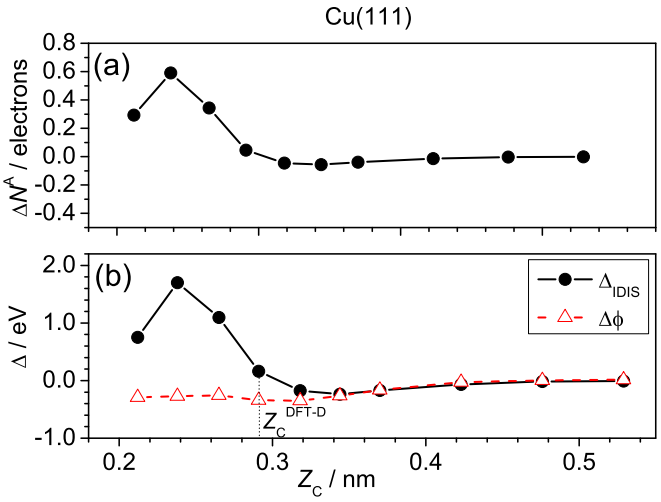

Figure 4.8: (a) Number of electrons transferred from the substrate to the adsorbate (ΔN^{A}) as a function of Z_{C} for PFP on Cu(111). (b) Vacuum level shifts estimated by the IDIS model (Δ_{IDIS}) and the work function change ($\Delta\phi$) as a function of Z_{C}, and the position of $Z_{\mathrm{C}}^{\mathrm{DFT-D}}$ is shown by a vertical dotted line.

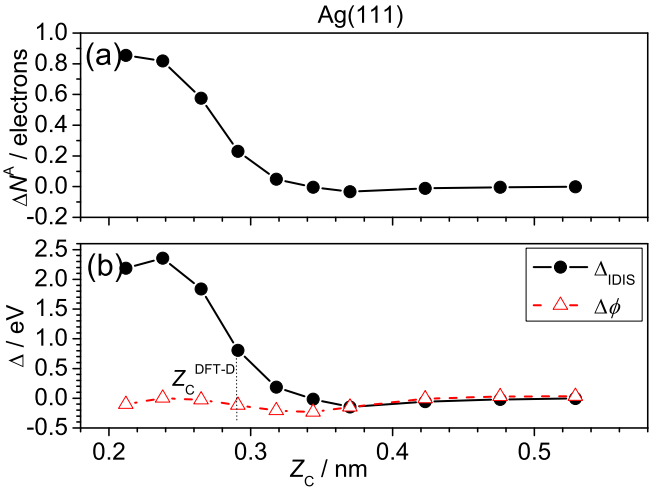

Figure 4.9: (a) Number of electrons transferred from the substrate to the adsorbate (ΔN^{A}) as a function of Z_{C} for PFP on Ag(111). (b) Vacuum level shifts estimated by the IDIS model (Δ_{IDIS}) and the work function change ($\Delta\phi$) as a function of Z_{C}, and the position of $Z_{\mathrm{C}}^{\mathrm{DFT-D}}$ is shown by a vertical dotted line.

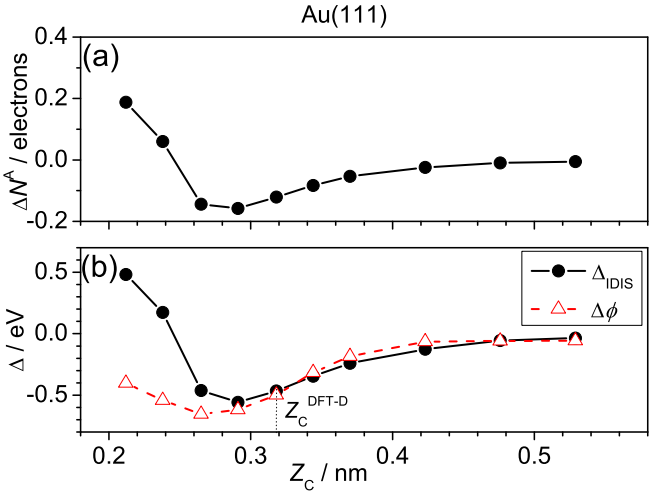

Figure 4.10: (a) Number of electrons transferred from the substrate to the adsorbate (ΔN^{A}) as a function of Z_{C} for PFP on Au(111). (b) Vacuum level shifts estimated by the IDIS model (Δ_{IDIS}) and the work function change ($\Delta\phi$) as a function of Z_{C}, and the position of $Z_{\mathrm{C}}^{\mathrm{DFT-D}}$ is shown by a vertical dotted line.

Summary of the examination of the IDIS model

Table 4.1 summarizes the vacuum level shifts estimated by the IDIS model (Δ_{IDIS}) and the work function change ($\Delta\phi$) for benzene, pentacene, and PFP on Cu(111), Ag(111), and Au(111).

Table 4.1: The vacuum level shifts estimated by the IDIS model (Δ_{IDIS}) and the work function change ($\Delta\phi$) for benzene, pentacene, and PFP on Cu(111), Ag(111), and Au(111).

Surface	C_6H_6		$C_{22}H_{14}$		$C_{22}F_{14}$	
	$\Delta\phi$ / eV	Δ_{IDIS} / eV	$\Delta\phi$ / eV	Δ_{IDIS} / eV	$\Delta\phi$ / eV	Δ_{IDIS} / eV
Cu(111)	-1.09	-0.73	-0.97	1.17	-0.34	0.16
Ag(111)	-0.71	-0.44	-0.61	-0.15	-0.21	0.18
Au(111)	-1.06	-1.25	-1.19	-1.9	-0.50	-1.9

As the molecule approaches, ΔN^{A} decreases. When the hybridization between molecular orbitals and substrate states causes back donation from the substrate to the molecule, ΔN^{A} sets in increasing drastically. Thus, the difference between $\Delta\phi$ and Δ_{IDIS} becomes large, if the effect of the back donation is significant. This results show Δ_{IDIS} is sensitive to the molecule-substrate distance, as pointed by Abad *et al.* [49]. That is to say, the IDIS model does not work well if the chemical interaction between the molecule and the substrate is strong, as for pentacene/Cu(111), PFP/Cu(111), and PFP/Ag(111) interfaces. On the other hand, the IDIS model work well if the chemical interaction is weak, as for the other interfaces. In such interfaces, the effect of the Pauli repulsion dominates, as pointed by Bagus *et al.* [77, 78, 79]. However, the present IDIS model neglects the effect of the Pauli repulsion. At present, the reason why the present IDIS model work reasonably well for such interfaces is not clear and needs to be further investigated.

The effect of the overlap integral on the calculation of the number of transferred electrons

We examined the effect of the different treatments of the overlap integral (S_{mn}) on the calculations of the numbers of transferred electrons (ΔN^{A}, Eq. (4.11)) of benzene on Cu(111), i.e. the ultrasoft pseudopotential (USPP) and the norm-conserving pseudopotential (NCPP) schemes. Figure 4.11 shows ΔN^{A} as a function of benzene-Cu(111) distance (Z_{C}) using the USPP and NCPP schemes. We also show the vacuum level shift estimated by the IDIS model (Δ_{IDIS}, Eq. (4.12)) and the work function change by using the self-consistent GGA results ($\Delta\phi$, Eq.(3.2)) in the two schemes. Both Δ_{IDIS}'s and $\Delta\phi$'s were corrected by the use of Eq. (3.3). As seen in Fig. 4.11 (a), the difference in ΔN^{A}'s between the two schemes is < 0.015 electrons at $Z_{\mathrm{C}} > 0.34$ nm, whereas it becomes larger at $Z_{\mathrm{C}} < 0.34$ nm. The difference in ΔN^{A}'s induces the difference in Δ_{IDIS}'s between the two schemes (Fig. 4.11). It should be noted that self-consistently calculated $\Delta\phi$'s are almost the same with the two schemes. The difference in ΔN^{A}'s and Δ_{IDIS}'s are mainly ascribed to the error in ΔN^{A} calculated by the USPP scheme, because in the USPP scheme, the normalization condition for wave functions of the separated benzene molecule (χ^{A}_m) and the metal substrate (χ^{S}_n) is satisfied if they separated but it is gradually violated as the adsorbate approaches the substrate. However, the qualitative features of ΔN^{A} and Δ_{IDIS} as a function of Z_{C} obtained by using USPP is similar to those by using NCPP, and thus the conclusion is unchanged when the USPP scheme is employed. We note that USPP should be used to calculate such a large system, because the USPP scheme has advantages over the NCPP scheme in the convergence of the self-consistent field (SCF) cycle and in the calculation time as shown in Table 4.2.

Table 4.2: Cutoff energies, average CPU time, and average number of SCF iterations by using the USPP and NCPP schemes.

Scheme	Cutoff energy / Ry		CPU time / hours	Number of SCF iterations
	Wave function	Charge density		
USPP	25	225	2.6	50
NCPP	64	256	10.6	81

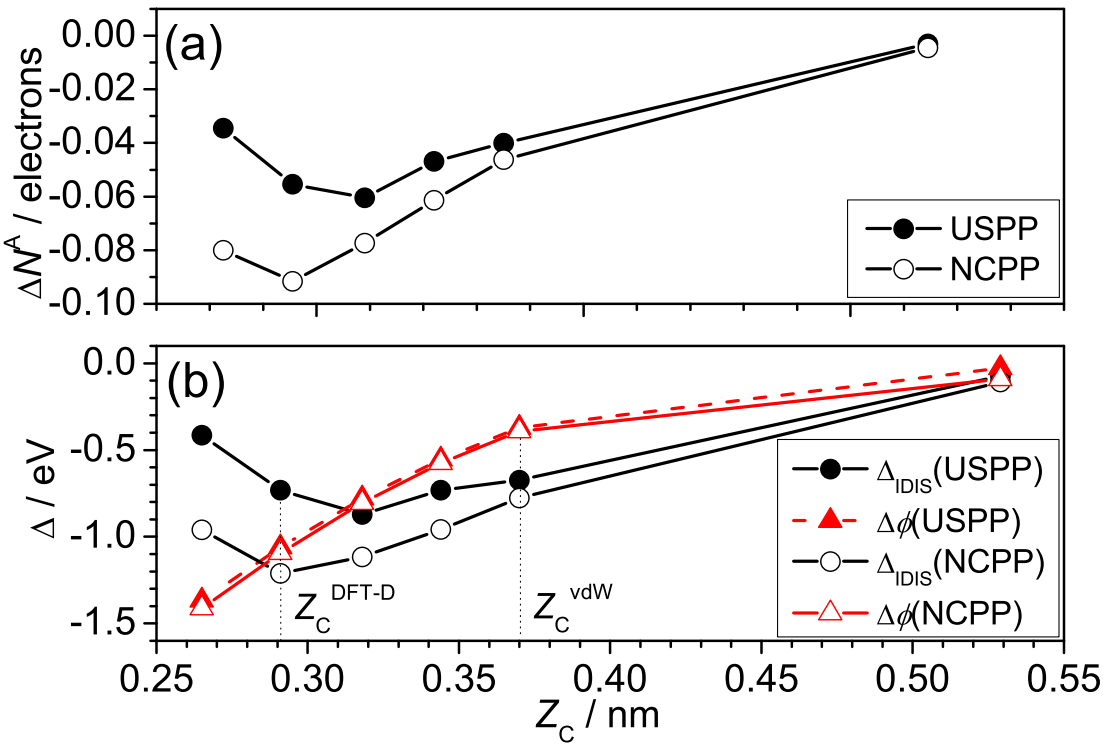

Figure 4.11: (a) Number of electrons transferred from the substrate to the adsorbate (ΔN^{A}) as a function of Z_{C} using the USPP and NCPP schemes for benzene on Cu(111). (b) Vacuum level shifts estimated by the IDIS model (Δ_{IDIS}) and the work function change ($\Delta\phi$) as a function of Z_{C}, in the USPP and NCPP schemes. The position of $Z_{\mathrm{C}}^{\mathrm{DFT-D}}$ is shown by a vertical dotted line.

4.2 Chemical trend of interface dipole

In the preceding section, we showed the limitation of the IDIS model. In this section, we investigate factors determining the interface dipole from the viewpoint of chemical trend.

4.2.1 Electron affinity

In the preceding chapter, the decrease in the slope parameter at small distance can infer that the chemical factor contributes to the molecule-substrate interaction. The calculated electronic structures show that the adsorbate LUMO and the substrate d states are important for the molecule-substrate interaction. We therefore focus on the back donation from substrate to the adsorbate LUMO, which the IDIS model neglects. Here, we employ the electron affinity of the adsorbate (A) to analyze the chemical trend on the same substrate.

To investigate the effect of A on the adsorbate-substrate distance and the interface dipole, in next session we will show $Z_{\mathrm{C}}^{\mathrm{DFT-D}}$ and $\Delta\phi$ as a function of A. A's of the adsorbate are calculated by GGA, and are summarized in Table 4.3.

Table 4.3: The electron affinity of the adsorbate (A) calculated by GGA

Adsorbate	A / eV
C_6H_6	1.24
$C_{22}H_{14}$	3.36
$C_{22}F_{14}$	4.28
PTCDA	4.82

Adsorption distance

To investigate the adsorbate dependence of $Z_{\mathrm{C}}^{\mathrm{DFT-D}}$ on each metal substrate, we plotted $Z_{\mathrm{C}}^{\mathrm{DFT-D}}$ as a function of A for the three metal surfaces as shown in Fig. 4.12. Here, the distances of PTCDA on noble metals are based on the experimental results in Ref. [41].

On Cu, $Z_{\mathrm{C}}^{\mathrm{DFT-D}}$'s are the range from 0.27 to 0.29 nm, except for the pentacene/Cu system. The deviation of the pentacene/Cu system is probably because the chemical interaction is much stronger than those of other systems. On Ag and Au, $Z_{\mathrm{C}}^{\mathrm{DFT-D}}$'s are the range from 0.29 to 0.31 nm and from 0.31 to 0.33 nm, respectively. In this way, on each metal surface, $Z_{\mathrm{C}}^{\mathrm{DFT-D}}$ does not significantly depend on A. This presumably comes from the repulsion of adsorbate electrons with substrate electrons, that is to say the Pauli repulsion effect is stronger, if that the adsorbate has stronger chemical reactivity. These results indicate that the balance of the chemical interaction with the Pauli repulsion effect makes $Z_{\mathrm{C}}^{\mathrm{DFT-D}}$ nearly constant on each metal surface.

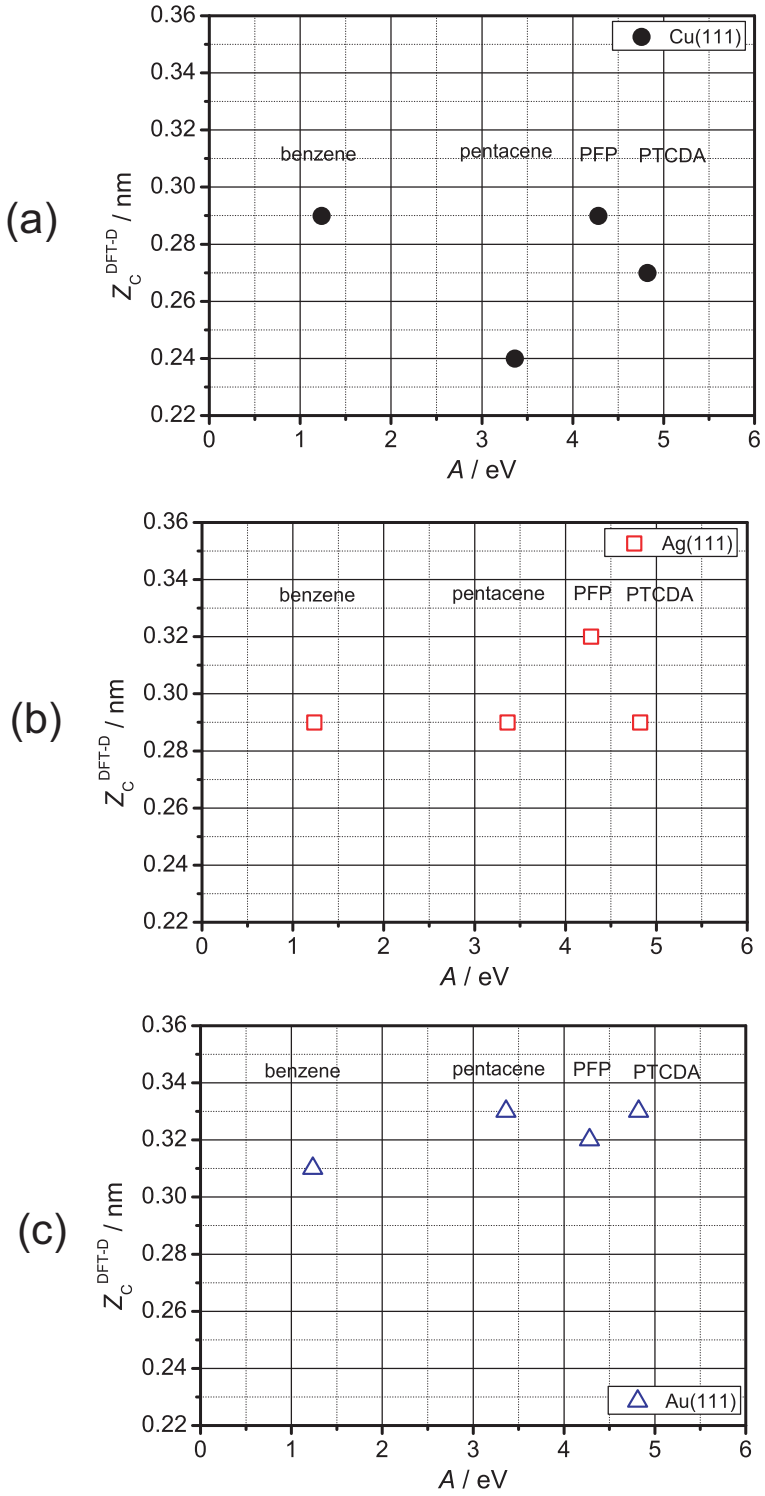

Figure 4.12: The calculated adsorption distance (Z_C^{DFT-D}) as a function of the electron affinity of the adsorbate (A) on (a) Cu(111), (b) Ag(111), and (c) Au(111). The distances of PTCDA on noble metals are base on the experimental results in Ref. [41].

Interface dipole

In order to understand the origins of the interface dipole quantitatively, we partition the interface dipole into three components, chemical one ($\Delta\phi_{\rm chem}$), physical one ($\Delta\phi_{\rm phy}$), and molecular one ($\Delta\phi_{\rm mol}$),

$$\Delta\phi = \Delta\phi_{\rm chem} + \Delta\phi_{\rm phy} + \Delta\phi_{\rm mol}. \tag{4.13}$$

As described in 3.3, for the PFP/metal systems $\Delta\phi_{\rm mol}$ contributes to $\Delta\phi$, and thus we extract $\Delta\phi_{\rm mol}$ from $\Delta\phi$. As shown in the preceding section, the adorbate-substrate distance is almost constant on each metal surface, and we thus consider that $\Delta\phi_{\rm phy}$ is independent on the adsorbate. Consequently, only $\Delta\phi_{\rm chem}$ depends on the chemical reactivity of the adsorbate. Then, by using Gauss's law [37], the $\Delta\phi_{\rm chem}$ can be modeled by

$$\Delta\phi_{\rm chem} = \frac{Z_{\rm C}}{\epsilon_0}\frac{\Delta N^{\rm A}}{A_0}. \tag{4.14}$$

In this expression, $\Delta N^{\rm A}$ is dependent on A of the adsorbate.

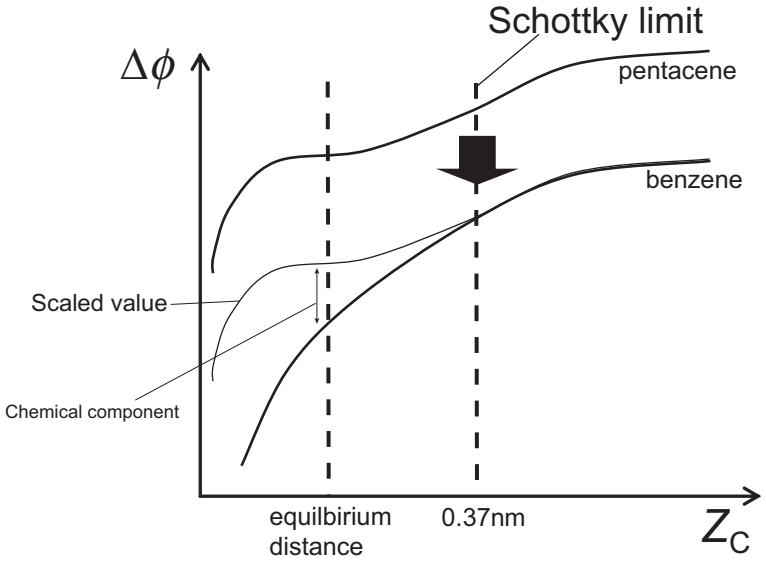

Figure 4.13: Schematic diagram of the way to extract the chemical component of the interface dipole by scaling the work function change for an adsorbate-metal system.

To extract the chemical component of the interface dipole, we need to scale the work function change to uniform the geometric factor, that is to say, surface molecular density, as shown in Fig. 4.13. Here, we assume that the interface dipole of a benzene/metal system includes only physical component. Thus, we scale the work function changes at $Z_{\rm C} = 0.37$ nm to coincide with that at the same $Z_{\rm C}$ for the

benzene/metal system. Note that the interface at $Z_{\mathrm{C}} = 0.37$ nm is in the Schottky limit.

As seen in Fig. 4.14, on Cu and Ag, the relationship between $\Delta\phi_{\mathrm{chem}}$ and A is approximation linear. In contrast, on Au, $\Delta\phi_{\mathrm{chem}}$ is not dependent on A. These results indicate the chemical reactivity of the surfaces, which means that Cu and Ag surfaces are chemical reactive whereas a Au surface is chemical inert.

On Cu and Ag, ΔN^{A} is derived on the basis of the results of $\Delta\phi_{\mathrm{chem}}$ and Eq. (4.14), and we show the results in Fig. 4.15. Here, the adsorbate-metal distances (Z_{C}) on Cu(111) and Ag(111) are assumed to be 0.29 and 0.30 nm, respectively. As shown in Fig. 4.15, ΔN^{A} is largely related to A, ΔN^{A}'s are estimated to be the range from 0.05 to 0.16 electrons.

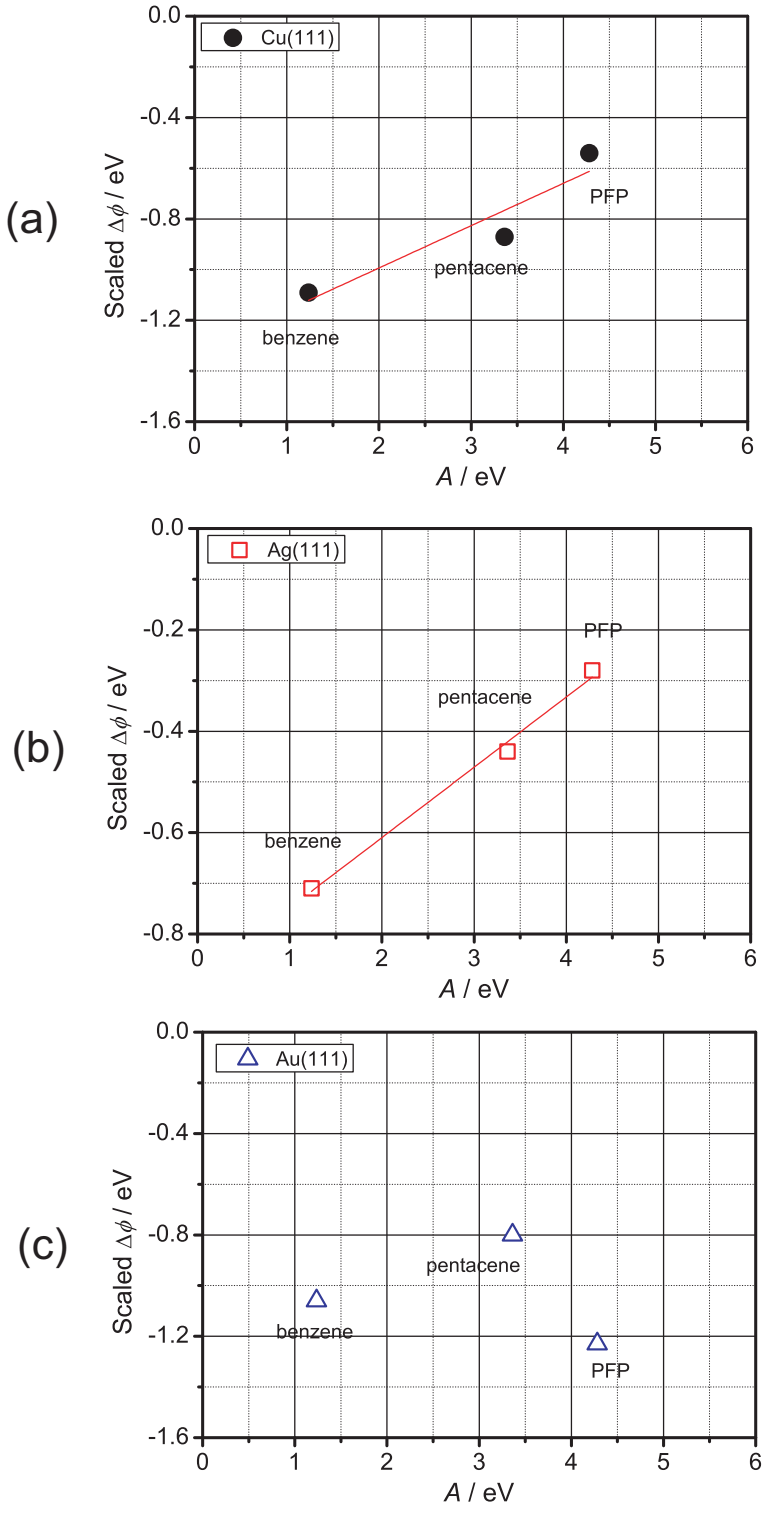

Figure 4.14: The scaled work function change ($\Delta\phi$) as a function of the electron affinity of the adsorbate (A) on (a) Cu(111), (b) Ag(111), and (c) Au(111).

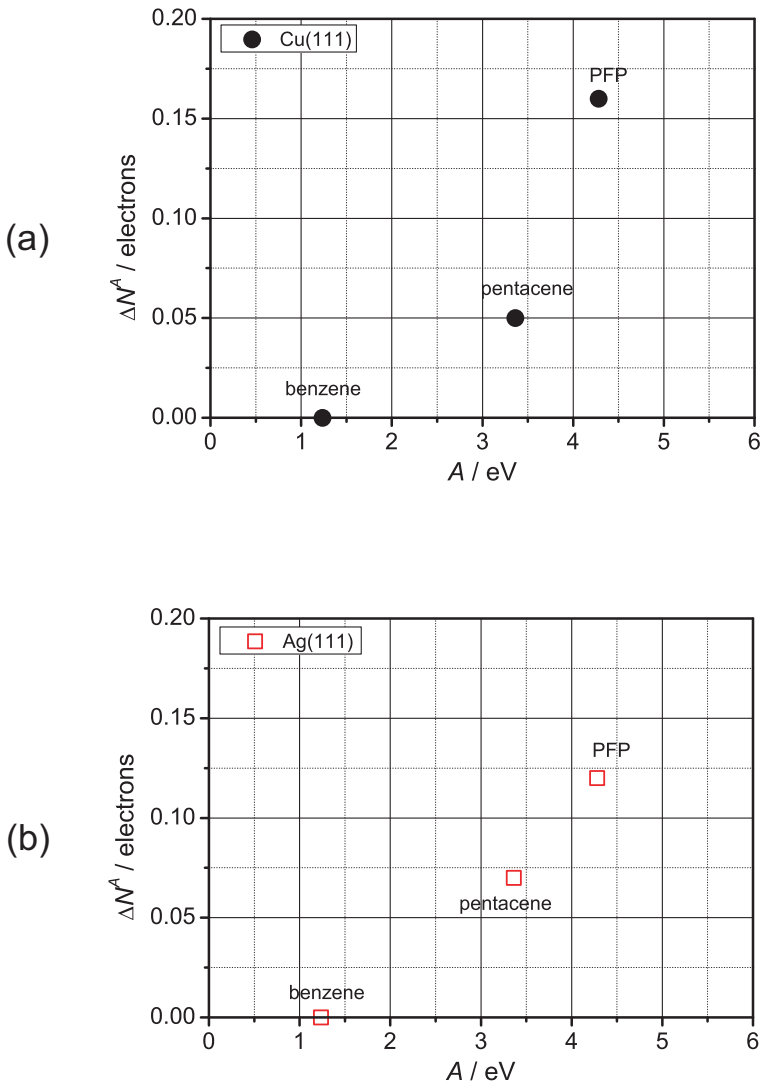

Figure 4.15: The number of electrons transferred from substrate to adsorbate (ΔN^{A}) as a function of the electron affinity of the adsorbate (A) on (a) Cu(111) and (b) Ag(111).

4.3 Summary

We have examined the IDIS model using first-principles calculations. At large distance, the vacuum level shift estimated by the IDIS model agrees with that estimated by self-consistent GGA calculations. On the other hand, at small distance, the two values branch off because of the back donation from the substrate to the molecule. Thus, the IDIS model does not work well if the chemical interaction is strong.

We have investigated factors determining the interface dipole from the viewpoint of chemical trend within electron affinity model. On each metal surface, the adsorption distance is nearly constant with any adsorbate, which indicates the physical component of the interface dipole is independent on adsorbate. We extract the chemical component to uniform the geometric factor. On Cu and Ag surface, the relationship between the chemical component of the interface dipole and the electron affinity is approximately linear, whereas on Au, the chemical component does not significantly depend on the electron affinity. These results show the chemical reactivity of metal surface determines the chemical contribution to the interface dipole. Therefore, the main factor of the interface dipole depending on adsorbate is the chemical contribution, which indicates that the relationship can predict the vacuum level shift of organic/metal interfaces.

Chapter 5

Conclusions

We have studied the electronic structures of π conjugate molecules (benzene, pentacene, and perfluoropentacene(PFP)) adsorbed on noble metal surfaces by using first-principles calculations, to clarify the origins of the interface dipoles.

We employed the semiempirical van der Waals (DFT-D) methods and the van der Waals density functional (vdW-DF) methods to include the long-range vdW interactions. The DFT-D method can reproduce the accurate distance between the molecule and the substrate. In contrast, the vdW-DF method systematically overestimates the distance. On Ag and Au, the distances for the adsorbed system are almost the same, reflecting that the Ag and Au surface are chemically inert. On the other hand, on Cu, the adsorption distances are different for different adsorbate. In particular, the distance for the pentacene/Cu interface is smaller than that for the benzene/Cu interface, reflecting that pentacene is more chemically reactive than benzene. In contrast, the distance for the PFP/Cu interface is larger than that for the pentacene/Cu interface, although PFP is more chemically reactive than pentacene. This is presumably because of the repulsion between $2p$ electrons of F atoms and electrons of substrate. Thus, these results indicate that functional group can control adsorption distance. The work function change is sensitive to the molecule-substrate distance, and thus the molecule-substrate distance is a key parameter for the interfacial electronic state. The calculated work function changes at the molecule-substrate distances calculated by DFT-D are in good agreement with the experimental values, which shows that the DFT-D method can predict the vacuum level shift of organic/metal interfaces accurately. The analysis

of slope parameter shows the electronic and the geometric contribution to the interface dipole. For benzene-adsorbed systems, the geometric factors are the main origin, whereas for pentacene-adsorbed, PFP-adsorbed systems, not only the geometric factors but also the electronic factor contribute to the interface dipole. Moreover, for the PFP-adsorbed system, the intramolecular dipole also contributes to the interface dipole. The calculated electronic structures show that for Au, a physical factor dominates the molecule-substrate interaction whereas for Cu and Ag, a chemical factor contributes to the interaction if the molecule is rather chemical reactive such as pentacene and PFP.

We have examined the induced density interface states (IDIS) model by using first-principles calculation. The IDIS model can describe well if the molecule-metal interaction is weak. On the other hand, it cannot describe if the interaction is strong, because of the back-donation from the substrate to the adsorbate. Thus, we partition the interface dipole into physical component and chemical component, and we examine the dependence of each component on the electron affinity of the adsorbate. On each surface, the adsorption distances are almost constant with any adsorbate, because of the balance between the chemical reactivity and the repulsion of electrons of the adsorbate with those of the substrate. We consider that the physical component of the interface dipole is independent on adsorbate, and consequently that the chemical component depends on adsorbate. Then, we extract the chemical component by coinciding the geometric factors with those of the benzene-adsorbed systems. The results show that the chemical component depends on the electron affinity of the adsorbate. Moreover, the back donation can be estimated from the chemical component. Therefore, these results indicate that the chemical trend can predict the vacuum level shifts of organic/metal interfaces.

In future, we need to investigate the effect of electric field and impurities on the interfacial electronic structures toward the design of the electrode for real organic devices.

Appendix A

Density functional theory

A.1 Hohenberg-Kohn theorem

Hohenberg and Kohn [122] established the density functional theory (DFT) in which the many body system can be expressed in terms of single particle density. The Hamiltonian of an electronic system in which there are interacting N-electrons in the external potential given by

$$\begin{aligned} H &= T + U + V, && \text{(A.1)} \\ &= \sum_{i}^{N} (-\nabla_i^2) + \frac{1}{2} \sum_{i \neq j} \frac{2}{|\mathbf{r}_{ij}|} + \sum_{i}^{N} V_{\text{ext}}(\mathbf{r}_i), && \text{(A.2)} \end{aligned}$$

where the first term is the kinetic energy, the second term is the electron-electron Coulomb repulsion, and the third term is the interaction with the external potential including the electrostatic potential with the fixed nuclei. It should be noted that in this section we employ the system of Rydberg atomic unit to describe the mathematical expressions.

The DFT is consist of two theorems.

The fist theorem is: *The external potential is a unique functional of the electron density n(*$\mathbf{r}$*) and the energy is described by a unique functional of n(*$\mathbf{r}$*).* Thus, the energy, $E[n]$ is given by

$$E[n] = F[n] + \int V_{\text{ext}}[n(\mathbf{r})] \mathrm{d}\mathbf{r}, \qquad \text{(A.3)}$$

where $F[n] = \langle\psi|T + U|\psi\rangle$, and ψ is a wave function of the ground state. This theorem expresses that if the electron density $n(\mathbf{r})$ is given, all quantities of the ground state are determined uniquely.

The second theorem is: *For a given $V_{\rm ext}$, the correct charge density of the ground state minimizes the energy functional (The energy variational principle).* Thus, if the universal functional $F[n]$ were known, it would be relatively simple to use the variational principle to determine the energy and charge density of the ground state for any specified external potentials. However, the exact form of the functional $F[n]$ is unknown.

A.1.1 Kohn-Sham equation

To enable practical use of Hohenberg-Kohn theorem, Kohn and Sham [123] redefined $F[n]$ as follows;

$$F[n] \equiv T_0[n] + \frac{1}{2}\int\int \frac{2n(\mathbf{r})n(\mathbf{r}')}{|\mathbf{r}-\mathbf{r}'|}\mathrm{d}\mathbf{r}\mathrm{d}\mathbf{r}' + E_{\rm xc}[n], \tag{A.4}$$

where the first term is the kinetic energy of *non-interacting* electron system, the second term is the classical Hartree term, and the third term is called the exchange-correlation energy.

Using the variational principle, the problem of searching the ground state is reduced to solving one-particle equations (Kohn-Sham equation);

$$[-\nabla^2 + V_{\rm eff}(\mathbf{r})]\psi_i(\mathbf{r}) = \varepsilon_i\psi_i(\mathbf{r})], \tag{A.5}$$

which gives the exact charge density of the ground state $n(\mathbf{r})$. The density $n(\mathbf{r})$ is given by

$$n(\mathbf{r}) = \sum_i^N |\psi_i(\mathbf{r})|^2 \tag{A.6}$$

The effective potential is given as;

$$V_{\rm eff}(\mathbf{r}) = \int \frac{2n(\mathbf{r}')}{|\mathbf{r}-\mathbf{r}'|}\mathrm{d}\mathbf{r}' + V_{\rm ext}(\mathbf{r}) + \mu_{\rm xc}(\mathbf{r}), \tag{A.7}$$

where $\mu_{\rm xc}(\mathbf{r})$ is the exchange-correlation potential defined as

$$\mu_{\rm xc}(\mathbf{r}) \equiv \frac{\delta E_{\rm xc}[n(\mathbf{r})]}{\delta n(\mathbf{r})}. \tag{A.8}$$

A.1.2 Approximation for the exchange-correlation energy

In order to solve the Kohn-Sham equation in practice, we introduce approximations for the exchange-correlation energy.

One of the approximations is the local density approximation (LDA). The exchange-correlation energy is given by

$$E_{\rm xc}^{\rm LDA}[n] = \int \varepsilon_{\rm xc}^{\rm LDA}[n(\mathbf{r})]n(\mathbf{r})\mathrm{d}\mathbf{r}, \tag{A.9}$$

if we assume that the exchange-correlation energy behaves locally as in a homogeneous electron gas system. The exchange-correlation potential is given as follows;

$$V_{\rm xc}^{\rm LDA}(\mathbf{r}) = \frac{\delta \varepsilon_{\rm xc}^{\rm LDA}[n]}{\delta n(\mathbf{r})}. \tag{A.10}$$

Useful estimates of $\varepsilon_{\rm xc}^{\rm LDA}[n(\mathbf{r})]$ and the corresponding potentials $V_{\rm ext}(\mathbf{r})$ have been given by Hedin and Lundqvist [124], von Barth and Hedin [125], and Gunnarsson and Lundqvist [126]. This approximation was designed to work with systems in which the electronic charge density is expected to be smooth. It typically provides good agreement with experimental results of structural and vibrational properties. However, it usually overestimates bonding energies and underestimated equilibrium bond distances compared with experimental values.

In order to overcome the difficulties of LDA, generalized gradient approximation (GGA) were introduced. Within GGA, the exchange-correlation energy is a functional not only of the density but also of its local spatial variations;

$$E_{\rm xc}^{\rm GGA} = \int \varepsilon_{\rm xc}^{\rm GGA}[n(\mathbf{r}), |\nabla n(\mathbf{r})|]n(\mathbf{r})\mathrm{d}\mathbf{r}. \tag{A.11}$$

Several expressions of the exchange-correlation energy have been described in different formulations of the GGA functionals. Among these, the Perdew-Burke-Ernzherof (PBE) expression was chosen in this

work [65]. The exchange-correlation potential is expressed as:

$$V_{\mathrm{xc}}^{\mathrm{GGA}}(\mathbf{r}) = \frac{\delta \varepsilon_{\mathrm{xc}}^{\mathrm{GGA}}[n]}{\delta n(\mathbf{r})}. \tag{A.12}$$

The GGA is actually able to cure the defect of LDA, and generally provides better description of the structural properties of covalent materials. In particular, it improves significantly the binding energies of covalent materials, whereas LDA completely tends to fail. For example, for bulk iron, GGA can accurately predict that it has a ferromagnetic bcc ground state, whereas LDA wrongly predicts that it has a paramagnetic fcc one.

However, LDA and GGA are not able to describe long-range van der Waals (vdW) interactions. In order to include the vdW interactions, the correction of vdW to the energy should be taken.

A.1.3 Pseudopotential method

In order to solve the Kohn-Sham equations by practical calculations, we need to transform the original integro-differential problem into a more tractable algebraic one. This can be achieved by expanding the electronic wavefunctions on a basis set and using this representation in all operators in the Hamiltonian. The plane wave basis set [127] is chosen in this work, and it takes advantage because of efficient algorithms such as the fast Fourier transform (FFT). The Bloch electronic wavefunction can thus be represented as:

$$\psi_{i,\mathbf{k}}(\mathbf{r}) = \frac{1}{\sqrt{N_{\mathrm{cell}}\Omega_{\mathrm{cell}}}} \sum_{m} c_{i,m}(\mathbf{k}) e^{i(\mathbf{k}+\mathbf{G}_m)\cdot\mathbf{r}}, \tag{A.13}$$

where N_{cell} is the number of the unit cell, Ω_{cell} is the volume of the unit cell, and the $c_{i,m}(\mathbf{k})$ are orthonormal vectors in the discrete index m of the reciprocal lattice vector $\mathbf{G}_m$ in the following:

$$\sum_{m} c_{i,m}^{*}(\mathbf{k}) c_{i',m}(\mathbf{k}) = \delta_{i,i'}. \tag{A.14}$$

Using this expression, the Kohn-Sham equations can be written in reciprocal space as:

$$\sum_{m'} H_{m,m'}(\mathbf{k}) c_{i,m'}(\mathbf{k}) = \varepsilon_i(\mathbf{k}) c_{i,m}(\mathbf{k}), \tag{A.15}$$

where $H_{m,m'}(\mathbf{k}) = |\mathbf{k}+\mathbf{G}_m|^2\delta_{m,m'} + V_{\text{eff}}(\mathbf{G}_m - \mathbf{G}_{m'})$. Here we have labeled the eigenvalues and eigenfunctions $i = 1, 2, ...,$ for the discrete set of solutions of the matrix equations for a given $\mathbf{k}$. As we are studying the ground state properties of the system, for each $\mathbf{k}$ point only a finite number of the lowest-energy electronic states are required to be calculated to obtain the charge density. The obtained charge density is then used to construct a new guess of the potential to be reintroduced in the Kohn-Sham equations for the successive step of the iterative diagonalization. Of course, the plane wave expansion is exact in the limit of infinite number of $\mathbf{G}$ vectors. In practice, one can deal with only a finite number of plane waves, and usually chooses those contained in a sphere of maximum kinetic energy E_{cut}, the energy cut-off:

$$|\mathbf{k}+\mathbf{G}_m|^2 \leq E_{\text{cut}}. \tag{A.16}$$

The accuracy is determined by E_{cut}, and the space resolution is $2\pi/\sqrt{E_{\text{cut}}}$.

Unfortunately, the plane wave expression uses the same resolution in each region, and thus we would need an intractably large number $\mathbf{G}_m$ vectors if we described the ionic core accurately. The pseudopotential technique can overcome the difficulty, given that the most relevant physical properties are brought about by the valence electrons whereas the ionic core can be considered as frozen in their atomic configurations. The valence electrons thus move in the effective external field produced by these inert ionic cores. The pseudopotential technique tries to reproduce the interaction of the true atomic potential on the most external state without explicitly including the core states in the calculations. The internal electrons remain frozen, whereas for external ones a pseudo wavefunction can built to be smooth and nodeless inside the core. Note that it keeps the total valence charge in this region conserving (norm conserving pesudopotential). Because of the smooth and nodeless of the pseudo wavefunction, the calculations can be performed with a reasonable number of plane waves.

In order to reproduce the scattering properties of the all-electrons (AE) wavefunctions of several angular momenta, it is usually necessary to split the pseudopotential into the two part, i.e. a local part (matching the real full potential outside core) and a nonlocal one (vanishing outside the core). Note that the nonlocal part acts in different ways on different angular momentum channel. The first expression for this nonlocal part was given in a semi-local form [128, 129, 130, 131], where the non-locality is built

just on angular coordinates:

$$V(\mathbf{r},\mathbf{r}') = V_{\rm loc}(\mathbf{r})\delta(\mathbf{r}-\mathbf{r}') + \sum_{l=0}^{l_{\rm max}} V_l(\mathbf{r})\delta(\mathbf{r}-\mathbf{r}')P_l(\mathbf{r},\mathbf{r}'), \tag{A.17}$$

where $V_{\rm loc}$ is the local part, V_l is the nonlocal l-dependent model pseudopotential, and P_l is the projector operator onto the l angular momentum subspace. In order to make the plane wave calculations more efficient, Kleiman and Bylander (KB) [132] replaced the above semi-local expression with a fully separable form:

$$V(\mathbf{r},\mathbf{r}') = V_{\rm loc}(\mathbf{r})\delta(\mathbf{r}-\mathbf{r}') + \sum_i |i\rangle V_i \langle i|, \tag{A.18}$$

where V_i is the KB potential and the wavefunctions $|i\rangle$ are atomic pseudo-states. $|i\rangle$ are modified such that the KB potential reproduces the action of the original semi-local one on the reference atomic pseudo-wavefunctions.

Vanderbilt introduced the most complete generalization of the scheme, and found an ulatrasoft pseudopotential method to increase the transferability of the pseudopotentials [67]. The region of energy corresponding to occupied states in the crystals is sampled with more than one projector so that the index in Eq. (A.18) runs not only on the atomic reference states but also, for each angular momentum, on a set of energy values around them used to reproduce the correct scattering properties of the ion. This requires a generalization of the expression (A.18), in which the nonlocal part is described as:

$$V_{\rm nl} = \sum_{i,j} B_{ij}|\beta_i\rangle\langle\beta_j|, \tag{A.19}$$

where the functions $|\beta_i\rangle$ are built by the chosen pseudowavefunctions, the matrix B_{ij} is an hermitian operator built by using the same quantities. The ultrasoft pseudopotential relaxes the norm conserving condition, and thus the pseudowavefunction inside the core can be as smooth as possible. This is possible by introducing a generalized overlap operator:

$$\hat{S} = 1 + \sum_{i,j} q_{i,j}|\beta_i\rangle\langle\beta_j|, \tag{A.20}$$

so that the orthonormality condition to be satisfied in the solution of the Kohn-Sham equations is:

$$\langle\psi_i|\hat{S}|\psi_j\rangle = \delta_{ij}. \tag{A.21}$$

In these expressions, $q_{i,j}$ is the integral of the augmentation charge density,

$$q_{i,j} = \int \mathrm{d}\mathbf{r} Q_{i,j}(\mathbf{r}), \tag{A.22}$$

$$Q_{i,j}(\mathbf{r}) = \psi_i^{\mathrm{AE}*}(\mathbf{r})\psi_j^{\mathrm{AE}}(\mathbf{r}) - \psi_i^{\mathrm{PS}*}(\mathbf{r})\psi_j^{\mathrm{PS}}(\mathbf{r}), \tag{A.23}$$

where the wavefunctions $\psi_i^{\mathrm{AE}}(\mathbf{r})$ and $\psi_i^{\mathrm{PS}}(\mathbf{r})$ are the all-electron ones and the pseudo ones of the atomic states, respectively. Because of this generalization, the charge density is required to be completed with the augmentation part on the ionic cores:

$$n(\mathbf{r}) = \sum_{i,\mathbf{k}} f_{i,\mathbf{k}} \left(|\psi_{i,\mathbf{k}}|^2 + \sum_{I,i,j} Q_{i,j}^I(\mathbf{r} - \mathbf{R}_I)\langle\psi_{i,\mathbf{k}}|\beta_i^I\rangle\langle\beta_i^I|\psi_{j,\mathbf{k}}\rangle \right), \tag{A.24}$$

where $f_{i,\mathbf{k}}$ is the fractional occupation of the state, I is the index of the ions, R_I is the position of the ions, $Q_{i,j}^I$ is the augmentation charge for the ions. The modification in $n(\mathbf{r})$ also involves the expression of the potential in the Kohn-Sham equations. The external potential is described by

$$V(\mathbf{r},\mathbf{r}') = V_{\mathrm{loc}}(\mathbf{r})\delta(\mathbf{r}-\mathbf{r}') + \sum_{I,i,j} D_{i,j}^{\mathrm{ion},I}|\beta_i^I\rangle\langle\beta_j^I|. \tag{A.25}$$

In this expression, the coefficients $D_{i,j}^{\mathrm{ion},I}$ need to be calculated as:

$$D_{i,j}^{\mathrm{ion},I} = D_{i,j}^I - \int \mathrm{d}\mathbf{r} V_{\mathrm{eff}}(\mathbf{r}) Q_{i,j}^I(\mathbf{r} - \mathbf{R}_I), \tag{A.26}$$

$$D_{i,j}^I = B_{i,j}^I + \varepsilon_j q_{i,j}^I. \tag{A.27}$$

This finally leads to the generalized eigenvalue problem:

$$\left(-\nabla^2 + \sum_{I,i,j} D_{i,j}^{\mathrm{ion},I}|\beta_i^I\rangle\langle\beta_j^I| + V_{\mathrm{eff}} \right) \psi_{i,\mathbf{k}} = \varepsilon_{i,\mathbf{k}}\hat{S}\psi_{i,\mathbf{k}}. \tag{A.28}$$

As evident from the last expression, the pseudopotential needs to be updated at each iteration, and this makes it participate to the screening process, further increasing its transferability. Although we can obtain the advantages introduced by ultrasoft pseudopotentials, we need a very large cut-off energy to describe the augmentation charge density. However, this term affects only the calculation of $n(\mathbf{r})$, and does not the diagonalization process.

Appendix B

van der Waals corrections to the density functional energy calculations

B.1 semiempirical van der Waals method

Grimme [52] proposed the semiempirical van der Waals (DFT-D) method, which is based on a damped atom-pairwise dispersion corrections of the form $C_6 R^{-6}$, where C_6 represents the dispersion coefficient for a given atom pair, and R is the distance between the atoms. The DFT-D total energy is give by Eq.(2.1).

E^{disp} is a semiempirical dispersion correction given by

$$E_{\text{disp}} = -s_6 \sum_{i=1}^{N-1} \sum_{j=i+1}^{N} \frac{C_6^{ij}}{R_{ij}^6} f_{\text{damp}}(R_{ij}), \tag{B.1}$$

where N is the number of atoms in the system, C_6^{ij} denotes the dispersion coefficient for atom pair ij, s_6 is a global scaling factor that only depends on the density functional used, and R_{ij} is an interatomic distance. In order to avoid near-singularities for small R, a damping function, f_{damp}, must be used,

which is given by

$$f_{\mathrm{damp}}(R_{ij}) = \frac{1}{1 + e^{d(R_{ij}/R_r - 1)}}, \tag{B.2}$$

where $d = 20$, and R_r is the sum of atomic vdW radii. These values are derived from the radius of the $0.01 a_0^{-3}$ electron density contour from ROHF/TZV computations of the atoms in the ground state.

The combination rule for C_6^{ij} is defined as

$$C_6^{ij} = \sqrt{C_6^i C_6^j}, \tag{B.3}$$

where C_6^i and C_6^j are the atomic C_6 coefficient. The C_6 coefficient for atom a (in Jnm^6 mol^{-1}) is given by

$$C_6^{\mathrm{a}} = 0.05 N I_p^{\mathrm{a}} \alpha^{\mathrm{a}}, \tag{B.4}$$

where N has values 2, 10, 18, 36, and 54 for atoms from rows 1-5 of the periodic table, I_p^{a} is the atomic ionization potential which is based on the DFT/PBE0 calculations, and α is the static dipole polarizabilities. The C_6 parameters and van der Waals radii R_r for elements H-Xe are summarized in Table 1 in Ref. [52].

The s_6 scale factors have been determined by least-squares optimization of interaction energy deviations for the 40 noncovalently bound complexes, and are found to be 0.75 for the GGA-PBE exchange-correlation functional.

B.2 van der Waals density functional

The van der Waals density functional (vdW-DF) procedure [58, 59] is in short

$$E_{\rm xc}[n] = E_{\rm x}^{\rm GGA}[n] + E_{\rm c}[n], \tag{B.5}$$

that (i) is to take an appropriately selected GGA exchange functional, (ii) to develop a properly constructed *nonlocal* correlation functional that includes an account of vdW forces, and (iii) to perform calculations with some efficient and accurate electron structure scheme, for instance, with plane-wave and real-space codes. The computational cost for vdW-DF [58, 59] are comparable to ordinary DFT. By using the functional derivative of $E_{\rm c}$ with respect to the density $n(\mathbf{r})$ as a component of the Kohn-Sham electron potential [123], the calculation are made fully self-consistent.

The revPBE exchange [133] is usually chosen because it best eliminates the spurious bonding from exchange alone, but the fact that it is not perfect is reflected in the slightly longer bonds obtained with it. Nevertheless it has proved a good match for the vdW-DF correlation functional in giving better equilibrium energies than when HF exchange is used. The search for an improved exchange functional has high priority.

The correlation energy is split into short- and long-ranged parts:

$$E_{\rm c}[n] = E_{\rm c}^{0}[n] + E_{\rm c}^{\rm nl}[n], \tag{B.6}$$

where $E_{\rm c}^{0}[n]$ is the short-ranged term and $E_{\rm c}^{\rm nl}[n]$ is the long-ranged term. $E_{\rm c}^{0}$ is evaluated in LDA, which implicitly uses the exact dielectric function. The long-ranged term, $E_{\rm c}^{\rm nl}$, depends nonlocally on the density, and contains the principle vdW terms. It is also much smaller in magnitude and in positional sensitivity, so it can be evaluated with a lower accuracy. in particular, in the vdW-DF, it is evaluated with a simple model dielectric function.

As a matter of fact, in the vdW-DF, the key ingredients of this long-range (nonlocal) part of the correlation functional are (i) the adiabatic-connection formula [126, 134, 135] as the starting point, (ii) an approximate coupling-constant integration, (iii) which as in the planar case [136] is exact for

the asymptotic long-range vdW term, (iv) the use of an approximate dielectric function ε in a single-pole form, (v) which is fully nonlocal and satisfies known limits, sum rules and invariances, (vi) whose pole position is scaled to give exact electron-gas ground-state energy locally, including the appropriate gradient correction (the pole strength is determined by a sum rule) and (vii) the lack of empirical or fitted parameter.

The form of the general-geometry functional for $E_{\rm c}^{\rm nl}[n]$ derived in [58] is

$$E_{\rm c}^{\rm nl} = \int\int {\rm d}\mathbf{r}{\rm d}\mathbf{r}' n(\mathbf{r}) K(\mathbf{r},\mathbf{r}') n(\mathbf{r}'), \tag{B.7}$$

where the kernel $K(\mathbf{r},\mathbf{r}')$ has been derived based on the adiabatic connection fluctuation dissipation theorem, the random phase approximation (RPA), and using a plasmon pole model for the polarizability. The short-range part is treated in LDA whereas the long-range part has nonlocal component. This is why double counting is avoided.

Bibliography

[1] H. Akamatu and H. Inokuchi. On the electrical conductivity of violanthrone, iso-violanthrone, and pyranthrone. *J. Chem. Phys.*, 18(6):810–811, 1950.

[2] H. Akamatu, H. Inokuchi, and Y. Matsunaga. Electrical conductivity of the perylene-bromine complex. *Nature*, 173:168–169, 1954.

[3] H. Akamatu, H. Inokuchi, and Y. Matsunaga. Organic semiconductor with high conductivity. i. complexes between polycyclic aromatic hydrocarbon an halogens. *Bulletin of the Chemical of Society of Japan*, 29(2):213–219, 1956.

[4] H. Ehrenreich and F. Spaepen, editors. *Solid State Physics, Advances in Research and Applicaltions*. Academic Press, 1994.

[5] R. B. Kanner and A. G. MacDiarmid. Plastics that conduct electricity. *Sci. Am.*, 258(2):106–112, 1988.

[6] P. Yam. Plastics get wired. *Sci. Am.*, 273(1):82–87, 1995.

[7] A. J. Heeger, S. Kivelson, J. R. Schrieffer, and W. P. Su. Solitons in conducting polymers. *Rev. Mod. Phys.*, 60(3):781–850, 1988.

[8] T. A. Skotheim, editor. *Handbook of Conducting Polymers*, volume 1-2. Marcel Dekker Inc., 1986.

[9] C. J. Drury, C. M. J. Mutsaers, C. M. Hart, M. Matters, and D. M. de Leeuw. Low-cost all-polymer integrated circuits. *Appl. Phys. Lett.*, 73(1):108–110, 1998.

[10] L. S. Hung and C. H. Chen. Recent progress of molecular organic electroluminescent materials and devices. *Mater. Sci. Eng. R.*, 39(5-6):143–222, 2002.

[11] C. W. Tang and S. A. VanSlyke. Organic electroluminescent diodes. *Appl. Phys. Lett.*, 51(12):913–915, 1987.

[12] J. H. Burroughers, D. D. C. Bradley, A. R. Brown, R. N. Marks, K. Mackay, R. H. Friend, P. L. Burn, and A. B. Holmes. Light-emitting diodes based on conjugated polymers. *Nature*, 347(6293):539–541, 1990.

[13] R. H. Friend, R. W. Gymer, A. B. Holmes, J. H. Burroughes, R. N. Marks, C. Taliani, D. D. C. Bradley, D. A. Dos Santos, J. L. Brédas, M. Lögdlund, and W. R. Salaneck. Electroluminescence in conjugated polymers. *Nature*, 397(14):466–469, 1999.

[14] F. Li, H. Tang, J. Shinar, O. Resto, and S. Z. Weisz. Effects of aquaregia treatment of indium-tin-oxide substrates on the behavior of double layered organic light-emitting diodes. *Appl. Phys. Lett.*, 70(20):2741–2743, 1997.

[15] H. Koezuka, A. Tsumura, and T. Ando. Field-effect transistor with polythiophene thin film. *SM*, 18(1-3):699–704, 1987.

[16] C. D. Dimitrakopoulos and P.R.L. Malenfant. Organic thin film transistors for large area electronics. *Adv. Mater.*, 14(2):99–117, 2002.

[17] H. E. Katz and Z. Bao. The physical chemistry of organic field-effect transistors. *J. Phys. Chem. B*, 104(4):671–678, 2000.

[18] F. De Angelis, L. Mariucci, S. Cipolloni, and G. Fortunato. Analysis of electrical characteristics of high performance pentacene thin-film transistors with PMMA buffer layer. *Journal of Non-Crystaline Solids*, 352(9-20):1765–1768, 2006.

[19] H. Hoppe and N. S. Sariciftci. Organic solar cells: An overview. *J. Mater. Res.*, 19(7):1924–1945, 2004.

[20] C. W. Tang. Two-layer organic photovoltaic cell. *Appl. Phys. Lett.*, 48(2):183–185, 1986.

[21] L. S. Hung and C. H. Chen. Recent progress of molecular organic electroluminescent materials and devices. *Materials Science and Engineering: R*, 39(5-6):143–222, 2002.

[22] Y. Yang. Polymer electoluminescent devices. *MRS Bulletin*, 22(6):31–38, 1997.

[23] Y. G. Kozlov, G. Parthasarathy, P. E. Burrows, S. R. Forrest, Y. You, and M. E. Thompson. Optically pumped blue organic semiconductor lasers. *Appl. Phys. Lett.*, 72(5):144–146, 1998.

[24] G. Yu, K. Pakbaz, and A. J. Heeger. Semiconducting polymer diodes: Large size, low cost photodetectors with excellent visible-ultraviolet sensitivity. *Appl. Phys. Lett.*, 64(25):3422–3424, 1994.

[25] R. N. Marks, J. J. M. Halls, D. D. C. Bradley, R. H. Friend, and A. B. Holmes. The photovoltaic response in poly(p-phenylene vinylene) thin-film devices. *J. Phys.: Condens. Matter*, 6(7):1379–1394, 1994.

[26] G. Yu and A. J. Heeger. Charge separation and photovoltaic conversion in polymer composites with internal donor/acceptor heterojunctions. *J. App. Phys.*, 78(7):4510–4515, 11995.

[27] G. Yu, J. Gao, J. C. Hummelen, F. Wudl, and A. J. Heeger. Polymer photovoltaic cells: Enhanced efficiencies via a network of internal donor-acceptor heterojunctions. *Science*, 270(5243):1789–1791, 1995.

[28] X. Wei, M. Raikh, Z. V. Vardeny, Y. Yang, and D. Moses. Photoresponse of poly(para-phenylenevinylene) light-emitting diodes. *Phys. Rev. B*, 49(24):17480–17483, 1994.

[29] J. Gao, F. Hide, and H. Wang. Efficient photodetectors and photovoltaic cells from composites of fullerenes and conjugated polymers: photoinduced electron transfer. *Synth. Met.*, 84(1-3):979–980, 1997.

[30] J. J. M. Halls, C. A. Walsh, N. C. Greenham, E. A. Marseglia, R. H. Friend, S. C. Moratti, and A. B. Holmes. Efficient photodiodes from interpenetrating polymer networks. *Nature*, 376(10):498–500, 1995.

[31] B. A. Gregg. Photovoltaic properties of a molecular semiconductor modulated by an exciton-dissociating film. *Appl. Phys. Lett.*, 67(9):1271–1273, 1995.

[32] K. Yoshino, K. Tada, A. Fujii, E. M. Conwell, and A. A. Zakhidov. Novel photovoltaic devices based on donor-acceptor molecular and conducting polymer systems. *IEEE Trans. Electron Devices*, 44(8):1315–1324, 1997.

[33] C. J. Brabec, S. E. Shaheen, C. Winder, and N. S. Sariciftci. Effect of LiF/metal electrodes on the performance of plastic solar cells. *Appl. Phys. Lett.*, 80(7):1288–1290, 2002.

[34] H. Spanggaard and F. C. Krebs. A brief history of the development of organic and polymeric photovoltaics. *Solar Energy Materials and Solar Cells*, 83(2-3):125–146, 2004.

[35] W. R. Salaneck, K. Seki, A. Kahn, and J. J. Pireaux, editors. *Conjugated Polymer and Molecular Interfaces*. Marcel Dekker, Inc., New York, Basel, 2002.

[36] H. Ishii, K. Sugiyama, E. Ito, and K. Seki. Energy level alignment and interfacial electronic structures at organic/metal and organic/organic interfaces. *Adv. Mater.*, 11(8):605–625, 1999.

[37] S. M. Sze and K. K. Ng. *Physics of Semiconductor Devices*. John Wiley & Sons, New York, 3rd edition, 2006.

[38] Y. Morikawa, H. Ishii, and K. Seki. Theoretical study of *n*-alkane adsorption on metal surfaces. *Phys. Rev. B*, 69(4):041403, 2004.

[39] L. Romaner, D. Nabok, P. Puschnig, E. Zojer, and C. Ambrosch-Draxl. Theoretical study of PTCDA adsorbed on the coinage metal surfaces, Ag(111), Au(111) and Cu(111). *New J. Phys.*, 11(5):053010, 2009.

[40] N. Koch, A. Gerlach, H. Glowatzki S. Duhm, A. Vollmer G. Heimel, Y. Sakamoto, T. Suzuki, J. Zegenhagen, J. P. Rabe, and F. Schreiber. Adsorption-induced intramolecular dipole: Correlating molecular conformation and interface electronic structure. *J. Am. Chem. Soc.*, 130(23):7300–7304, 2008.

[41] A. Gerlach, S. Sellner, F. Schreiber, N. Koch, and J. Zegenhagen. Substrate-dependent bonding distances of PTCDA: A comparative x-ray standing-wave study on Cu(111) and Ag(111). *Phys. Rev. B*, 75(4):045401, 2007.

[42] H. Vázquez, R. Qszwaldowski, P. Pou, J. Ortega, R. Pérez, F. Flores, and A. Kahn. Dipole formation at metal/PTCDA interfaces: Role of the charge neutrality level. *Europhys. Lett.*, 65(6):802–808, 2004.

[43] H. Vázquez, R. Qszwaldowski, J. Ortega, R. Pérez, and A. Kahn. Barrier formation at metal-organic interfaces: dipole formation and the charge neutrality level. *Appl. Surf. Sci.*, 234(1-4):107–112, 2004.

[44] H. Vázquez, W. Gao, F. Flores, and A. Kahn. Energy level alignment at organic heterojunctions: Role of the charge neutrality level. *Phys. Rev. B*, 71(4):041306, 2005.

[45] H. Vázquez, F. Flores, and A. Kahn. Induced density of states model for weakly-interacting organic semiconductor interfaces. *Org. Electron.*, 8(2-3):241–248, 2007.

[46] H. Vázquez, Y. J. Dappe, J. Ortega, and F. Flores. Energy level alignment at metal/organic semiconductor interfaces: "Pillow" effect, induced density of interface states, and charge neutrality level. *J. Chem. Phys.*, 126(14):144703, 2007.

[47] M. G. Betti, A. Kanjilal, C. Mariani, H. Vázquez, Y. J. Dappe, J. Ortega, and F. Flores. Barrier formation at organic interfaces in a Cu(100)-benzenethiolate-pentacene heterostructure. *Phys. Rev. Lett.*, 100(2):027601, 2008.

[48] E. Abad, J. Ortega, and F. Flores. Density functional theory calculations and the induced density of interface states model for noble metals/C_{60} interfaces. *J. Vac. Sci. Technol. B*, 27(4):2008–2011, 2009.

[49] E. Abad, Y.J. Dappe, J. Ortega, and F. Flores. Dipoles and band alignment for benzene/Au(111) and C_{60}/Au(111) interfaces. *Appl. Phys. A*, 95(1):119–124, 2009.

[50] S. Lee, B. Koo, J. Shin, E. Lee, and H. Park. Effects of hydroxyl groups in polymeric dielectrics on organic transistor performance. *Appl. Phys. Lett.*, 88(16):162109, 2006.

[51] Y. Inoue, Y. Sakamoto, T. Suzuki, M. Kobayashi, Y. Gao, and S. Tokito. Organic thin-film transistors with high electron mobility based on perfluoropentacene. *Jpn. J. Appl. Phys.*, 44(6A):3663–3668, 2005.

[52] S. Grimme. Semiempirical GGA-type density functional constructed with a long-range dispersion correction. *J. Comput. Chem.*, 27(15):1787–1799, 2006.

[53] F. Ortmann, W. G. Schmidt, and F. Bechstedt. Attracted by long-range electron correlation: Adenine on graphite. *Phys. Rev. Lett.*, 95(18):186101, 2005.

[54] F. Ortmann, F. Bechstedt, and W. G. Schmidt. Semiempirical van der waals correction to the density functional description of solids and molecular structures. *Phys. Rev. B*, 73(20):205101, 2006.

[55] N. Atodiresei, V. Caciuc, J.-H. Franke, and S. Blügel. Role of the van der waals interactions on the bonding mechanism of pyridine on Cu(110) and Ag(110) surface: First-principles study. *Phys. Rev. B*, 78(4):045411, 2008.

[56] N. Atodiresei, V. Caciuc, P. Lazić, and S. Blügel. Chemical versus van der waals interaction: The role of the heteroatom in the flat absorption of aromatic molecules C_6H_6, C_5NH_5, and $C_4N_2H_4$ on the Cu(110) surface. *Phys. Rev. Lett.*, 102(13):136809, 2009.

[57] E. McNellis, J. Meyer, and K. Reuter. Azobenzene at coinage metal surfaces: The role of dispersive van der waals interactions. *Phys. Rev. B*, 80(20):205414, 2009.

[58] M. Dion, H. Rydberg, E. Schröder, D. C. Langreth, and B. I. Lundqvist. Van der waals density functional for general geometries. *Phys. Rev. Lett.*, 92(24):246401, 2004.

[59] D. C. Langreth, B. I. Lundqvist, S. D. Chakarova-Käck, V. R. Cooper, M. Dion, P. Hyldgaard, A. Kelkkanen, J. Kleis, , L. Kong, S. Li, P. G. Moses, E. Murray, A. Puzder, H. Rydberg, E. Schröder, and T Thonhauser. A density functional for sparse matter. *J. Phys.: Condens. Matter*, 21(8):084203, 2009.

[60] K. Lee, J. Yu, and Y. Morikawa. Comparison of the localized basis and planewave basis for density functional calculations of organic molecules on metals. *Phys. Rev. B*, 75(4):045402, 2007.

[61] S. Yanagisawa and Y. Morikawa. Theoretical investigation on the electronic structure of the tris-(8-hydroxyquinolinato) aluminum/aluminum interface. *Jpn. J. Appl. Phys.*, 45(1B):413–416, 2006.

[62] S. Yanagisawa and Y. Morikawa. Important role of molecular permanent dipoles of the Alq_3/Al interface studied from first-principles. *Chem. Phys. Lett.*, 420(4-6):523–528, 2006.

[63] S. Yanagisawa, K. Lee, and Y. Morikawa. First-principles theoretical study of Alq_3/Al interfaces: Origin of the interfacial dipole. *J. Chem. Phys.*, 128(24):244704, 2008.

[64] Y. Nakano, S. Yanagisawa, I. Hamada, and Y. Morikawa. Theoretical study of vacuum level shift at the C_6H_6/Al(111) interface. *Surf. Interface Anal.*, 40(6-7):1059–1062, 2008.

[65] J. P. Perdew, K. Burke, and M. Ernzerhof. Generalized gradient approximation made simple. *Phys. Rev. Lett.*, 77(18):3865, 1996.

[66] N. Troullier and J. L. Martins. Efficient pseudopotentials for place-wave calculations. *Phys. Rev. B*, 43(3):1993, 1991.

[67] David Vanderbilt. Soft self-consistent pseudopotentials in a generalized eigenvalue formalism. *Phys. Rev. B*, 41(11):7892–7895, 1990.

[68] J. Neugebauer and M. Scheffler. Adsorbate-substrate and adsorbate-adsorbate interactions of Na and K adlayers on Al(111). *Phys. Rev. B*, 46(24):16067–16080, 1992.

[69] M. Douglas and N. M. Kroll. Quantum electrodynamical corrections to the fine structure of helium. *Ann. Phy.*, 82(1):89–155, 1974.

[70] B. A. Hess. Relativistic electronic-structure calculations employing a two-component no-pair formalism with external-field projection operators. *Phys. Rev. A*, 33(6):3742–3748, 1986.

[71] G. Jansen and B. A. Hess. Revision of the Douglas-Kroll transformation. *Phys. Rev. A*, 39(11):6016–6017, 1989.

[72] T. Tsuchiya, M. Abe, T. Nakajima, and K. Hirao. Accurate relativistic gaussian basis sets for H through Lr determined by atomic self-consistent field calculations with the third-order Douglas-Kroll approximation. *J. Chem. Phys.*, 115(10):4463–4472, 2001.

[73] M. J. Frisch, G. W. Trucks, H. B. Schlegel, G. E. Scuseria, M. A. Robb, J. R. Cheeseman, J. A. Montgomery, Jr., T. Vreven, K. N. Kudin, J. C. Burant, J. M. Millam, S. S. Iyengar, J. Tomasi, V. Barone, B. Mennucci, M. Cossi, G. Scalmani, N. Rega, G. A. Petersson, H. Nakatsuji, M. Hada, M. Ehara, K. Toyota, R. Fukuda, J. Hasegawa, M. Ishida, T. Nakajima, Y. Honda, O. Kitao,

H. Nakai, M. Klene, X. Li, J. E. Knox, H. P. Hratchian, J. B. Cross, V. Bakken, C. Adamo, J. Jaramillo, R. Gomperts, R. E. Stratmann, O. Yazyev, A. J. Austin, R. Cammi, C. Pomelli, J. W. Ochterski, P. Y. Ayala, K. Morokuma, G. A. Voth, P. Salvador, J. J. Dannenberg, V. G. Zakrzewski, S. Dapprich, A. D. Daniels, M. C. Strain, O. Farkas, D. K. Malick, A. D. Rabuck, K. Raghavachari, J. B. Foresman, J. V. Ortiz, Q. Cui, A. G. Baboul, S. Clifford, J. Cioslowski, B. B. Stefanov, G. Liu, A. Liashenko, P. Piskorz, I. Komaromi, R. L. Martin, D. J. Fox, T. Keith, M. A. Al-Laham, C. Y. Peng, A. Nanayakkara, M. Challacombe, P. M. W. Gill, B. Johnson, W. Chen, M. W. Wong, C. Gonzalez, and J. A. Pople. Gaussian 03, Revision D.02. Gaussian, Inc., Wallingford, CT, 2004.

[74] B. Hammer, L. B. Hansen, and J. K. Nørskov. Improved adsorption energetics within density-functional theory using revised perdew-burke-ernzerhof functionals. *Phys. Rev. B*, 59(11):7413–7421, 1999.

[75] P. Sony, P. Puschnig, D. Nabok, and C. Ambrosch-Draxl. Importance of van der waals interaction for organic molecule-metal junctions: Adsorption of thiophene on Cu(110) as a prototype. *Phys. Rev. Lett.*, 99(17):176401, 2007.

[76] Gabor A. Somorjai. *Introduction to Surface Chemistry and Catalysis*, chapter 7, page 442. John Wiley and Sons, Inc., New York, 1994.

[77] R. Caputo, B. P. Prascher, V. Staemmler, P. S. Bagus, and C. Wöll. Adsorption of benzene on coinage metals: A theoretical analysis using wavefunction-based methods. *J. Phys. Chem. A*, 111(49):12778–12784, 2007.

[78] P. S. Bagus, K. Hermann, and C. Wöll. The interaction of C_6H_6 and C_6H_{12} with noble metal surfaces: Electronic level alignment and the origin of the interface dipole. *J. Chem. Phys.*, 123(18):184109, 2005.

[79] G. Witte, S. Lukas, P. S. Bagus, and C. Wöll. Vacuum level alignment at organic/metal junctions:'cushion' effect and the interface dipole. *Appl. Phys. Lett.*, 87(26):263502, 2005.

[80] H. Koschel, G. Held, and H. P. Steinruck. The orientation of benzene on bimetallic surfaces. *Surf. Rev. Lett.*, 6(5):893–901, 1999.

[81] X. L. Zhou, M. E. Castroa, and J. M. Whitea. Interactions of UV photons and low energy electrons with chemisorbed benzene on Ag(111). *Surf. Sci.*, 238(1-3):215–225, 1990.

[82] S. Lukas. Ph.D. dissertation, Faculty for Chemistry, Rhur-University, Bochum, 2006.

[83] R. Dudde, K. H. Frank, and E. E. Koch. The electronic structure of benzene adsorbed on Ag(111) studied by angle resolved photoemission. *Surf. Sci.*, 225(3):267–272, 1990.

[84] T. J. Rockey, M. Yang, and H.-L. Dai. Adsorption energies, inter-adsorbate interactions, and the two binding sites within monolayer benzene on Ag(111). *J. Phys. Chem. B*, 110(40):19973–19978, 2006.

[85] L. Triguero, L. G. M. Pettersson, B. Minaev, and H. Ågren. Spin uncoupling in surface chemisorption of unsaturated hydrocarbons. *J. Chem. Phys.*, 108(3):1193–1205, 1998.

[86] A. Bilić, J. R. Reimers, N. S. Hush, R. C. Hoft, and M. J. Ford. Adsorption of benzene on copper, silver, and gold surfaces. *J. Chem. Theory Comput.*, 2(4):1093–1105, 2006.

[87] T. Munakata, T. Sakashita, M. Tsukakoshi, and J. Nakamura. Fine structure of the two-photon photoemission from benzene adsorbed on Cu(111). *Chem. Phys. Lett.*, 271(4-6):377–380, 1997.

[88] T. Munakata. Dispersion of an adsorption-induced electronic state of benzene/Cu(111). *J. Chem. Phys.*, 110(5):2736–2737, 1999.

[89] T. Munakata. Bonding state formed between adsorbed benzene and Cu(111). *Surf. Sci.*, 454-456(20):118–121, 2000.

[90] Y. Sonoda and T. Munakata. Occupied and unoccupied electronic states of benzene adsorbed Cu(110) surface. *Chem. Phys. Lett.*, 445(4-6):198–202, 2007.

[91] N. Lorente, M. F. G. Hedouin, R. E. Palmer, and M. Persson. Chemisorption of benzene and stm dehydrogenation products on Cu(100). *Phys. Rev. B*, 68(15):155401, 2007.

[92] P. Han, B. A. Mantooth, E. C. H. Sykes, Z. J. Donhauser, and P. S. Weiss. Benzene on Au{111} at 4 K: Monolayer growth and tip-induced molecular cascades. *J. Am. Chem. Soc.*, 126(34):10787–10793, 2004.

[93] S. Tsuzuki, K. Honda, T. Uchimaru, M. Mikami, and K. Tanabe. Origin of attraction and directionality of the π/π interaction: Model chemistry calculations of benzene dimer interaction. *J. Am. Chem. Soc.*, 124(1):104–112, 2002.

[94] S. Tsuzuki, K. Honda, T. Uchimaru, and M. Mikami. High-level *ab initio* computations of structures and interaction energies of naphthalene dimers: Origin of attraction and its directionality. *J. Chem. Phys.*, 120(2):647–659, 2004.

[95] P. S. Bagus, V. Staemmler, and C. Wöll. Exchangelike effects for closed-shell adsorbates: Interface dipole and work function. *Phys. Rev. Lett.*, 89(9):096104, 2002.

[96] M. Rohlfing and T. Bredow. Binding energy of adsorbates on a noble-metal surface: Exchange and correlation effects. *Phys. Rev. Lett.*, 101(26):266106, 2008.

[97] K. Toyoda, Y. Nakano, I. Hamada, K. Lee, S. Yanagisawa, and Y. Morikawa. First-principles study of the pentacene/Cu(111) interface: Adsorption states and vacuum level shifts. *J. Electron Spectrosc. Relat. Phenom.*, 174(1-3):78–84, 2009.

[98] A. Ferretti, C. Baldacchini, A. Calzolari, R. D. Felice, A. Ruini, E. Molinari, and M. G. Betti. Mixing of electronic states in pentacene adsorption on copper. *Phys. Rev. Lett.*, 99(4):046802, 2007.

[99] H. Yamane, D. Yoshimura, E. Kawabe, R. Sumii, K. Kanai, Y. Ouchi, N. Ueno, and K. Seki. Electronic structure at highly ordered organic/metal interfaces: Pentacene on Cu(110). *Phys. Rev. B*, 76(16):165436, 2007.

[100] H. Yamane, E. Kawabe, D. Yoshimura, R. Sumii, K. Kanai, Y. Ouchi, N. Ueno, and K. Seki. Intermolecular band dispersion in highly ordered monolayer and multilayer films of pentacene on Cu(110). *phy. stat. sol (b)*, 245(5):793–798, 2008.

[101] J. Lagoute, K. Kanisawa, and S. Fölsch. Manipulation and adsorption-site mapping of single pentacene molecules on Cu(111). *Phys. Rev. B*, 70(24):245415, 2004.

[102] S. Lukas, G. Witte, and Ch. Wöll. Novel mechanism for molecular self-assembly on metal substrates: Unidirectional rows of pentacene on Cu(110) produced by a substrate-mediated repulsion. *Phys. Rev. Lett.*, 88(2):028301, 2002.

[103] N. Koch, I. Salzmann, R. L. Johnson, J. Pflaum, R. Friedlein, and J.P. Rabe. Molecular orientation dependent energy levels at interfaces with pentacene and pentacenequinone. *Org. Electron.*, 7(6):537–545, 2006.

[104] D. Käfer and G. Witte. Evolution of pentacene films on Ag(111): Growth beyond the first monolayer. *Chem. Phys. Lett.*, 442(4-6):376–383, 2007.

[105] D. B. Dougherty, W. Jin, W. G. Cullen, J. E. Reutt-Robey, and S. W. Robey. Variable temperature scanning tunneling microscopy of pentacene monolayer and bilayer phases on Ag(111). *J. Phys. Chem. C*, 112(51):20334–20339, 2008.

[106] N. Koch, A. Vollmer, S. Duhm, Y. Sakamoto, and T. Suzuki. The effect of fluorination on pentacene/gold interface energetics and charge reorganization energy. *Adv. Mater.*, 19(1):112–116, 2007.

[107] P. G. Schroeder, C. B. France, J. B. Park, and B. A. Parkinson. Energy level alignment and two-dimensional structure of pentacene on Au(111) surfaces. *Appl. Phys. Lett.*, 91(5):3010–3014, 2002.

[108] C. B. France, P. G. Schroeder, J. C. Forsythe, and B. A. Parkinson. Scanning tunneling microscopy study of the coverage-dependent structures of pentacene on Au(111). *Langmuir*, 19(4):1274–1281, 2003.

[109] C. B. France, P. G. Schroeder, and B. A. Parkinson. Direct observation of a widely spaced periodic row structure at the pentacene/Au(111) interface using scanning tunneling microscopy. *Nano. Lett.*, 2(7):693–696, 2002.

[110] C. Baldacchini, C. Mariani, and M. G. Betti. dsorption of pentacene on filled *d*-band metal surfaces: Long-range ordering and adsorption energy. *J. Chem. Phys.*, 124(15):154702, 2006.

[111] N. J. Watkins, L. Yan, and Y. Gao. Electronic structure symmetry of interfaces between pentacene and metals. *Appl. Phys. Lett.*, 80(23):4384–4386, 2002.

[112] N. Koch. Energy levels at interfaces between metals and conjugated organic molecules. *J. Phys.: Condens. Matter*, 20(18):184008, 2008.

[113] M. Simeoni, S. Picozzi, and B. Delley. An ab-initio study of pentacene on aluminum (100) surface. *Surf. Sci.*, 562(1-3):43, 2004.

[114] K. Lee and J. Yu. Ab initio study of pentacene on Au(001) surface. *Surf. Sci.*, 589(1-3):8–18, 2005.

[115] G. Witte and Ch. Wöll. Molecular beam deposition and characterization of thin organic films on metals for applications in organic electronics. *phy. stat. sol. (a)*, 205(3):497–510, 2008.

[116] S. Söhnchen, S. Lukas, and G. Witte. Epitaxial growth of pentacene films on cu(110). *J. Chem. Phys.*, 121(1):525–534, 2004.

[117] E. Kawabe, H. Yamane, R. Sumii, K. Koizumi, Y. Ouchi, K. Seki, and K. Kanai. A role of metal d-band in the interfacial electronic structure at organic/metal interface: PTCDA on Au, Ag and Cu. *Org. Electron.*, 9(5):783–789, 2008.

[118] E. Annese, J. Fujii, C. Baldacchini, B. Zhou, C. E. Viol, I. Vobornik, M. G. Betti, and G. Rossi. Molecular charge distribution and dispersion of electronic states in the contact layer between pentacene and Cu(119) and beyond. *Phys. Rev. B*, 77(20):205417, 2008.

[119] Roald Hoffmann. A chemical and theoretical way to look at bonding on surfaces. *Rev. Mod. Phys.*, 60(3):601–628, 1988.

[120] H. Aizawa and S. Tsuneyuki. First-principles study of CO bonding to Pt(111): validity of the blyholder model. *Surf. Sci.*, 399(2-3):L364–L370, 1998.

[121] L. Romaner, G. Heimel, J. L. Brédas, A. Gerlach, F. Schreiber, R. L. Johnson, J. Zegenhagen, S. Duhm, N. Koch, and E. Zojer. Impact of bidirectional charge transfer and molecular distortions on the electronic structure of a metal-organic interface. *Phys. Rev. Lett.*, 99(25):256801, 2007.

[122] P. Hohenberg and W. Kohn. Inhomogeneous electron gas. *Phys. Rev.*, 136(3B):B864–B871, 1964.

[123] W. Kohn and L. J. Sham. Self-consistent equations including exchange and correlation effects. *Phys. Rev.*, 140(4A):A1133–A1138, 1965.

[124] L. Hedin and B. I. Lundqvist. Explicit local exchange-correlation potentials. *J. Phys. C*, 4:2064–2083, 1971.

[125] U. von Barth and L. Hedin. Local exchange-correlation potential for spin polarized case 1. *J. Phys. C*, 5:1629–1642, 1972.

[126] O. Gunnarsson and B. I. Lundqvist. Exchange and correlation in atoms, molecules, and solids by the spin-density-functional formalism. *Phys. Rev. B*, 13:4274–4298, 1976.

[127] W. E. Pickett. Pseudopotential methods in condensed matter applications. *Computer Physics Reports*, 9(3):115–197, 1989.

[128] D. R. Hamann, M. Schlüter, and C. Chiang. Norm-conserving pseudopotentials. *Phys. Rev. Lett.*, 43(20):1494–1497, 1979.

[129] G. P. Kerker. Non-singular atomic pseudopotentials for solid-state applications. *J. Phys. C*, 13:L189–L194, 1980.

[130] Alex Zunger and Marvin L. Cohen. First-principles nonlocal-pseudopotential approach in the density-functional formalism: Development and application to atoms. *Phys. Rev. B*, 18(10):5449–5472, 1978.

[131] Alex Zunger and Marvin L. Cohen. First-principles nonlocal-pseudopotential approach in the density-functional formalism. ii. application to electronic and structural properties of solids. *Phys. Rev. B*, 20(10):4082–4108, 1979.

[132] Leonard Kleinman and D. M. Bylander. Efficacious form for model pseudopotentials. *Phys. Rev. Lett.*, 48(20):1425–1428, 1982.

[133] Y. Zhang and W. Yang. Comment on "generalized gradient approximation made simple". *Phys. Rev. Lett.*, 80(4):890–890, 1998.

[134] D. C. Langreth and J. P. Perdew. The exchange-correlation energy of a metallic surface. *Solid State Commun.*, 17(11):1425–1429, 1975.

[135] D. C. Langreth and J. P. Perdew. Exchange-correlation energy of a metallic surface: Wave-vector analysis. *Phys. Rev. B*, 15(6):2884–2901, 1977.

[136] H. Rydberg, M. Dion, N. Jacobson, E. Schröder, P. Hyldgaard S. I. Simak, D. C. Langreth, and B. I. Lundqvist. Van der waals density functional for layered structures. *Phys. Rev. Lett.*, 91:126402, 2003.

List of publications

1. K. Toyoda, Y. Nakano, I. Hamada, K. Lee, S. Yanagisawa, and Y. Morikawa: "First-principles study of benzene on noble metal surfaces: Adsorption states and vacuum level shifts" *Surf. Sci.*, 603(18):2912-2922, 2009.

2. K. Toyoda, Y. Nakano, I. Hamada, K. Lee, S. Yanagisawa, and Y. Morikawa: "First-principles study of the pentacene/Cu(111) interface: Adsorption states and vacuum level shifts" *J. Electron. Spectrosc. Relat. Phenom.*, 174(1-3):78-84, 2009.

3. K. Toyoda: "First-principles study of π conjugate molecules adsorbed on noble metal interfaces." *Panasonic Technical Journal*, 55(4):27-32, 2010.

4. K. Toyoda, I. Hamada, S. Yanagisawa, and Y. Morikawa: "Origin of surface-band dispersion at the pentacene/Cu interface" *APEX*, 3:025701, 2010.

5. K. Toyoda, I. Hamada, K. Lee, S. Yanagisawa, and Y. Morikawa: "First-principles study of pentacene/noble metal interfaces: Vacuum level shifts and electronic structures" *J. Chem. Phys.*, submitted.

6. K. Toyoda, I. Hamada, K. Lee, S. Yanagisawa, and Y. Morikawa: "First-principles study of perfluoropentacene/noble metal interfaces: Vacuum level shifts and electronic structures" *Phys. Rev. B*, submitted.

7. K. Toyoda, I. Hamada, S. Yanagisawa, and Y. Morikawa: "First-principles Study of Interface Dipole of Conjugate Molecules Adsorbed on Noble Metal Surfaces": *5th Handai Nanoscience and Nanotechnology International Symposium Nano-Advanced Materials Design*, P1-31, 2009.